

**METAL ASSISTED CHEMICALLY ETCHED SILICON
NANOWIRES FOR APPLICATION IN A HYBRID
SOLAR CELL**

BY

SIPHESIHLÉ SIPHAMANDLA MAGUBANE



**A thesis submitted in fulfilment of the requirement for the degree of
Magister Scientiae in the Department of Physics and Astronomy,
University of the Western Cape (UWC).**

Supervisor: Dr T.F.G. Muller (UWC)

Co-supervisor: Prof C.J. Arendse (UWC)

Co-supervisor: Prof C.J. Oliphant (NMISA)

November 2018



DEDICATION

This thesis is dedicated to my mother, Tryphina Zibuyile Magubane.



KEYWORDS

Metal assisted chemically etched silicon nanowires for application in a hybrid solar cell

Photovoltaics

Bulk-heterojunction

Inorganic-organic hybrid layers

Optimisation

Metal assisted chemical etching

Silicon nanowire

Spin coating

Poly (3-hexylthiophene-2, 5-diyl)

Charge carrier donor-acceptor interface

Optical properties

Electric properties

Current density-Voltage measurements

Power conversion efficiency



ABSTRACT

Metal assisted chemically etched silicon nanowires for application in a hybrid solar cell

S.S. Magubane

MSc. Thesis, Department of Physics and Astronomy, University of the Western Cape

Photovoltaic (PV) devices based on inorganic-organic hybrid active layers have been extensively studied for over a decade now. However, photoactive hybrid layers of material combinations such as rr-P3HT and SiNWs still require further exploration as candidates for solar cell (SC) fabrication, due to favourable optical absorption and charge carrier mobility associated with them respectively. The ultimate goal of the study is to fabricate ITO/PEDOT:PSS/rr-P3HT:SiNWs/Al SCs with different SiNWs content and investigate the different parameters or factors influencing the performance of these cells. The vertically aligned SiNW arrays on a Si wafer were synthesised via metal assisted chemical etching (MACE) and a method of chemically detaching these wires was developed. The average length and the diameter of the SiNWs obtained were 4.5 μm and 0.2 μm , respectively. Different weight ratios of as-synthesised SiNWs were then incorporated within rr-P3HT to form different hybrid solutions, i.e. rr-P3HT: 0.3 wt% SiNWs, rr-P3HT: 0.7 wt% SiNWs and rr-P3HT: 1.3 wt% SiNWs. In addition, a pure rr-P3HT solution was made for reference purposes. SEM characterisation shows that the SiNWs are randomly distributed across the active area, and that the film becomes progressively inhomogeneous upon addition of SiNWs, whereas the TEM characterisation revealed that there is no chemical interaction between the rr-P3HT and SiNWs. The UV-Vis and PL spectra suggest that there are changes in absorption and emission characteristics upon SiNW incorporation into the rr-P3HT matrix, which may have impacted the charge transfer. The electrical properties of the different hybrid films were probed using Hall Effect measurements, which revealed that the conductivity increases with the increase in the concentration of nanowires (NWs). The increase in conductivity upon the addition of SiNWs in the rr-P3HT matrix was related to an increase of the mobility (μ) of charge carriers in the hybrid films. The maximum conductivity was obtained from the rr-P3HT: 1.3 wt% SiNWs thin film. Hybrid solar

cells were characterised by measuring the current density-voltage under illumination. The baseline power conversion efficiency (PCE) of 0.0007 % was calculated for the smallest concentration of SiNWs (i.e. rr-P3HT: 0.3 % SiNWs). By increasing the concentration of SiNWs into the rr-P3HT matrix an efficiency of up to 0.0011 % was realised for rr-P3HT: 1.3 wt% SiNWs. Since the PCE of rr-P3HT: SiNWs was very low, PCBM was added to the blend and the PCE improved to 0.68 % for the rr-P3HT: PCBM: 0.8 wt% SiNWs cell. The enhancement in the PCE was related to the fact that more electron accepting candidates were present in the active layer to extract electrons from rr-P3HT, which reduced charge carrier losses. Thus the effect of the SiNWs could be better understood.

November 2018



DECLARATION

I declare that, “*Metal assisted chemically etched silicon nanowires for application in a hybrid solar cell*” is my own work, that it has not been submitted for any degree or examination in any other university, and that all the sources I have used or quoted have been indicated and acknowledged by complete references.

Full name: Siphehile Siphamandla Magubane

Date: November 2018

Signed: _____



ACKNOWLEDGEMENTS

I would like to express my deepest and heartfelt gratitude's to the following people and organisations without whose assistance and support, the completion of this study would not have been possible.

- First and foremost I would like to thank God, the pillar and the source of everything for opportunities He has granted me.
- My supervisor Dr T.F.G. Muller for his excellent supervision, guidance and support. Working with him has been a great experience of my life and I thank him for that.
- My co-supervisors, Prof C.J. Arendse and Prof. C. J. Oliphant, for their enlightening advice and expertise in photovoltaics.
- National Research Foundation, iThemba Labs and University of the Western Cape for financial support.
- Electron Microscope Unit (UWC), Dr F.R. Cummings, Miss N. Peterson, Mr E. McDonald and Miss N. Kensley for always opening their arms for me whenever I needed to do SEM and/or TEM characterisations.
- Management staff of the Department of Physics and Astronomy, UWC.
- My seniors, Sifiso Khanyile and Sphelo Ngqoloda for their inspiration, motivation and encouragements throughout the study.
- My colleagues Anele Tshaka, Jene Slinger, Sinovulo Tanci, Jean Mbokam and Norman Bowers for the worthwhile conversation we used to have from time to time.
- My grandmother Thokozile Magubane and my two aunties Nobuhle and Bonisile Magubane whose sacrifices, patience and consistent love and support will forever be appreciated. Their little knowledge about research and employment opportunities it comes with, did not stop them from believing in me.
- My siblings Minenhle, Lindokuhle, Lihlithemba, Tsepang, Snethemba, Sbahle and Mnqobi, their belief in me has always been an inspiration and motivation that kept me striving.

- Last but not least, I would like to thank all my close friends for their support and comfort. They have always been there for me, providing joy even in times of difficulty.

“No dream is too big and no challenge is too great. Nothing we want for our future is beyond our reach. Never settle for anything less than the best”, Donald Trump



CONTENT

1 LITERATURE REVIEW	1
1.1 INTRODUCTION.....	1
1.2 SOLAR CELLS.....	4
1.2.1 <i>First generation solar cells</i>	6
1.2.2 <i>Second generation solar cells</i>	6
1.2.3 <i>Third generation solar cells</i>	7
1.3 CONJUGATED POLYMERS	9
1.3.1 <i>Electronic structure of carbon</i>	9
1.3.2 <i>Type of bonds formed by carbon</i>	10
1.3.3 <i>Formation of molecular orbitals</i>	11
1.3.4 <i>Polymer names, structures and average molecular weights</i>	14
1.4 CONJUGATED POLYMERS FOR PV DEVICES.....	16
1.4.1 <i>Types of polymers used in solar cells</i>	16
1.4.2 <i>Preparation methods of polymers</i>	18
1.4.3 <i>Electronic and optical properties</i>	19
1.5 SILICON NANOWIRES (SiNWs)	20
1.5.1 <i>SiNWs synthesis methods</i>	21
1.5.2 <i>Properties of SiNWs</i>	24
1.6 DEVICE ARCHITECTURE	26
1.7 CHARGE GENERATION AND TRANSPORT PROCESSES WITHIN BHJ PVs	27
1.8 DEVICE EFFICIENCY	28
1.9 THESIS STRUCTURE	30
1.9.1 <i>Aim of the study</i>	30
1.9.2 <i>Outline of the thesis</i>	30
REFERENCES	32
2 ANALYTICAL TECHNIQUES	37
2.1 INTRODUCTION.....	37
2.2 SCANNING ELECTRON MICROSCOPY	38
2.2.1 <i>Introduction</i>	38
2.2.2 <i>Resolution</i>	39
2.2.3 <i>Depth of focus, aperture size and working distance</i>	40
2.2.4 <i>Electron beam and specimen interaction</i>	41

2.2.5 <i>Detection of secondary and backscattered electrons</i>	43
2.2.6 <i>Energy dispersive X-ray spectroscopy (EDS)</i>	44
2.2.7 <i>Sample preparation for SEM</i>	46
2.3 TRANSMISSION ELECTRON MICROSCOPY	46
2.3.1 <i>Introduction</i>	46
2.3.2 <i>Basic operation</i>	46
2.3.3 <i>Electron diffraction</i>	48
2.3.4 <i>The formation of a diffraction pattern.</i>	50
2.3.5 <i>Sample preparation for TEM</i>	52
2.4 STYLUS PROFILOMETRY	53
2.4.1 <i>Introduction</i>	53
2.4.2 <i>Working principle</i>	53
2.4.3 <i>Horizontal scan resolution</i>	54
2.5 HALL EFFECT	54
2.5.1 <i>Introduction</i>	54
2.5.2 <i>Theory</i>	55
2.6 ULTRAVIOLET – VISIBLE SPECTROSCOPY.....	56
2.6.1 <i>Introduction</i>	56
2.6.2 <i>Theory</i>	57
2.6.3 <i>UV-Vis mechanism</i>	57
2.6.4 <i>Experimental set-up</i>	59
2.7 PHOTOLUMINESCENCE.....	60
2.7.1 <i>Introduction</i>	60
2.7.2 <i>Theory</i>	60
2.7.3 <i>Experimental set-up</i>	62
REFERENCES	64
3 METAL ASSISTED CHEMICAL ETCHING OF SILICON WAFER FOR THE FORMATION OF SILICON NANOWIRES.....	67
3.1 INTRODUCTION.....	67
3.2 MACE MECHANISM	68
3.2.1 <i>Formation of silver nanoparticles</i>	68
3.2.2 <i>Formation of SiNWs</i>	71
3.3 EXPERIMENTAL	73

3.3.1 <i>Solution preparation</i>	73
3.3.2 <i>Synthesis process</i>	74
3.3.3 <i>Detachment of SiNWs</i>	74
3.4 RESULTS AND DISCUSSION.....	75
3.4.1 <i>Silver nanoparticle deposition</i>	75
3.4.2 <i>Silicon nanowires formation</i>	76
3.4.3 <i>Horizontal etching</i>	79
3.4.4 <i>Transfer of SiNWs onto another substrate</i>	82
3.4.5 <i>TEM characterisation of SiNWs</i>	83
3.4.6 <i>Optical properties of SiNWs</i>	84
3.5 CONCLUSION	86
REFERENCES	87
4 INCORPORATION OF SINWS INTO RR-P3HT MATRIX FOR SOLAR CELL APPLICATION.....	89
4.1 INTRODUCTION	89
4.2 SPIN COATING TECHNIQUE.....	90
4.2.1 <i>Introduction</i>	90
4.2.2 <i>Spin coating mechanism</i>	91
4.2.3 <i>Spin coating experimental setup</i>	93
4.2.4 <i>Samples preparation and device fabrication</i>	94
4.3 RESULTS AND DISCUSSION.....	95
4.3.1 <i>Morphology</i>	95
4.3.2 <i>Thicknesses of the hybrid films</i>	96
4.3.3 <i>Absorption properties</i>	98
4.3.4 <i>Emission properties</i>	99
4.3.5 <i>High Resolution TEM analysis</i>	101
4.3.6 <i>Electric properties and current density-voltage characteristics (J-V curves)</i>	105
4.4 CONCLUSION	110
REFERENCE	111
5 SUMMARY AND RECOMMENDATIONS.....	114

LIST OF TABLES

Table 2. 1: Analytical technique used in this study	37
Table 2. 2: Typical chromophores	59
Table 3. 1: Summary of the solution preparation	74
Table 4. 1: Thickness and conductivity of spin coated films.....	106
Table 4.2: Photovoltaic parameters of ITO/PEDOT:PSS/rr-P3HT:SiNWs/Al devices with different weight ratios of SiNWs.....	108
Table 4.3: Photovoltaic parameters of ITO/PEDOT:PSS/rr-P3HT:PCBM:SiNWs/Al devices with different weight ratios of SiNWs.....	110



LIST OF FIGURES

Figure 1. 1: (a) shows the world energy consumption 2014, (b) illustrate the intensity of carbon emission in some common energy generation techniques [1.6].	2
Figure 1. 2: Global total photon flux from the sun and maximum achievable integrated short circuit current density (J_{sc}) [1.8].	4
Figure 1. 3: The comparison of photoelectric effect on the left and photovoltaic effect on the right. The blue or ultraviolet light provides enough energy for an electron to escape completely from the surface of the metal.	5
Figure 1. 4: Various type of materials and SC technologies that have been explored over the past decades [1.11]......	5
Figure 1. 5: The representation of the atomic s orbital (a), p orbitals (b-d) and hybrid orbitals (e-f) [1.40]......	10
Figure 1. 6: Types of carbon bonds depicted by the illustration of molecular structures of, (a) methane (CH_4), (b) ethylene (C_2H_4) and (c) acetylene (C_2H_2) [1.41].....	11
Figure 1. 7: Schematic representation of the formation of the sigma (σ) bonding and anti-bonding (σ^*) orbitals in the combination of two hydrogen atoms [1.42].	12
Figure 1. 8: Energy levels of molecular orbitals of H_2 [1.42].....	13
Figure 1. 9: Band scheme for semiconductors [1.44].	14
Figure 1. 10: Representation of phenyl and thiophene rings and their connections, (a), (b) and (c) shows, o-xylene, m-xylene and p-xylene respectively while (d), (e) and (f) shows head-to-tail, tail-to-tail and head-to-head thiophene rings connections respectively [1.46].....	15
Figure 1. 11: Representation of the polymer structures, (a) regioregular and (b) regiorandom structure [1.46].....	16
Figure 1. 12: Structural representation of selected D polymers and the most popular used fullerene (PCBM). The red and blue units are D and A units, respectively [1.1]......	17
Figure 1. 13: HOMO and LUMO energy levels of selected polymers commonly used for SCs applications [1.1].....	19
Figure 1. 14: Absorption co-efficients of films of selected materials compared to standard AM 1.5 terrestrial solar spectrum [1.49].	20

Figure 1. 15: Schematics of experimental setups for SiNW growth, (a) VLS mechanism, (b) CVD, (c) Electroless metal deposition and dissolution (d) Evaporation of SiO, (e) MBE and (f) Laser Ablation [1.52, 1.55].	22
Figure 1. 16: Device architecture of BHJ photovoltaic [1.82].....	27
Figure 1. 17: Schematic representation of working mechanism of BHJ PV [1.1].....	28
Figure 1. 18: J-V characteristic of a PV in dark condition and under light illumination which is obtained by applying variable voltage and measuring the current density obtain [1.86].....	29
Figure 2. 1: Schematic diagram of scanning electron microscope (JSM-5410, courtesy of JEOL, USA).....	39
Figure 2. 2: Schematic depicting the relationship between the aperture size and the depth of focus (Fig 2.2 (a) and (b)), and the relationship between the working distance and the depth of focus (fig 2.2 (b) and (c)) [2.6].	40
Figure 2. 3: Schematic representation of signals that may be used in SEM [2.7].	41
Figure 2. 4: The interaction volume between electron the beam and the specimen [2.8]	42
Figure 2. 5: Schematic representation of the secondary electrons detection [2.1].....	43
Figure 2. 6: Schematic representation of the generation of characteristic X-rays within an atom [2.10].	44
Figure 2. 7: Simulated EDS spectrum [2.11].	45
Figure 2. 8: Schematic representation of a TEM and its important components (JEM- 1010, courtesy of JEOL Ltd.).....	47
Figure 2. 9: The schematic representation of a cross section of a crystalline specimen bombarded by a beam of electrons (I). Electrons may emerge on the other side of the specimen having scattered (D and N) or unscattered (T) [2.16].	49
Figure 2. 10: Schematic diagram showing the geometry of diffraction pattern information [2.16].	50
Figure 2. 11: The ray diagram of a projection microscope showing position of diffraction pattern and an image [2.6].....	51
Figure 2. 12: Shows various types of diffraction patterns produced by specimens of different microstructure; (a) is a single perfect crystal, (b) consist small number of grain and (c) consist a large number of randomly oriented grains [2.16].	52

Figure 2. 13: Schematic representation of Dektak 6M architecture [2.17]	54
Figure 2. 14: The schematic representation of Hall Effect theoretical model [2.21].....	56
Figure 2. 15: Various possible transitions between the bonding and anti-bonding electronic states of a molecule [2.24].....	58
Figure 2. 16: Simplified Schematic of a double beam UV-Vis spectrophotometer [2.25].	60
Figure 2. 17: Energy diagram showing absorption of light and the processes involved in the emission of light as fluorescence and phosphorescence [2.29].....	62
Figure 2. 18: Schematic diagram of the NanoLog spectrofluorometer showing the main features of the system [2.30].	63
Figure 3. 1: Schematic illustration of MACE of Si for the realisation of SiNWs [3.6]..	68
Figure 3. 2: Mechanism diagram of electroless Ag deposition on the Si substrate in HF/AgNO ₃ solution, (a) Formation of Ag nucleation, (b) Ag particles growth and Si oxidation and (c) Ag particle trapped in the pit created by the dissolution of SiO ₂ [3.7].....	69
Figure 3. 3: This diagram represent the dynamic electrochemical redistribution of Ag between nanoparticles [3.9].	70
Figure 3. 4: The dependence of deposited AgNPs distribution and shapes with time on a p (100) Si substrate, as shown by Zachary et.al [3.9].	71
Figure 3. 5: Mechanism of Ag nanoparticle- assisted chemical etching of silicon which lead to the formation of SiNWs [3.8].....	72
Figure 3. 6: Schematic representation of base etched SiNWs [3.15].....	73
Figure 3. 7: Synthesising solutions and steps followed during SiNWs formations.....	73
Figure 3. 8: (a) SEM image of AgNPs deposited on an n-type Si (100) wafer by immersion in an aqueous solution of AgNO ₃ and HF at room temperature for 60 seconds and (b) size distribution histogram of AgNPs.	75
Figure 3. 9: EDS spectrum of AgNPs on the n-type Si (100) wafer.....	76
Figure 3. 10: SEM micrographs of (a) and (b) cross sectional images of AgNPs/SiNWs etched for 10 and 20 minutes respectively, (c) and (d) the cross sectional and top view image of AgNP-free SiNWs etched for 20 minutes, respectively.....	78
Figure 3. 11: (a) Histogram distribution of SiNW diameters and (b) the EDS spectrum of as-synthesised n-type SiNWs.	79
Figure 3. 12: SEM cross-sectional micrographs of base etched SiNWs in the etching solution II for (a) 2 minutes, (b) 4 minutes, (c) 6 minutes and (d) 8 minutes.....	80

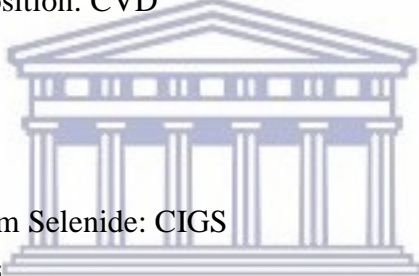
Figure 3. 13: SEM images of n-type Si wafers after SiNWs detachment through sonication. These samples, (a), (b), (c) and (d) were immersed in etching solution II for 2, 4, 6 and 8 minutes, respectively.....	81
Figure 3. 14: SiNWs deposited on a glass substrate. These correspond to the wafers depicted in figure 3.13 above.....	83
Figure 3. 15: TEM characterisation of an as-synthesised single SiNW, with (a) and (b) low and high magnification TEM micrographs, (c) is the HR-TEM micrograph and (d) is the SAED pattern of as-synthesised wire.	84
Figure 3. 16: Optical absorption spectrum of n-type SiNWs over a wavelength range of 300-1200 nm.	85
Figure 3. 17: Photoluminescence spectrum of n-type SiNWs.	86
Figure 4. 1: Different stages of spin coating deposition process [4.19].....	91
Figure 4. 2: Schematic representation of spin coating experimental setup [4.25].	94
Figure 4. 3: SEM micrographs of the photoactive hybrid layers; (a) rr-P3HT, (b) rr-P3HT: 0.3 wt % SiNWs, (c) rr-P3HT: 0.7 wt% SiNWs and (d) rr-P3HT: 1.3 wt% SiNWs.	96
Figure 4. 4: Dependence of thickness on the amount of SiNWs incorporated into the rr-P3HT matrix, (a) shows the thickness profiles whereas (b) shows the average thickness of the films.	97
Figure 4. 5: Gaussian deconvoluted UV-Vis absorption spectrum of rr-P3HT thin film.	98
Figure 4. 6: UV-vis absorption spectra of thin films of rr-P3HT and rr-P3HT: SiNWs with different SiNWs weight percent ratios.....	99
Figure 4. 7: Gaussian deconvoluted photoluminescence emission spectrum of rr-P3HT thin films.	100
Figure 4. 8: Photoluminescence emission spectra of thin films of rr-P3HT and rr-P3HT: SiNWs with different SiNWs weight percent ratios.	101
Figure 4. 9: HR-TEM micrograph of rr-P3HT thin film. The inset displays the SAED pattern of the rr-P3HT.....	102
Figure 4. 10: EDS spectrum of the rr-P3HT film.	103
Figure 4. 11: TEM images, (a) SiNWs covered by rr-P3HT and (b) crystallographic information on rr-P3HT: 1.3 wt% SiNWs.	104

Figure 4. 12: The SAED pattern for the combination of rr-P3HT: 1.3 wt % SiNWs, (a) is the unindexed pattern which serve as a reference and (b) is the indexed pattern.	105
Figure 4. 13: J-V characteristics of ITO/PEDOT:PSS/rr-P3HT:SiNWs/Al devices with different weight ratios of SiNWs measure in dark and under light illumination, the inset is the zoomed-up J-V curve close to the origin.	107
Figure 4. 14: J-V characteristics of ITO/PEDOT:PSS/rr-P3HT:PCBM:SiNWs/Al devices with different weight ratios of SiNWs measure in dark and under light illumination.	109



LIST OF ABBREVIATIONS, ACRONYMS AND SYMBOLS

Absorbance: A
Acetylene: C₂H₂
Amorphous silicon: aSi
Back-scattered electrons: BE
Bulk Heterojunction: BHJ
Cadmium telluride: CdTe
Carbon: C
Carbon dioxide: CO₂
Carrier concentration: n
Carrier mobility: μ
Charged coupled device: CCD
Chemical vapour deposition: CVD
Chloroform: CF
Conduction band: CB
Copper: Cu
Copper Indium Gallium Selenide: CIGS
Crystalline silicon: cSi
Current density-voltage: J-V
Deionised water: DI water
Depth of focus: D
Dichlorobenzene: DCB
Drift velocity: V_d
Dye-sensitised solar cell: DSSC
Electric charge: q
Electric force: **F**_e
Energy band gap: E_g
Energy dispersive x-ray spectroscopy: EDS
Ethylene: C₂H₄
External conversion: ec
Field effect transistor: FET
Fill factor: FF



Gallium: Ga

Gold: Au

Hall co-efficient: R_H

Hall electric field: \mathbf{E}_H

Hall voltage: V_H

High Resolution Transmission Electron Microscope: HR-TEM

Highest occupied molecular orbital: HOMO

Hydrofluoric acid: HF

Hydrogen: H

Hydrogen peroxide: H_2O_2

Indium: In

Indium Gallium Arsenide: InGaAs

Indium tin oxide: ITO

International Energy Agent: IEA

Inter-Governmental Panel on Climate Change: IPCC

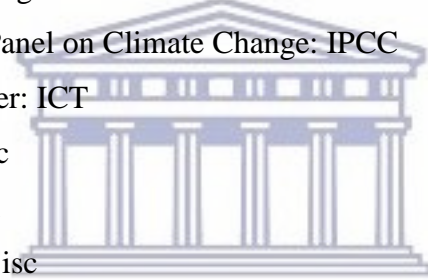
Internal charge transfer: ICT

Internal conversion: ic

Interplanar spacing: d

Intersystem crossing: isc

Iodine: I



Kinetic Energy: KE

Lattice constant: a

Light emitting diode: LED

Linear variable differential transformer: LVDT

Lowest unoccupied molecular orbital: LUMO

Magnetic field: \mathbf{B}

Magnetic force: \mathbf{F}_B

Metal assisted chemical etching: MACE

Methane: CH_4

Methyl: CH_3

Molar absorptivity: ϵ

Molecular beam epitaxy: MBE

Mono-crystalline silicon: mono-cSi

Multichannel analyser: MCA

Nanoparticle: NPs

Nanowires: NWs

Nitric acid: HNO₃

Nitrogen: N

Number of average molecular weight: M_N

Open source voltage: V_{oc}

Organic photovoltaics: OPVs

Organic solar cell: OSC

Oxygen: O

Phenyl-C₆₁-butyric acid methyl ester: PCBM

Photoluminescence: PL

Photomultiplier tube: PMT

Photovoltaic: PV

Pi: π

Poly (2, 6-bis (3-alkylthiophen-2-yl) dithieno-[3, 2-b; 2', 3'-d] thiophene): PDTPBT

Poly (3-hexylthiophene-2, 5-diyl): P3HT

Poly (ethylene-dioxythiophene): poly (styrene sulfonate): PEDOT: PSS

Poly[2,6-(4,4-bis-(2-ethylhexyl)-4H-cyclopenta [2,1-b;3,4-b']dithiophene)-alt-4,7(2,1,3-benzothiadiazole)]: PCPDTBT

Poly [2-methoxy-5-(2-ethylhexyloxy)-1, 4-phenylenevinylene]: MEH-PPV

Poly [2-methoxy-5-(3', 7'-dimethyloctyloxy)-1, 4-phenylenevinylene]: MDMO-PPV

Polyacetylene: PAc

Polyaniline: PANI

Poly-crystalline silicon: poly-cSi

Polyfluorenes: PFOs

Polyphenylene vinylene: PPV

Polypyrroles: PPy

Polythiophenes: PTs

Power Conversion Efficiency: PCE

Quantum Confinement Effect: QCE

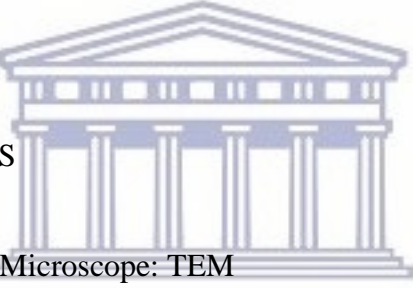
Reaction-ion etching: RIE

Residentiary Apparatus for Device Application Research: RADAR

Resistivity: ρ

Scanning Electron Microscopy: SEM

Secondary electrons: SE
Selected Area electron diffraction pattern: SAED
Selenide: Se^{2-}
Series resistance: R_s
Short circuit current density: J_{sc}
Shunt resistance: R_{sh}
Sigma: σ
Silane: SiH_4
Silicon dioxide: SiO_2
Silicon monoxide: SiO
Silicon: Si
Silicon-tetrachloride: SiCl_4
Silver: Ag
Silver Nitrate: AgNO_3
Soda lime silicate: SLS
Solar cell: SC
Solid-Liquid-Solid: SLS
Sulfur: S
Transmission Electron Microscope: TEM
Transmittance: T
Ultraviolet: UV
Ultraviolet-visible: UV-Vis
Valence band: VB
Vapor-Liquid-Solid: VLS
Water: H_2O
Wavelength: λ
Weight of average molecular weight: M_w
X-ray diffraction: XRD



1 LITERATURE REVIEW

1.1 Introduction

The world's energy production depends mostly on fossil fuels which consequently produce carbon dioxide (CO₂) and other greenhouse gases as by-products. Due to the rapid growth of the human population and a modernizing society, the world's energy demand is predicted to double and electricity demand to quadruple by 2050 [1.1]. This predicted increase in energy demand will result in an 80 % increase in CO₂ emission if environmental friendly energy generation alternatives are not implemented [1.1]. L. Alexander at el. (2013) in the Inter-governmental panel on climate change (IPCC)'s fifth assessment report reported that the atmospheric concentration of CO₂ has increased to an unprecedented level over the last 800 000 years and that human influence toward this negative impact is very significant [1.2]. The report elucidated that there is a direct relationship between the global temperature and atmospheric concentration of CO₂, and also outlined how the future global temperature can be stabilised by reducing CO₂ output.

The IPCC's impact, adoption and vulnerability report concluded that a number of negative impacts will arise due to climate change [1.3]. The major risks include; food insecurity, fresh water access, extreme weather and floods, and the loss of marine and coastal ecosystems. Even though it is very crucial to reduce the CO₂ output, unfortunately the progress has been slow thus far. The global temperature increase target that has been agreed on internationally is 2 °C, however the International Energy

Agency (IEA) estimates that the long term global temperature increase of 3.6 °C is on track but can increase even further if no proper mechanisms are put in place [1.4 -1.5]. Figure 1.1 (a) and (b) illustrate the world energy consumption figures from a study conducted in 2014 by fuel projection, which shows that oil is the dominant consumed energy, and the carbon (C) intensity emitted by some of the common electricity generation methods, respectively [1.6].

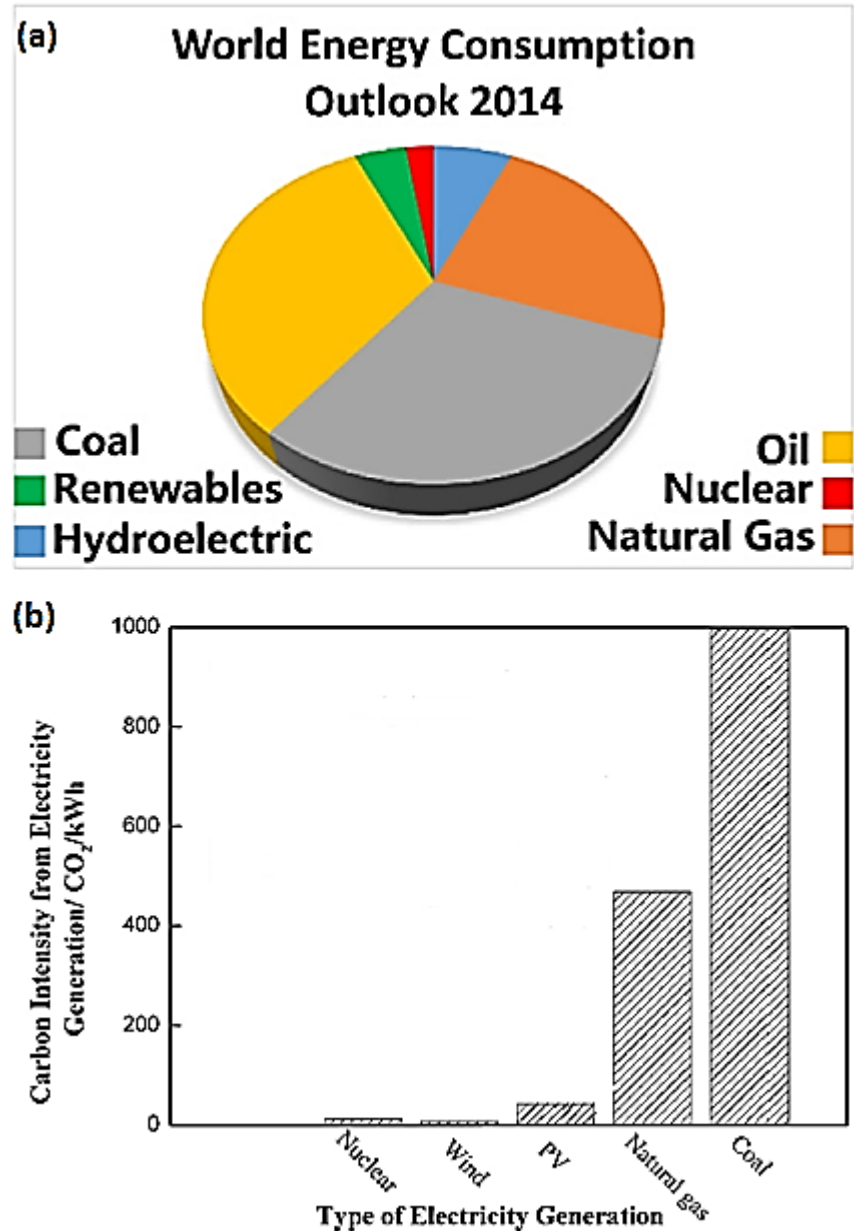


Figure 1. 1: (a) shows the world energy consumption 2014, (b) illustrate the intensity of carbon emission in some common energy generation techniques [1.6].

In order to reduce the emission of CO₂ and other toxic gases, renewable energy is one of the promising alternatives. Of these solar energy is at the forefront. Solar energy is an unlimited and free source of energy. According to the latest figures, the earth

surface receives about 3.85 yottajoules per year of solar power [1.7]. However, the maximum achievable photocurrent by photovoltaic (PV) devices making use of the power from the sun, is determined by the breadth of the absorption of the active layer and the degree of overlap with the photon flux from the sun, as depicted in figure 1.2 [1.8]. This is important when deciding upon the type of materials to be used for solar cells (SCs), as the suitable active layer materials should be targeting a maximum photocurrent.

Even though solar energy is abundant, sustainable and environmentally friendly as compared to commercial energy supply, which is based on fossil fuel, there is an initial expenditure on the equipment for harvesting this radiant energy by the development of SCs, panels and modules [1.9]. On that note, a lot of research work have been done and still in progress to reduce solar devices production cost, and to improve the power conversion efficiency (PCE) of SCs. Solar energy currently provides less than 3 % of the electricity demand with its wide application in countries like Europe, China and USA [1.10]. Global installation of PVs have been increasing rapidly since the year 2000, and the continual decrease in the price of solar modules provide strong reasons to believe in the potential for solar electricity generation to become a major source of low-carbon energy in the future. The IEA predicted that solar energy could generate 22 % of the world's electricity by 2050 [1.1]; however this percentage could be surpassed if low cost and large scale PVs devices could be implemented as a result of new technologies.

Even though solar energy is considered as the solution to the world's energy crisis, this type of electricity production has limitations too: (i) the solar radiant energy received on earth vary depending on the geographic location and time of the day i.e. a lot of radiant energy is received from the sun during the day than at night [1.11]. (ii) An enormous amount of sunlight is required for the generation of electricity from solar PV devices [1.12-1.13]. (iii) Seasons of the year and weather conditions dictate the amount of radiant energy reaching the surface of the earth, i.e. the amount of sunlight reaching the earth surface reduces during winter and the sun's radiation is less intense [1.13]. In order to minimise these disadvantages associated with this technology, solar energy must be stored elsewhere at night and effective SCs and modules need to be developed. The storage of solar power is still an unresolved problem up to date; however a lot of

research activities which aim at inventing solar power storage and effective batteries are underway.

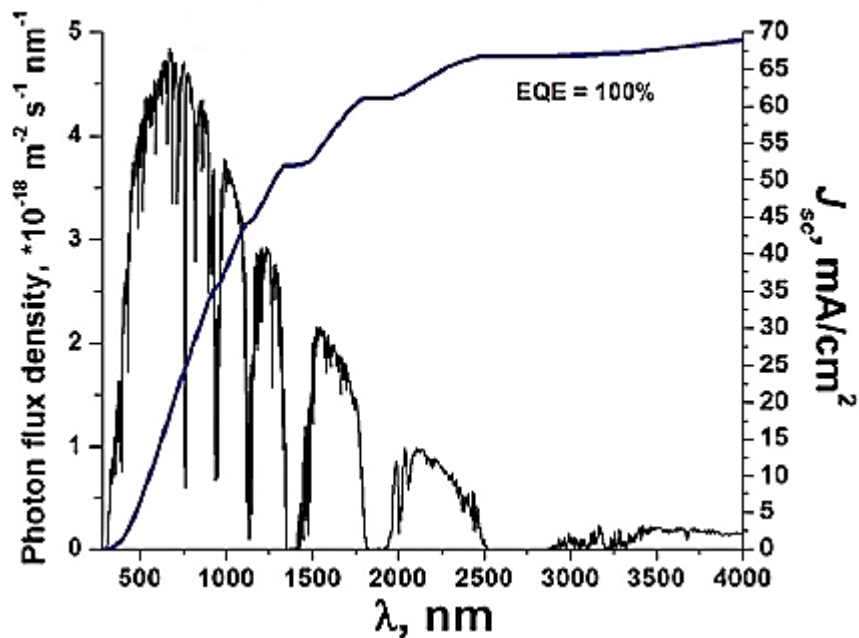


Figure 1.2: Global total photon flux from the sun and maximum achievable integrated short circuit current density (J_{sc}) [1.8].

1.2 Solar cells

A SC is an electric device that converts radiant energy from the sun directly into electricity by the means of a chemical and physical phenomenon known as the photovoltaic effect. It is a form of a photoelectric cell, defined as a device whose electrical characteristics vary with exposure to light. Solar panels are a collection of SCs arranged in a defined geometrical shape used to produce a given amount of power. PV technology obeys the principle that each SC consist of two different layers of semiconducting materials, which are n-type and p-type semiconductors. When a p-type semiconductor, which has holes as the majority charge carriers and an n-type semiconductor, which has electrons as the majority charge carriers are brought close together, electrons from the n-type semiconductor migrate to the p-type semiconductor and holes from the p-type semiconductor migrate to the n-type semiconductor and form what is known as a p-n junction. This migration of charge carriers is due to an imbalanced concentration of electrons and holes between the two regions. When light of sufficient energy strikes the p-n junction it excite electrons which were bound to atoms

in the valence band to a high energy level i.e. excited state, which means they are free to move; this is called the photovoltaic effect.

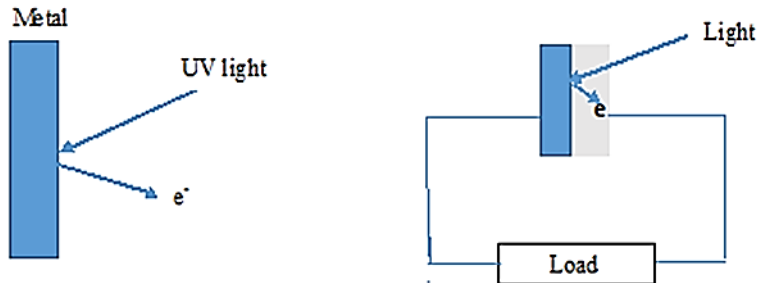


Figure 1. 3: The comparison of photoelectric effect on the left and photovoltaic effect on the right. The blue or ultraviolet light provides enough energy for an electron to escape completely from the surface of the metal.

The photoelectric effect was first reported in 1839 when Edmund Becquerel, the French physicist discovered that a silver coated platinum electrode immersed in an electrolyte produced an electric current when exposed to light [1.14]. In 1905, Einstein explained the photovoltaic effect and mentioned that it works on the same principle as the photoelectric effect (refer to figure 1.3 for his experimental setup). Later, William Adams and Richard Day confirmed the existence of this effect in solid materials. The first PV device based on silicon (Si) was made in Bell Laboratories in 1954 [1.15]. It had a PCE of 6% and ever since researchers have been trying to improve the PCE of PVs to the theoretical predicted value of 30% by using various types of materials and SC technologies which can be categorized as shown in figure 1.4 below [1.15].

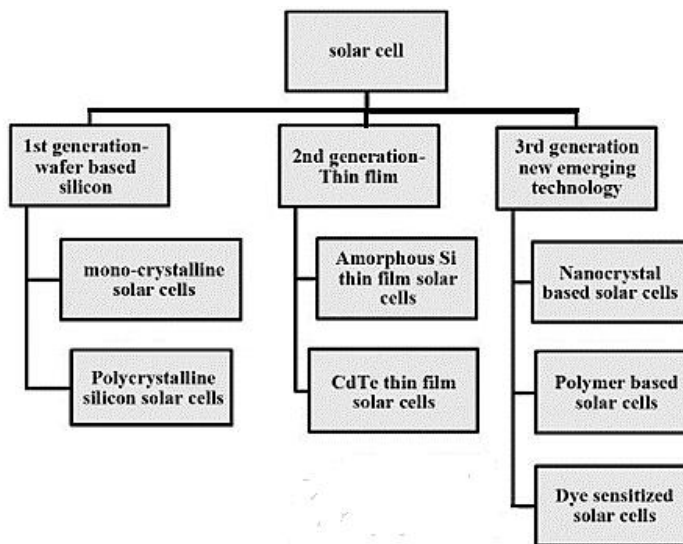


Figure 1. 4: Various type of materials and SC technologies that have been explored over the past decades [1.11].

1.2.1 First generation solar cells

First generation SCs, also known as wafer based SCs, are made of crystalline silicon (cSi), the commercially predominant PV technology, that includes materials like mono-crystalline silicon (mono-cSi) and poly-crystalline silicon (poly-cSi) [1.13, 1.16-1.17]. Mono-cSi SCs are made up of highly pure single cSi, while poly-cSi SCs consist of many crystals produced by cooling and solidifying molten Si which is then cut into thin plates. Mono-cSi SCs have high PCE, 14% - 18% [1.18]. However, purification methods used to produce high quality Si, coupled with high temperature and low throughput manufacturing techniques are economically unfriendly [1.7]. Therefore, poly-cSi SCs came in as alternative to reduce the cost of mono-cSi SCs. The cheaper processing and fabrication of poly-cSi SCs came at a cost of PCE which reduced to 13%-15% [1.18]. A major throwback associated with this PV generation is that the Si wafer cells consist of thick light absorbing layers which consequently make them heavier. Heavier and bulk solar modules need a lot of space for transportation and huge solar modules are required in case of high power application [1.19].

1.2.2 Second generation solar cells

Second generation SCs, also known as thin film SCs, are more cost effective than the first generation SCs as they need less material for construction [1.13]. Amongst other materials used in this SC generation we have amorphous silicon (a-Si), Cadmium telluride (CdTe) and copper indium gallium selenide (CIGS) [1.20].

The most popular thin film technology makes use of a-Si with PCE of 5-7 % up to 8-10 % for double and triple junction SCs, respectively [1.21]. The a-Si thin film SCs are made of non-crystalline Si and captured 25 % of the world market [1.22]. These are usually fabricated by depositing a thin silicon-dioxide (SiO_2) buffer layer on a soda-lime-silicate glass followed by a textured layer of indium tin oxide (ITO) to promote light trapping over the visible range [1.22]. They are normally dark brown in colour on the reflecting side and silver on the conducting side. A throwback associated with a-Si thin film SCs is their low and unstable efficiency.

CdTe SC describes a PV technology that is based on the use of CdTe, another crystalline compound semiconductor, which has a direct band gap of approximately 1.45 eV along with high optical absorption coefficient and chemical stability [1.11].

These properties make the absorption of light easier for CdTe thin film SCs, thus increasing the PCE to be between 9-11 %. However, there are environmental concerns with the production and disposal of PV cells containing heavy metals like CdTe [1.23].

CIGS thin film SCs are made-up of thin films of a compound semiconductor comprising four elements namely, copper (Cu), indium (I), gallium (Ga), selenide (Sn) which are direct band gap semiconductors [1.18]. Among thin film SCs, CIGS SCs have attracted researchers' attention due to its high efficiency, tunable band gap and cell stability with durability similar to that of Si SCs [1.24]. The normal structure of CIGS SC includes three major components, the CIGS absorber layer, a buffer layer and a conductive window layer [1.25]. High temperatures and vacuum processing in the fabrication of these SCs turned out to limit its application as far as cost is concerned. In response to this high cost associated with this specific PV technology, various fabrication methods have been explored. Among these fabrication methods, the solution ink method has turned out to be a promising candidate with high PCE of 15.2 % compared to a-Si and CdTe SCs [1.26]. However, high post-deposition annealing temperature remains an unresolved problem.

1.2.3 Third generation solar cells

Third generation SCs include nanocrystal, polymer, dye-sensitized SCs, etc. These are recent PV technologies which have not been commercialised yet as they are still in the research developing phase. Nevertheless, this generation of SCs has attracted a lot of attention over the past years because of its possibility to improve the PCE beyond the Shockley and Queisser limit of 31 % in a cost effective manner [1.27]. Third generation SCs do not depend only on a single p-n junction configuration for the separation of photon-induced charge carriers. They are configured as electron donor (D)-acceptor (A) bulk heterojunctions (BHJs) with staggered electronic band alignment.

Nanocrystal SCs also known as Quantum dot (QD) SCs are based on a substrate coated with a film of nano-crystals. The method that is often used to obtain thin films of nanocrystals is referred to as spin coating [1.13]. QD SCs attempt to replace bulk material SCs with the use of nano-crystals based on Si, CdTe or CIGS and the substrates are generally Si or organic conductors. The nanoscale size of the crystal

materials used allow the number of atoms to reside on their surface rather than their interior which subsequently give them improved characteristics and properties as compared to their bulk counterparts. Advantages associated with using nano-crystals as light harvesting candidates in SCs includes the following [1.28-1.29]: (i) the establishment of significant optical and electronic properties which can be tuned according to their size; this make them useful for multi-junction PVs where a variety of materials are used to improve the PCE by harvesting multiple portions of the solar spectrum (ii) the consumption of less material which leads to cost benefits and (iii) various possible preparation methods.

Dye-sensitised SCs (DSSCs) are low cost SCs with PCE of greater than 10 % [1.30-1.31]. They are photo-electrochemical systems based on a dye-molecule formed between a photo-sensitised anode and an electrolyte. Moreover, they are easy to prepare using a conventional roll-printing technique, semi-flexible and semi-transparent which grant them a wide variety of applications. The initial hope of DSSCs was that the technology would be substantially cheaper to fabricate than Si based cells. However, the decrease in Si prices has removed this hypothetical advantage therefore inhibiting its commercial availability.

Organic solar cells (OSCs) are the type of PVs that use organic materials to absorb light from the sun and transport photo-induced charge carriers to the external circuit to generate electricity. The device structure of this type of SCs can be either bilayer or BHJ structure. In either case the device consist of two electrodes (anode and cathode electrode), and electron D and A materials. The major reason for using organic materials is due to their high optical absorption co-efficient, which means that a very thin film is required to absorb a large amount of light [1.22]. Furthermore, organic molecules are solution-processable and cheap, which reduces production costs and allow large cells to be fabricated, thus increasing the surface area for light absorption [1.32]. The two major setbacks of this PV technology are low efficiencies and an instability issue, induced by humidity, oxygen, ultraviolet (UV) light and thermal stresses. In that regard, OPVs have not replaced the Si SCs, but are rather used for power mobile applications such as camping gear, smart wearables and smartphone chargers to name a few.

1.3 Conjugated polymers

Since the discovery of the conductive properties of doped polyacetylene (PAC) in 1997 [1.33], incredible progress has been made in synthesising conjugated polymers, understanding their properties and developing them for use in electronic and optical devices [1.34]. The discovery was accidental, this happened when a student of the Shirakawa's laboratory at the Tokyo Institute of Technology who was working on the preparation of the PAC added an excessive amount of catalyst in the reaction vessel. This resulted in the formation of the silver-coloured film instead of the expected dark powder [1.35]. The new product had different optical properties compared to the normal dark powder, therefore they tried to oxidize the PAC in order to obtain its normal optical properties using iodine vapour. However, that only resulted in an increase in the conductivity of the polymer [1.35]. This discovery led to the year 2000 Nobel Prize in Chemistry awarded to Alan Heeger, Alan MacDiarmid and Hideki Shirakawa. To date, polymers find their useful applications in a number of devices including light emitting diodes (LED's), photodetectors, PV cells and field effect transistors (FETs). These devices are important not only because of their outstanding performances but because of their cheap processing techniques such as spin coating, ink jet printing etc. [1.36-1.38].

1.3.1 Electronic structure of carbon

Organic polymers are semiconducting materials that are made up of carbon (C) and hydrogen (H) atoms with the addition of a few heteroatoms like oxygen (O), nitrogen (N), sulfur (S) etc. The mostly widely studied organic polymer are polythiophenes (PTs), polyphenylene vinylenes (PPVs), polypyrroles (PPy's) and polyanilines (PANI's) [1.39]. The conductivity in organic semiconductor is with respect to conjugation, i.e. the alternation of single and double bonds between C atoms [1.40]. Because organic semiconductors are based on C and the bonding of these C atoms plays a significant role in the conductivity, it is of importance to understand the electronic structure of C.

A C atom in its ground state has six electrons of which two of them occupy the 1s orbital, another two occupy the 2s orbital and the remaining two are found in the first two p orbitals which are $2p_x$ and $2p_y$ leaving the $2p_z$ orbital unoccupied, see figure 1.5 (a), (b), (c) and (d) for s, p_x , p_y , and p_z orbitals respectively. As a result, the ground state electron configuration of the C atom is able to make two covalent bonds only. However

C orbitals are able to hybridize and form sp, sp² or sp³ hybrid orbitals of equal energies. The sp hybrid orbitals are formed when one electron from the 2s orbital is promoted to the 2p orbitals and the empty s orbital mixes with one p orbital to give two sp orbitals. When an empty s orbital mixes with two p orbitals this gives three sp² orbitals, this is referred to as sp² hybridisation. The sp³ hybridisation occurs when an empty s orbital mixes with three p orbitals to give four orbitals of equal energies. These sp³ hybrid orbitals arrange themselves as far as possible from each other, thus making an angle of 109.5°. Figure 1.5 (e), (f) and (g) depict sp, sp² and sp³ hybrid orbitals respectively.

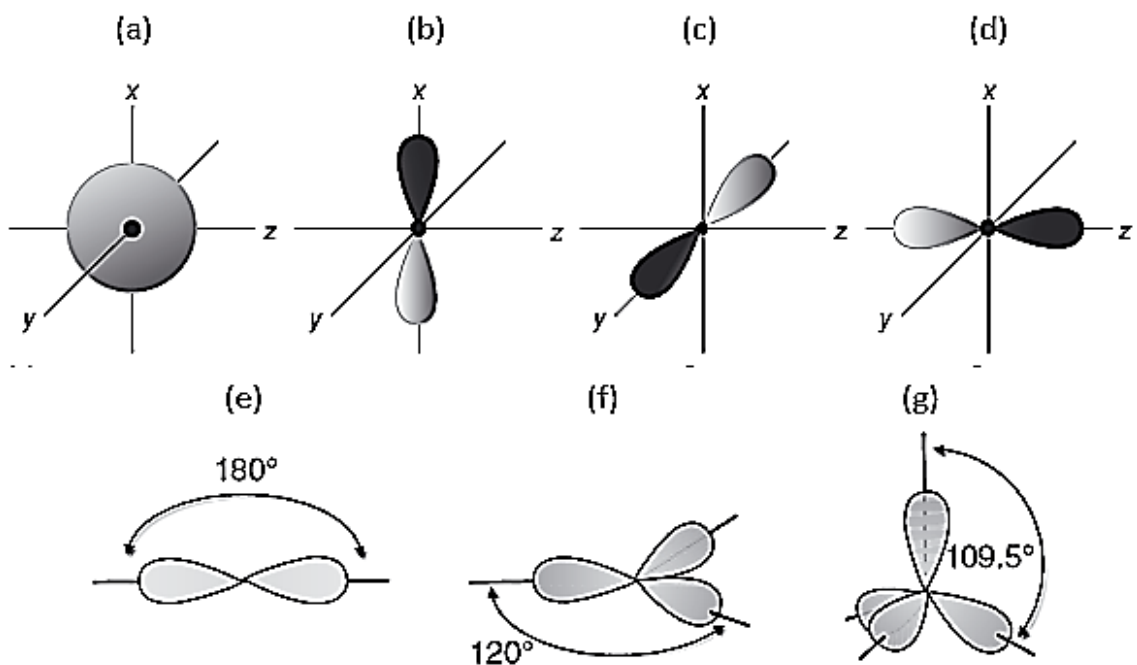


Figure 1. 5: The representation of the atomic s orbital (a), p orbitals (b-d) and hybrid orbitals (e-f) [1.40].

1.3.2 Type of bonds formed by carbon

The electrons in the sp³ hybridized orbitals can bond by overlapping with the 1s H atoms, this type of bond is referred to as sigma (σ) bond. As an example, a molecule which resembles this is methane (CH₄), see figure 1.6 (a). A unique property of C that makes it different to other elements and which allows it to make up many organic compound is its ability to bond with itself through covalent bonding. Thus an addition of two CH₄ molecules results in the formation of a new molecule known as ethylene (C₂H₄) which has covalent σ bonds between H-C and C-C atoms. The combination of two sp² hybridized C atoms leads to two C atoms being double bonded together by an overlap of sp² orbitals to form a σ bond and a side-to-side overlap of p_z orbitals to form

another bond known as the pi (π) bond. Thus the molecule is planar with a bond angle of 120° . The molecular structure of C_2H_4 depicted in figure 1.6 (b) is a good example of the C-C double bond. Another type of bond that C atoms form with itself is the triple bond found in a class of compound called alkynes. After the promotion of the 2s electron to the 2p orbital, the s orbital can mix with one p orbital to give two sp hybrid orbitals. The two remaining p orbitals (p_y and p_z) are used to make π bonds. The example for a triple bond between C atoms is shown in the acetylene (C_2H_2) molecule where two H atoms are bonded to one sp orbital, whereas the triple bond is formed by one σ bond from the other sp orbital and two π bonds from the side-to-side overlap of the two p orbitals, as depicted in figure 6(c). These sp hybrid orbitals position themselves 180° apart from each other.

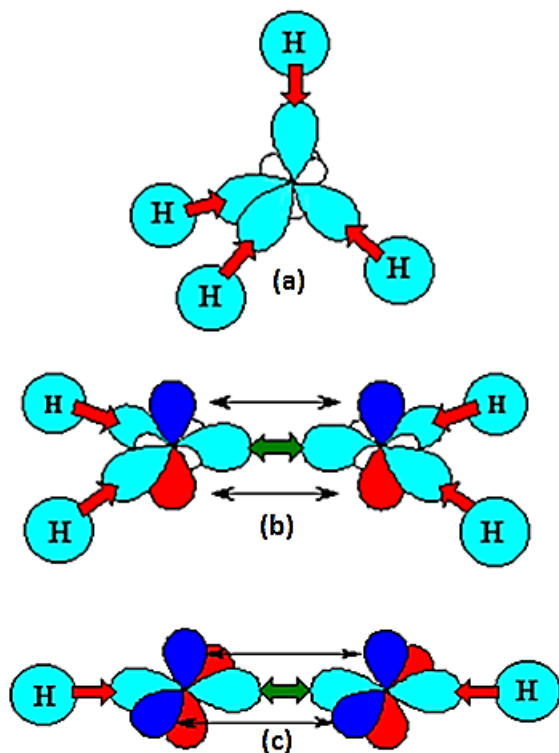


Figure 1.6: Types of carbon bonds depicted by the illustration of molecular structures of, (a) methane (CH_4), (b) ethylene (C_2H_4) and (c) acetylene (C_2H_2) [1.41].

1.3.3 Formation of molecular orbitals

The number of hybrid orbitals and the remaining p-orbitals in C atom determine the number and type of bonds it can form. A chemical bond can be considered as a pair of electrons that are shared between atoms. Because electrons are shared, they can no

longer be assigned to atomic orbitals but rather assigned to molecular orbitals and hence they are equally probable to be found orbiting around both sharing atoms. The resulting orbitals can be either π or σ -orbitals depending on the type of atomic orbitals combining. Kundu considered for example the combination of 1s orbitals of two H atoms during the formation of the H_2 molecule as shown in figure 1.7 [1.42]. Each H atom has just 1s orbital which contains just one electron so these atomic orbitals from both H atoms overlap which result in the formation of two molecular orbitals known as bonding (σ) and anti-bonding orbitals (σ^*). A bonding orbital can be viewed as the constructive interference while an anti-bonding orbital may be interpreted as a destructive interference of atomic orbitals.

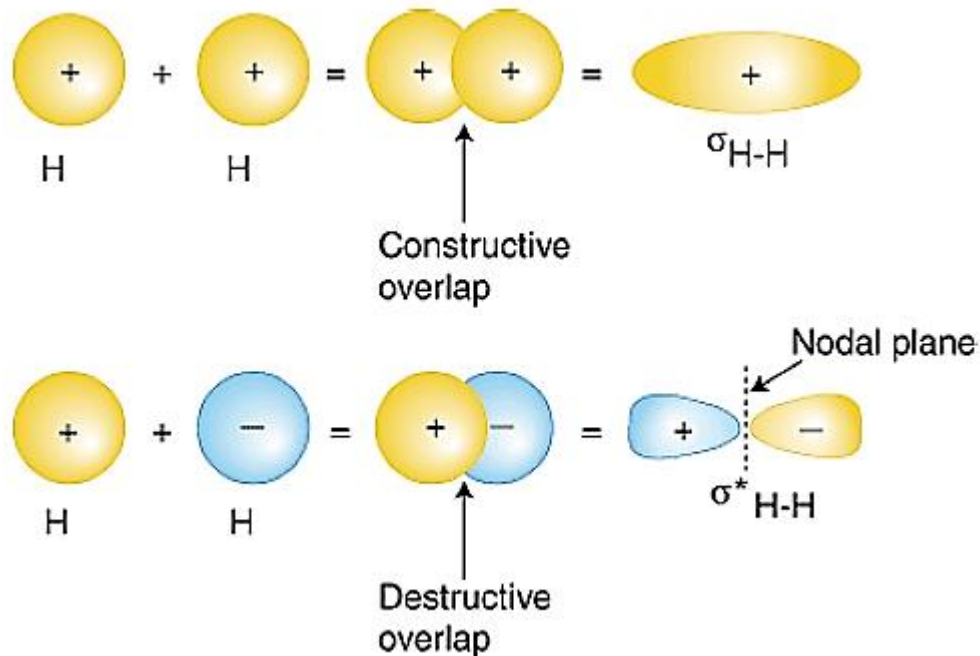


Figure 1.7: Schematic representation of the formation of the sigma (σ) bonding and anti-bonding (σ^*) orbitals in the combination of two hydrogen atoms [1.42].

The energy levels associated with these orbitals are different from that of the 1s orbital of each H atom, with the anti-bonding orbital being at a higher energy level than the bonding orbital. In general, it is essential to know the energy levels possessed by molecular orbitals if one need to understand the optical and electronic processes associated with organic molecules. During H_2 formation, each 1s orbital contributes one electron and when they combine, the pair will fill the low-lying bonding σ -orbital while leaving the high energy anti-bonding σ^* - orbital unfilled as depicted in figure 1.8. This

result in the strong net attractive interaction between the nuclei involved and hence the σ -bond holds the molecule together.

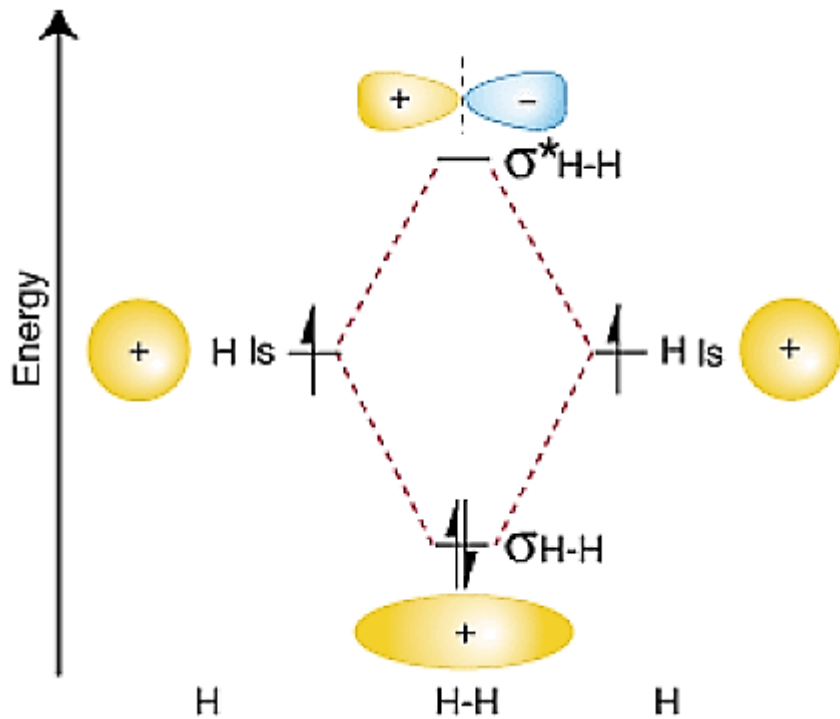


Figure 1.8: Energy levels of molecular orbitals of H_2 [1.42].

The bonding σ orbital is completely occupied hence it is called a highest occupied molecular orbital (HOMO) while an empty anti-bonding σ^* orbital is known as the lowest unoccupied molecular orbital (LUMO). These HOMO and LUMO respectively result in the formation of a valence band (VB) and the conduction band (CB) within the molecule or crystal, see figure 1.9 for the illustration of bands. The width of each band across the range of energy levels is called the band width while the range of energy between the bands is called the energy band gap (E_g) [1.42]. In conjugated polymers, the extent of delocalization and alternation of single and double bonds in C atoms determines the size of E_g [1.43]. Consequently, this band gap determines whether a polymer is a conductor, insulator or semiconductor. For conducting polymers there is no band gap i.e. $E_g = 0$ eV therefore the VB and the CB overlap, or the VB is not completely filled with electrons which allows an electron jump from lower atomic states to higher states within the valence band to be possible. For insulators the band gap is very large, i.e. $E_g > 3$ eV, hence electrons cannot be excited from the VB to the CB. For semiconductors, the band gap is smaller than that of insulators i.e. the E_g is between 0.1-

3 eV. This makes semiconductors to be insulators at temperature $T = 0$ K and conductors at $T = 300$ K.

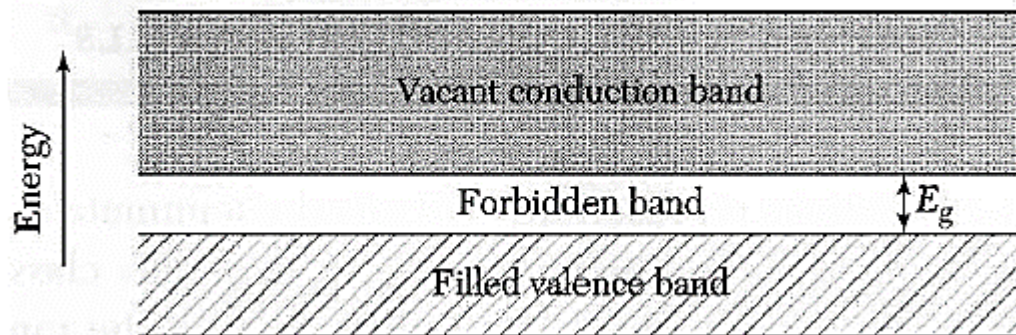


Figure 1. 9: Band scheme for semiconductors [1.44].

1.3.4 Polymer names, structures and average molecular weights

Polymers are large molecules composed of repeated subunits. Because of their broad range of properties, both synthetic and natural polymers play an essential and significant role in everyday life [1.45]. The production of polymers both natural and synthetic is via polymerization of many small building blocks called monomers. They have large molecular mass relative to small molecule compounds which as a result produces unique and exceptional physical properties including toughness, viscoelasticity and a tendency to form glasses and semi-crystalline structures. Commercially available semiconducting polymers like PPV derivatives and polyfluorenes (PFOs) are offered with molecular weight in the range of 50 000 – 100 000 atomic mass units, thus containing about 200 – 400 repeat units [1.46].

In general, it is very hard to find a sample of a synthetic polymer in which all the chains have the same molecular weight, instead we usually find the number-average molecular weight (M_N) or the weight-average molecular weight (M_w). The M_N is defined as the total weight of all the polymer molecules in a sample divided by the total number of polymers in a sample

$$\overline{M_N} = \frac{\sum N_i M_i}{\sum N_i} , \quad (1.1)$$

where N_i is the number of molecules of molecular weight M_i . The M_w is based on the fact that a bigger molecule contains more mass of the polymer sample than the smaller molecule. It is given as

$$\overline{M_W} = \frac{\sum N_i M_i^2}{\sum N_i M_i} . \quad (1.2)$$

where N_i is the number of molecules of molecular weight M_i .

In the most frequently used semiconducting polymers, the polymer back bone also referred to as the main chain polymer, determines useful properties of the polymer, like optical and electronic properties. The side chain polymer units give them the solubility in common solvents and control the separation between polymer chains once they are deposited in a film. Therefore, side chains control the degree of electronic interaction that take place between polymer chains. However, there are also other semiconducting polymers where the electronically active molecules reside on the side chains of the polymer. Nevertheless, most semiconducting polymers contain rings linked at different positions to form chains. Prefixes such as ortho (o), meta (m) and para (p) are used to indicate the positions at which connections are made. For instance, if we number atoms of a phenyl ring from 1 to 6 as shown in figure 1.10 (a), the substitution with two methyl groups (CH_3) changes a phenyl ring into xylene, also known as dimethylbenzene. The two methyl groups may be in ortho, meta, or para position with respect to each other as illustrated fig 1.10 (a), (b) and (c), respectively.

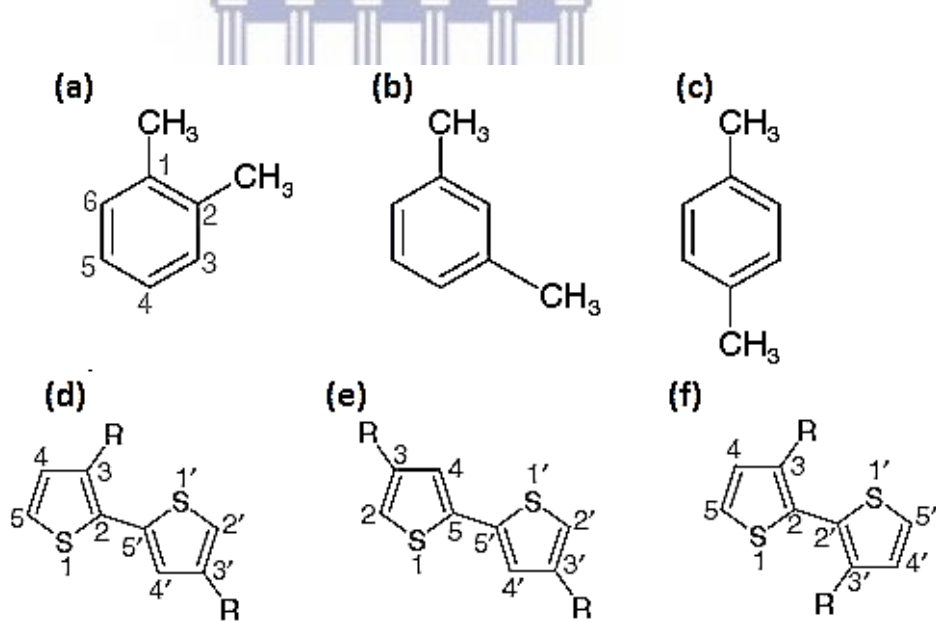


Figure 1. 10: Representation of phenyl and thiophene rings and their connections, (a), (b) and (c) shows, o-xylene, m-xylene and p-xylene respectively while (d), (e) and (f) shows head-to-tail, tail-to-tail and head-to-head thiophene rings connections respectively [1.46].

The relative position of side chains in a sequence can be relevant for some polymer chains. For instance, in a thiophene ring with atomic positions numbered as depicted in figure 1.10 (d), the alkyl side chain may be connected at position 3 or 4. If the side chain is at a consistent position, 3, and the repeat units is always connected from position 2 on one ring to position 5 on the next, it results in a structure with all side chains in the same direction. This is known as head-to-tail connection and it results in a regioregular polymer structure, see figure 1.10(d). Other combinations for example are tail-to-tail (figure 1.10 (e)), or head-to-head (figure 1.10 (f)) connections which results in structures with irregular side chain directions called regiorandom structures.

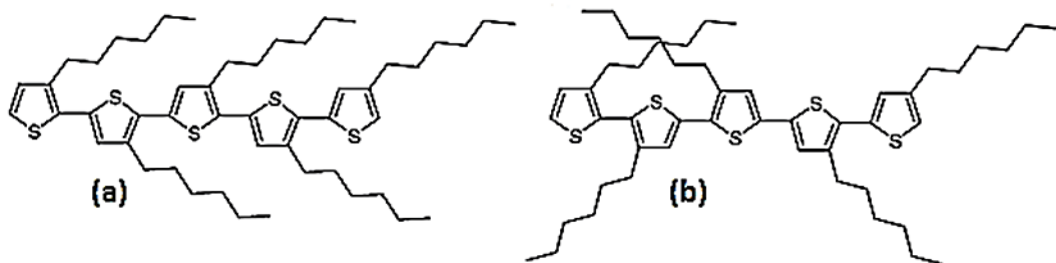


Figure 1. 11: Representation of the polymer structures, (a) regioregular and (b) regiorandom structure [1.46]

It has been reported that regioregular structures form more ordered film morphologies with improved charge carrier mobilities compared to regiorandom structures. Regioregular and regiorandom structures are depicted in figure 1.11.

1.4 Conjugated polymers for PV devices.

Conjugated polymers are used for different applications, however in this section we discuss conjugated polymers that are used mostly in photovoltaic (PV) devices. An overview of type of polymers used, preparation methods for thin films and properties of these polymers is given.

1.4.1 Types of polymers used in solar cells

Semiconducting polymers in the SC industry or research field are mostly used as electron donors of a SC. The most popular and successful polymers that have been employed can largely be divided into three groups, homopolymers, D-A polymers and quinoid type polymers [1.1]. (i) Homopolymers are formed when a single type of monomer is polymerised to form a macromolecule. Homopolymers include common

polymers like P3HT, MEH-PPV and MDMO-PPV just to name a few. (ii) D-A polymers contain alternating sequence of strong electron D and A units. In this category we can mention polymers like PCPDTBT and PDTPBT amongst others. These polymers have a reduced E_g value due to the internal charge transfer (ICT) from the D to the A units. (iii) Quinoid type polymers are formed when two aromatic units are fused together whereby one of the units has larger resonance energy than the other [1.47]. In the quinoid type polymers, the E_g reduction is accomplished by making the quinoidal structures more energetically favourable [1.48]. Figure 1.12 shows the structures of the above mentioned selected polymer and PCBM. It can be observed from figure 1.12 that there are many polymers available for exploration in SC applications. However, in this study we used rr-P3HT as a light absorbing material and the electron donor for our SCs. This polymer (rr-P3HT) was chosen for its good optical absorption and hole transporting ability arising from the crystalline ordering.

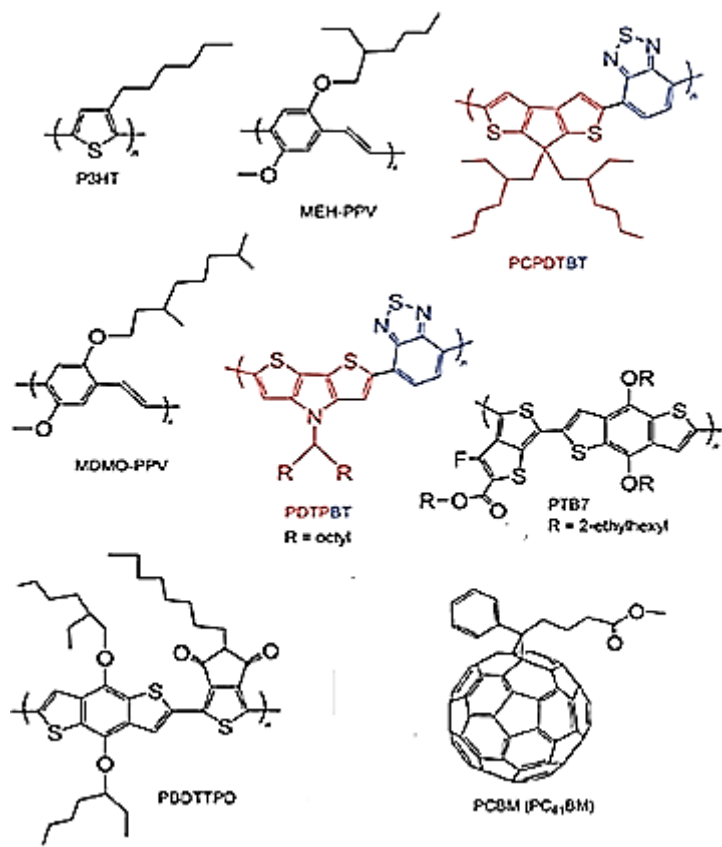


Figure 1. 12: Structural representation of selected D polymers and the most popular used fullerene (PCBM). The red and blue units are D and A units, respectively [1.1].

Even though this study focuses on the hybrid SCs where a photoactive layer comprises of a polymer and an inorganic nanoscale material; there was little chance that we could have finished off the study without mentioning an outstanding fullerene (PCBM) which is both an n-type semiconductor and good electron acceptor material. This fullerene has a good solubility in many organic solvents and has been used in many research works. The set-back with PCBM has been its poor ability to absorb light in the visible spectrum, thus it does not contribute effectively to the electrical output of the SC. As a result, fullerenes such as PC₇₁BM and PC₈₁BM which absorb more strongly in the solar spectrum have been developed. However, the strong light absorption ability in the latter has been achieved at the expense of the solubility in organic solvents.

1.4.2 Preparation methods of polymers

Material preparation methods for thin film SCs depend largely on the choice of material to be used. The main two techniques used are thermal evaporation and wet processing. For thermal evaporation, the material is heated in a vacuum chamber ($<10^{-5}$ mbar) until its surface atoms have sufficient energy to leave the surface. At that point they will traverse the vacuum chamber and coat a substrate positioned at a distance no longer than the mean free path of the evaporated particles [1.49]. On that note, contaminants like water and oxygen need to be reduced and can be further eliminated by either decreasing the pressure down to high vacuum ($<10^{-9}$ mbar) or performing the whole thermal evaporation process inside of a glove box with inert atmosphere. Small molecules are more stable than polymers hence evaporation is the best method to use in case of the former preparation.

The largely used wet processing technique for thin films involves dissolving a material of interest in an appropriate solvent. Polymers are thermally unstable and contain large molar masses; therefore polymer based thin films are prepared via solution based methods since they are highly susceptible to temperature. Various common techniques associated with solution based thin films preparations include spin coating and printing techniques, roll-to-roll technique and other film-forming techniques that are relevant such as spray coating, flexographic printing, and so forth. Most of these techniques require post preparation thermal treatments to evaporate the solvent and promote interpenetration between D and A materials in the case of BHJ SCs.

1.4.3 Electronic and optical properties

For the construction of SCs, the D polymer can be combined with either a fullerene and/or inorganic semiconducting nano-crystals in the BHJ structure. The optimisation of a SC involves fine-tuning electronic properties and interaction between the components forming the photoactive layer to enhance light absorption, generate charge carriers and transport them to their respective electrodes as effective as possible, before any recombination can occur. This ultimately focuses mostly on the electronic characteristic of individual components like absorption co-efficient, charge carrier mobility etc.

The most important property of a polymer in a SC is the value of closed circuit current density (J_{sc}) and open source voltage (V_{oc}) it can provide, which directly depend on the E_g and the HOMO-LUMO energy levels of that polymer. Figure 1.13 shows the energy levels of the selected most-used electron D polymers, and PCBM. Electrochemical E_g values for P3HT, MEH-PPV, PCPDTBT, MDMO-PPV, PDTPBT, PTB7, PBDTTPD and PCBM are 2.1, 2.4, 1.7, 2.3, 1.8, 1.85, 1.8 and 1.7 eV respectively [1.1, 1.50].

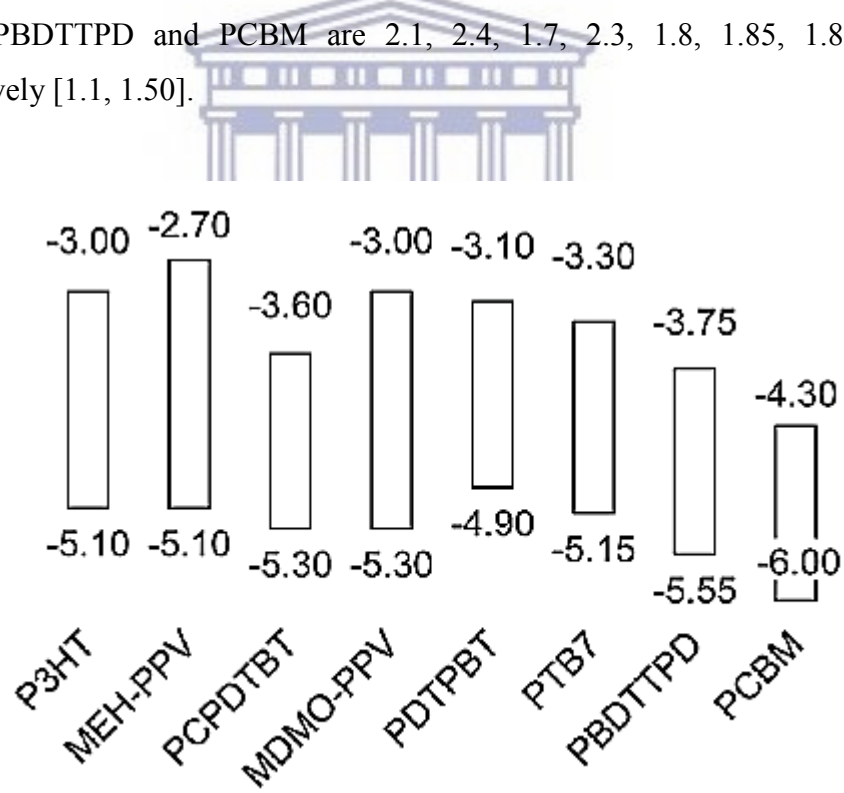


Figure 1. 13: HOMO and LUMO energy levels of selected polymers commonly used for SCs applications [1.1].

The majority of semiconducting polymers have a wide E_g (~ 2 eV), which limits the possible absorption of solar photons to about 30 %. However, due to high absorption co-efficients ($\sim 10^5 \text{ cm}^{-1}$) associated with organic materials only about 100 nm thick film is enough to absorb most of the solar irradiation. To depict the fraction of sunlight which contributes to energy conversion in some of these materials, absorption co-efficients of films are shown in comparison with an AM 1.5 standard solar spectrum in figure 1.14 below. P3HT is a special polymer due to its broad absorption spectrum in the visible range of the solar spectrum, as is evident in figure 1.14.

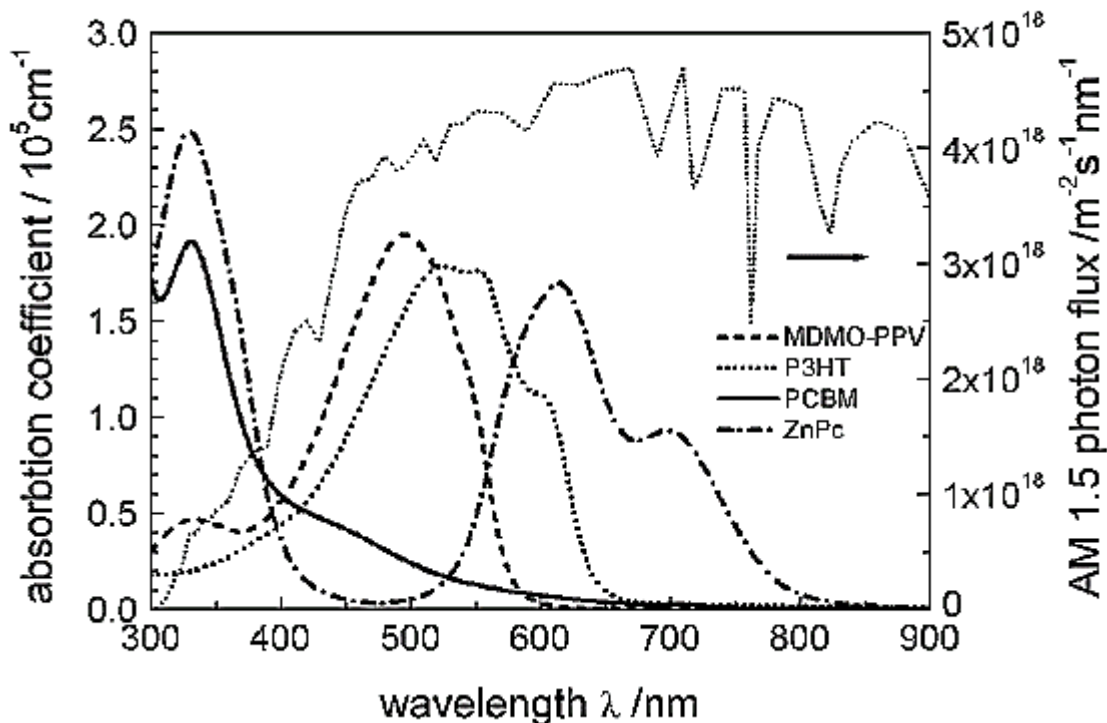


Figure 1. 14: Absorption co-efficients of films of selected materials compared to standard AM 1.5 terrestrial solar spectrum [1.49].

1.5 Silicon Nanowires (SiNWs)

The photoactive layers of our SCs will consist of rr-P3HT and different amount of SiNWs. The publication on Si wire growth was first presented by Treuting and Arnold in 1957, where in particular, they reported on the successful synthesis of Si whiskers (the term used then, to refer to Si wires) with a $<111>$ orientation [1.51-1.52]. A few years down the line after this publication, Wagner and Ellis reported on a ground breaking bottom-up technique of synthesising Si wires called the vapour-liquid-solid (VLS) mechanism of single crystal growth. This mechanism propelled the research interest in Si wires and up until today, it serves as the basis of a new research field of

SiNWs [1.53]. Wagner and Ellis observed that when a Si wafer coated with a metal catalyst like gold (Au) is heated to a temperature above 363°C in a vacuum chamber filled with a Si precursor like Silicon tetrachloride (SiCl_4) or silane (SiH_4), SiNWs growth resulted [1.53]. They claimed that as the Au coated Si wafer is heated small liquid Au-Si alloy droplet are formed, and upon its surface, a precursor molecule will break and result in Si being incorporated into the droplet. This continues until the droplet is supersaturated with Si which leads to Si freezing out at the bottom of the Si/droplet interface [1.53]. The continuation of this process then leads to the growth of a wire with the alloy droplet riding atop the growing wire and determining the size of the wire produced, see figure 1.15 (a) for the illustration of the mechanism. Si is known to oxidise easily if exposed to O at high temperature, hence it is useful to reduce this O level by lowering the pressure to high vacuum in order to obtain uniform SiNW growth. The advantage of using the VLS mechanism to synthesise SiNWs has been its ability to provide a controlled growth of wires in terms of the diameter and length which depend mostly on the Si precursor and temperature used during growth.

1.5.1 SiNWs synthesis methods

After Wagner and Ellis's work, different techniques have been developed and applied for the synthesis of nanowires (NWs). These techniques however can be divided into two groups, the bottom-up method which includes chemical vapour deposition (CVD), evaporation of silicon monoxide (SiO), Molecular Beam Epitaxy (MBE) and Laser Ablation, and the top-down method which includes electroless metal deposition and dissolution [1.54]. Figure 1.15 below depicts different methods (including VSL mechanism) used to synthesise NWs which were developed and applied after the VLS mechanism came into play.

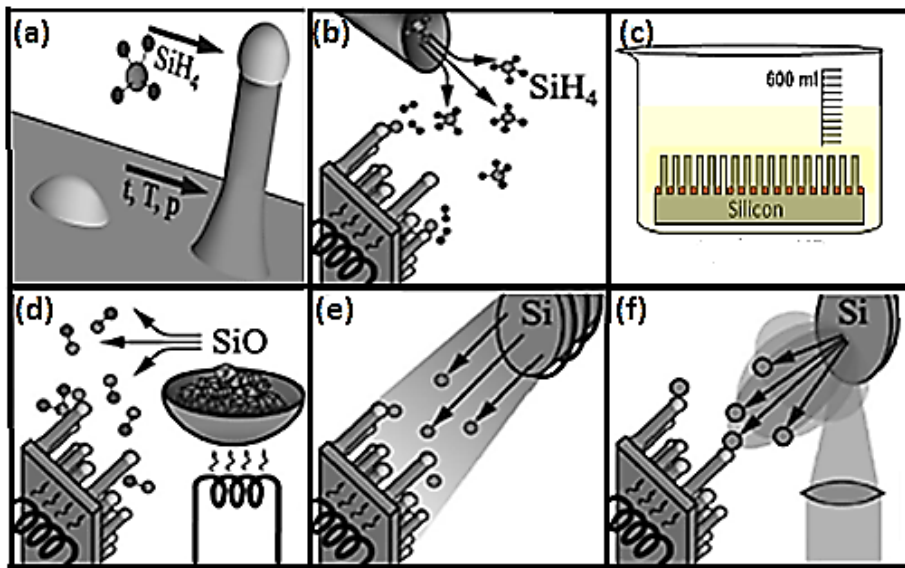


Figure 1. 15: Schematics of experimental setups for SiNW growth, (a) VLS mechanism, (b) CVD, (c) Electroless metal deposition and dissolution (d) Evaporation of SiO, (e) MBE and (f) Laser Ablation [1.52, 1.55].

1.5.1.1 Chemical vapour deposition

CVD is much like the VLS mechanism in the context of growth of SiNWs. At first CVD was aimed at depositing high-purity films of Si, however it was observed that contamination like Au particles turns out to cause the growth of SiNWs. Therefore, during the CVD process, a gaseous Si precursor which can be either SiH_4 or SiCl_4 acts as Si source. This gaseous Si precursor flows through the vacuum and get deposited onto the surface of the Si substrate whereupon it breaks down into its constituent which leads to growth of wires just like in the VLS mechanism, see figure 1.15 (b). The CVD enable the growth of SiNWs with a velocity that ranges from 10^{-2} to 10^{-3} nm/min [1.52]. A variety of CVD methods exist and are classified by parameters and the type of Si precursor used during the deposition. The remarkable aspect of CVD over the VLS mechanism is that the CVD method does not only control the growth of SiNWs but it also controls the properties of the SiNWs.

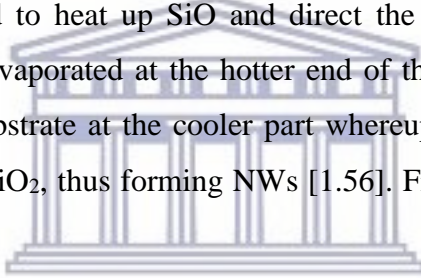
1.5.1.2 Electroless metal deposition and dissolution

In this technique, wire synthesis occurs in liquid media rather than the gaseous environment. Various solution based growth techniques have been utilised such as solution-liquid-solid (SLS), reaction-ion etching, metal assisted chemical etching (MACE) and other related methods. These solution based methods of synthesising SiNWs are more suitable methods to use if a high yield production of wires is desired. Amongst these methods, MACE has attracted a lot of researcher's attention lately.

MACE of the Si substrate to produce SiNWs begins with the deposition of metal particles like Au, silver (Ag) or Cu on the Si substrate. The metal coated Si substrate is then immersed in the etching solution of hydrofluoric acid (HF) and hydrogen peroxide (H_2O_2) where the wire growth actually occurs. The noble metal serves as a catalyst in the reaction by enhancing the oxidation of Si. Moreover, during etching the formation of SiNWs is due to the sinking of this noble metal, and longitudinal and lateral dissolution of the Si substrate, see figure 1.15 (c) for the representation of MACE technique.

1.5.1.3 Evaporation of SiO

This is another SiNWs synthesis technique that find it basis in the VLS mechanism in terms of the way in which SiNWs are grown. The exception is that the Si source (SiO) normally in powder form needs to be heated to high temperatures until it evaporates and flows through the tube of the furnace. In order to execute this, a two zone furnace and inert gas are required to heat up SiO and direct the evaporated SiO to the substrate respectively. SiO is evaporated at the hotter end of the tube and it flows with the gas stream toward the substrate at the cooler part whereupon it undergoes a disproportion reaction into Si and SiO_2 , thus forming NWs [1.56]. Figure 1.15 (d) shows the setup of this technique.



1.5.1.4 Molecular beam epitaxy (MBE)

Like most of the other techniques, MBE is based on the VLS concept. It is characterised by a uniform flux of Si atoms impinging on the Si substrate, see figure 1.15 (e) [1.57]. In contrast to CVD where the Au droplet acts like a catalyst to dissociate the precursor gas into its constituents, small metal clusters (Au droplets) act as seeds to initiate and later to continue the wire growth [1.58]. Just like in the case of CVD, the Au droplet absorb Si monomers from the source and as a result of supersaturation of dissolved Si atoms in the liquid droplet, Si atoms precipitate at the liquid-solid interface, allowing the wire growth. SiNWs in this case either form through layer growth by steps of monolayer-height or by the growth of small crystals at the interface [1.58].

1.5.1.5 Laser Ablation

Laser ablation is the process of removing material from a solid surface by bombarding it with a laser beam. At low laser flux, the material is heated by the absorbed laser energy and evaporates or sublimates (the transition of a material from a solid phase straight to

gas phase without passing through an intermediate liquid phase). At higher laser flux, the material is typically converted to plasma. Consider figure 1.15 (f) for the schematic representation of the setup of laser ablation growth of SiNWs. Here, a high power pulsed laser ablates Si target material which is placed in a tube furnace held at high temperature and purged with inert gas. The Si materials ablated from the target cool down in the vacuum and its atoms condense to liquid nano-droplets with the same chemical composition as the target, thus growing SiNWs via the VLS mechanism [1.59]. The resulting NWs growth velocities for this technique range in the order of micrometres per min [1.59, 1.60]. What is remarkable about this technique is that a Si substrate is not a prerequisite for SiNWs growth and that the constituents of NWs can be varied by changing the composition of the laser target.

Amongst all the aforementioned SiNWs growth techniques, in this study we are going to employ the solution based method, MACE. This technique is chosen because of its economical friendliness. A very high yield of SiNWs is required in this study since the wires are going to be mixed with large amount of polymer and the MACE method is efficient to achieve this. In addition, MACE of Si wafer to realise SiNWs is a simple synthesis method which enables the control of the size of the resulting SiNWs and the orientation of those SiNWs relative to the substrate.

1.5.2 Properties of SiNWs

The study and characterisation of nanostructured material properties are extremely important in order to determine suitable applications for those materials. Using different advanced instruments and techniques, one is able to study materials with absolutely small sizes and even examine individual atoms making up those materials. SiNWs have attracted enormous attention over the past decades largely because they exhibit properties that are different from their bulk Si counterpart. SiNWs have distinctive properties that vary with the diameter, length, crystallinity, growth orientation and the density [1.61].

1.5.2.1 Morphological and Structural properties

SiNWs can be synthesised under different conditions using different mechanisms and usually the resulting NWs have various morphologies. For an example, SiNWs produced via MACE contains nano-pores due to residual Ag nucleate that get attached into the side walls during NWs formation [1.62]. In addition, the crystal structure of

SiNWs consists of amorphous exterior shells and a single crystalline Si core. K. Peng et.al have reported that the growth direction of SiNWs varies with growth mechanisms and/or crystalline structure of the starting wafer [1.63-1.64]. Moreover, SiNWs that are synthesised using different techniques and conditions provide different X-ray diffraction (XRD) patterns. S.A. Razek et.al illustrated that the common diffraction peak of SiNWs synthesised via MACE is found around $2\theta = 33^\circ$ which they related to cSi [1.65]. Other peaks appeared around 38° and 44° which they ascribed to Ag oxide and Ag respectively.

1.5.2.2 Optical properties

The two major factors to be considered as far as optical properties of nanostructures are concerned are optical band gap and the light absorption ability. The objective has been to improve the indirect band gap of Si from 1.12 eV to an ideal band gap of 1.4 eV and minimise the reflection of incident light by improving the absorption co-efficient from $10^4 /cm$ to $10^5 /cm$ in order to enhance the cell efficiency [1.66-1.67]. For the past decade, the reflection properties of materials have been controlled by an antireflection coating, however the setback with regard to this practise has been the fact that it works efficiently only for limited spectrum and specific frequencies [1.68-1.70]. Various optical techniques have shown that properties of SiNWs are different from those of the bare Si wafer. The results show that modifying the surface morphology of Si to form SiNWs reduces the reflection loss of incident radiation over a broad spectral range. In the visible and near visible spectrum regions (NUV-Vis-NIR), the average optical reflectance is approximately 10% [1.71-1.72]. Another merit associated with SiNWs over bulk Si is that its optical band gap can be varied between 1.1 eV to 3.5 eV by varying the diameter in the range of 7-1.3 nm which could be explained by the quantum confinement (QC) effect [1.66, 1.67].

1.5.2.3 Electrical properties

Charge carrier mobility is one of the common essential electrical parameters that provide limitations to the electrical response of the device. Even though it has been a challenge to perform theoretical calculations and experimental work at the nanoscale, this has not stopped researchers from attempting to determine the charge carrier mobilities of SiNWs. Various mobility calculations involving small and large diameters of SiNWs have been performed employing different models and theories, where it has

been shown that the mobility varies with both axial orientation and diameter of SiNWs [1.73-1.75]. It has been further reported that the electron mobility of intrinsic SiNWs is greater than or equivalent to the hole mobility [1.76].

Similarly, various charge carrier mobility estimations through I-V characteristics of SiNWs had been underway. N. Singh et al. have reported electron and hole mobility of SiNWs with the diameter of $\sim 5\text{nm}$ to be approximately 750 and $325 \text{ cm}^2 /V.\text{s}$ respectively [1.77]. Byon et al. reported higher electron and hole mobilities that amounted to 770 and $510 \text{ cm}^2 /V.\text{s}$ respectively for SiNWs with diameters from $6\text{-}7 \text{ nm}$ [1.78]. The group of S-M. Koo reported an even higher electron mobility of $\sim 1000 \text{ cm}^2 /V.\text{s}$ for SiNWs with a diameter of $\sim 20 \text{ nm}$ which was then ascribed to induced strain due to the oxide layer [1.79]. Therefore from these results it could be inferred that charge carrier mobilities of SiNWs are strongly dependent on the actual physical structures, with large SiNWs diameters enhancing the mobility.

1.6 Device architecture

The most commonly used structure for hybrid SCs is a BHJ structure which consist of both electron D and A materials assembled together in one layer. In general the device consist of two electrodes, i.e. ITO and aluminium (Al), and an active layer (rr-P3HT: SiNWs) sandwiched in-between as illustrated in figure 1.16 [1.80]. Al has a lower work function as compared to ITO, which creates the electric field within the active layer that is responsible for exciton dissociation. The thickness of the active layer must be between $100\text{-}300 \text{ nm}$ and the phase domains of the inorganic and organic material making up the active layer need to be in the nanoscale ($\sim 20 \text{ nm}$) to allow excitons with short life time to diffuse to, and dissociate at the D-A interface. The poly (ethylene-dioxythiophene): poly (styrene sulfonate) (PEDOT: PSS) layer is a transparent thin layer deposited to improve the surface quality of ITO and facilitate the hole transportation [1.81].

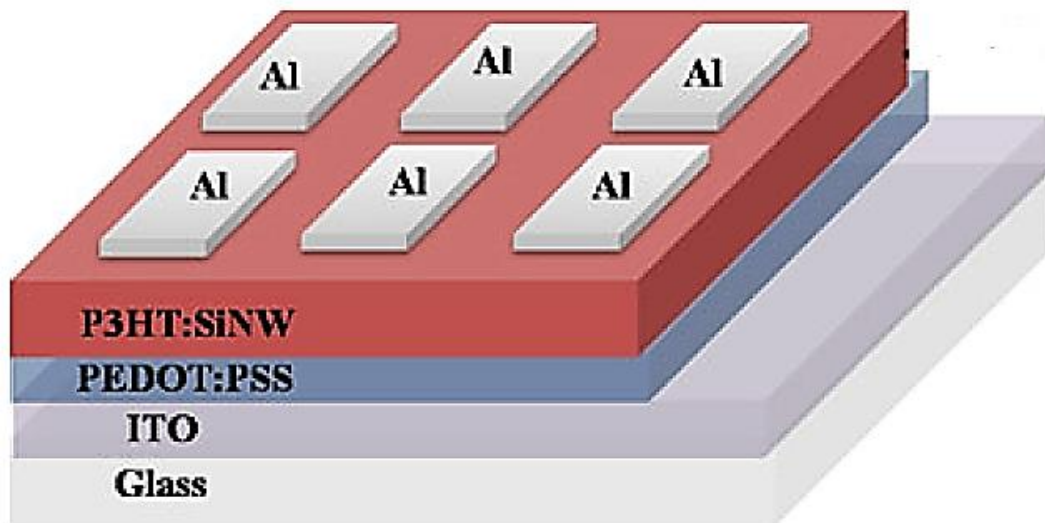


Figure 1. 16: Device architecture of BHJ photovoltaic [1.82]

1.7 Charge generation and transport processes within BHJ PVs.

The process of photo-generation and charge transport to the external circuit within BHJ PV devices, which is basically the conversion of light energy into electrical energy, can be separated into five steps as shown in figure 1.17 [1.1]. The first step is light absorption and generation of the exciton (figure 1.17 (a)). When photons with energy larger than the E_g of the D polymer strike the SC, electrons are excited from the HOMO to the LUMO of the electron D material. This leads to the formation of bound electron-hole pairs known as excitons [1.83]. These electron–hole pairs are bound together by the Coulomb attraction. The number of the initial exciton depends on the factors such as active layer thickness compared to the absorption length and also the E_g . The second step is the diffusion of excitons to the D- A interface (figure 1.17 (b)). The generated excitons are characterized by very short life times which limit their mobility. The overall mobility of the exciton is ~ 10 nm which is called the diffusion length [1.84]. This means that if excitons cover 10 nm before reaching the interface they will recombine and waste the photon energy that was absorbed. In contrast, upon arrival at the D- A interface they will successfully dissociate into free charge carriers (figure 1.17 (c)), if the energy difference between the LUMOs for D and A materials exceed the exciton binding energy, third step . The fourth step is free charge carrier transportation, i.e. the migration of free electrons and holes to their respective electrodes through interconnected electron A and D phases, respectively (figure 1.17(d)). Finally, the dissociated charges cross over the photoactive-layer/electrode interfaces (charge

transfer) to reach the external circuit (figure 1.17 (e)). The efficiency of charge transfer depends on the nature of electrical contacts between the active layer and the electrodes, energy levels of each phase, as well as the properties of the contact materials used [1.85].

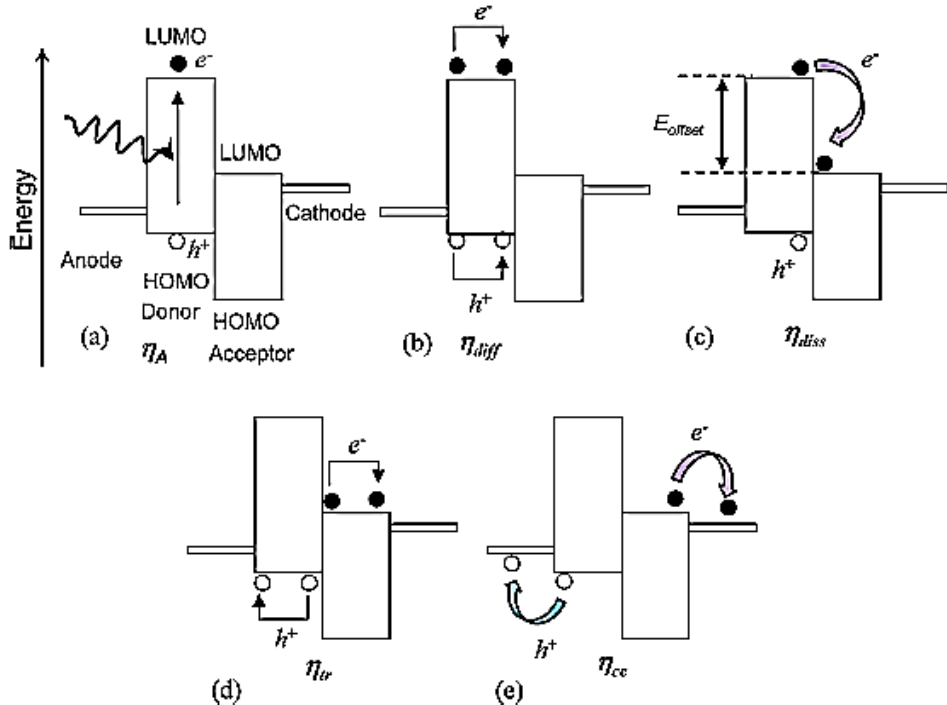


Figure 1. 17: Schematic representation of working mechanism of BHJ PV [1.1].

1.8 Device efficiency

The key characteristic of a SC is the ability to convert light into electricity, which is determined by performing the measurement of the current as a function of voltage. However, generally, the current density is used instead of current when characterising SCs to exclude the general current's dependency on the area of the SC. The current density-voltage (J-V) characteristic of a SC in the dark and under illumination is illustrated in figure 1.18. Under the dark condition the SC behaves as a diode and there is no current flow until the contacts start to inject a forward bias voltage that is larger than the open circuit voltage (V_{oc}). Under light illumination, the cell generates current with its maximum power point (P_{max}) in the fourth quadrant.

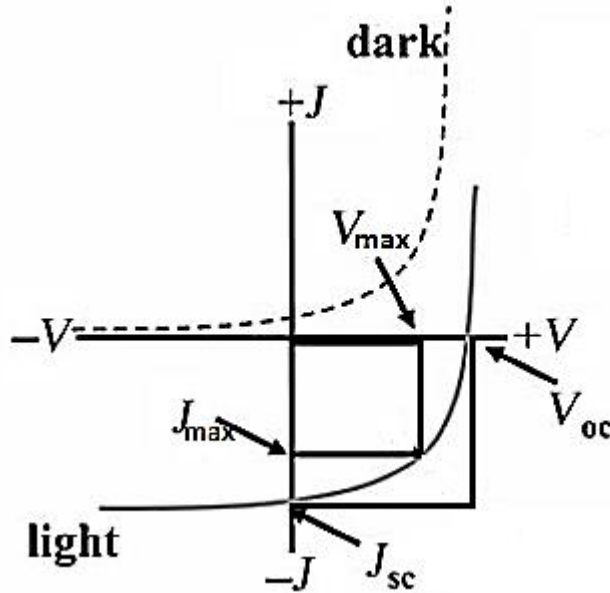


Figure 1. 18: J-V characteristic of a PV in dark condition and under light illumination which is obtained by applying variable voltage and measuring the current density obtain [1.86].

The PCE is the ratio of the power density (mW/cm^2) given by the sun to the maximum power density produced by a SC, normally it is expressed as a percentage:

$$\eta = \frac{P_{max}}{P_{source}}. \quad (1.3)$$

At any point along the J-V curve, power density is the product of J and V at that particular point, hence the maximum power density can be given as:

$$P_{max} = V_{max} \times J_{max}. \quad (1.4)$$

where V_{max} and J_{max} are the maximum voltage and the current density a SC can produce.

Now substituting equation (1.4) into (1.3) we get;

$$\eta = \frac{V_{max} \times J_{max}}{P_{source}}. \quad (1.5)$$

The Fill factor, denoted as FF is the ratio between the maximum power density generated by a SC and the product of V_{oc} and the short circuit current density, J_{sc} . Generally, BHJ SCs display a FF that is less than the ideal value of 1 due to physical

constraints of the SCs. Thus, FF determined by the charge carriers reaching the electrodes can be calculated as:

$$FF = \frac{P_{max}}{V_{oc} \times J_{sc}} = \frac{V_{max} \times J_{max}}{V_{oc} \times J_{sc}}. \quad (1.6)$$

The J_{sc} depends on the materials used to make the SC and the intensity of the incident light. Now making $V_{max} \times J_{max}$ the subject of the formulae and then substituting into (5) we get;

$$\eta = FF \times \frac{V_{oc} \times J_{sc}}{P_{source}} \quad (1.7)$$

Note that the FF has no units since it is just the fraction that multiplies the big box in order to get a smaller box in figure 1.18. In order to allow valid comparison of the device performance, an international standard for incident power density is used (i.e. P_{source}). This standard is an incident spectrum of AM 1.5 G, with the power density of 100 mW/cm² whilst the cell is at room temperature (25 °C) [1.7].

1.9 Thesis structure

1.9.1 Aim of the study

The aim of the study was to optimise the weight ratio of rr-P3HT: SiNWs and fabricate BHJ hybrid SCs with rr-P3HT: SiNWs as a photoactive layer, taking into account that the quality of the hybrid films strongly depend on the deposition technique, film processing conditions, choice of solvent and the nature of the substrate used. In order to achieve our ultimate goal, the sub-objectives were as follows; (1) the synthesis of SiNWs via MACE, (2) chemical detachment of as-synthesised SiNWs and (3) incorporating SiNWs into the polymer matrix.

1.9.2 Outline of the thesis

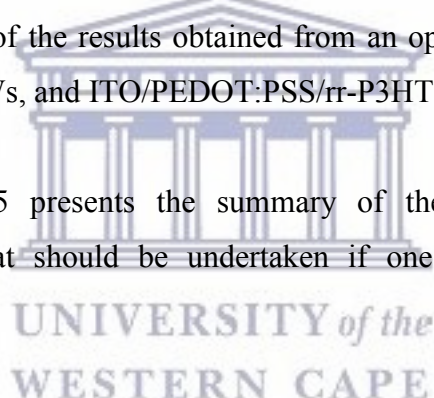
Chapter one highlights a number of things as part of the introduction and motivation of our study. In addition, a review of SCs illustrating different generation of SCs that have been explored thus far was given, recommending the use of organic/inorganic hybrid nanocomposites as photoactive hybrid SCs. Since rr-P3HT is a conjugated polymer, electronic and optical properties of the polymer was given, mentioning polymers that have attracted researcher's interest the most over the past decades. Furthermore, a review on the developments of SiNWs synthesis mechanisms was also given together with optical and electrical properties of SiNWs. The chapter concluded with the theory of device fabrication and characterisation.

Chapter two discusses all the analytical techniques used in the study. A brief introduction, the underlying theory and the experimental set-up is given for each technique. Detailed concepts of a technique where given when necessary (i.e. when it was going to give us better insight of the investigated aspect and improve our understanding of the results that were observed).

Chapter three introduces the formation of SiNWs by two step MACE and also reviews the etching mechanism of MACE. In addition, it outlines the solutions and sample preparation methods used to realise based-etched SiNWs, and lastly discusses the results that were obtained.

Chapter four introduces the mechanism and experimental set-up of spin coating which is the technique that was used for thin films deposition. This is followed by a thorough discussion of the results obtained from an optimisation study of composition of rr-P3HT and SiNWs, and ITO/PEDOT:PSS/rr-P3HT:SiNWs/Al SCs characterisation.

Finally, chapter 5 presents the summary of the main findings and provides recommendations that should be undertaken if one needs to improve the results obtained.



References

- [1.1] Yan J and Saunder B R 2014 *RSC Advances* **4** 43286
- [1.2] Stocker T F et al 2013: Technical Summary. In: Climate Change 2013: The Physical Science Basis. Contribution of Working Group I to the Fifth Assessment Report of the Intergovernmental Panel on Climate Chang. Cambridge, United Kingdom and New York, NY, USA: *Cambridge University Press*
- [1.3] Field C B et al 2014: Climate Change 2014: Impacts, Adaptation, and Vulnerability. Summaries, Frequently Asked Questions, and Cross-Chapter Boxes. A Contribution of Working Group II to the Fifth Assessment Report of the Intergovernmental Panel on Climate Change. Geneva, Switzerland: *World Meteorological Organization*
- [1.4] International Energy Agency. (2013), World Energy Outlook. [Online]. Available at: <https://www.iea.org/publications/freepublications/publication/WEO2013.pdf> (Accessed 13 March 2016).
- [1.5] International Energy Agency (2016), World Energy Outlook Executive Summary. [Online]. Available at: <https://www.iea.org/publications/freepublications/publication/WorldEnergyOutlook2016ExecutiveSummaryEnglish.pdf> (Accessed 13 March 2016).
- [1.6] Yu P, Wu J, Liu S, Xiong J, Jagadish C and Wang Z M 2016 *Nano Today* **11** 704
- [1.7] Johnson G 2009 *National Geographic*
- [1.8] Khlyabich P P, Burkhardt B, Rudenko A E and Thompson B C 2013 *Polymer* **54** 5267
- [1.9] Bertolli M 2008 *Solar Cell Materials*
- [1.10] European Photovoltaic Industry Association (2013), Global market outlook for photovoltaics 2013-2017. [Online]. Available at: <http://www.fotovoltaica.com/fv-look.pdf> (Accessed 14 March 2016).
- [1.11] Sharma S, Jain K K and Sharma A 2015 *Materials Sciences and Applications* **6** 1145
- [1.12] Rana S 2013 *International Journal of Scientific & Technology Research* **1** 77
- [1.13] Bagher A M, Vahid M M A and Mohsen M 2015 *American Journal of Optics and Photonics* **3** 94
- [1.14] Markvart, T. (1994). *Solar Electricity*. 2nd ed. Chichester, UK: John Wiley & Sons, pp.1-4.

- [1.15] Chapin D M, Fuller C S and Pearson G L 1954 *Journal of Applied Physics* **25** 676
- [1.16] McEvoy, A., Castaner, L. and Markvart, T. (2012) *Solar Cells, Materials, Manufacture and Operation*. 2nd ed. Oxford: Elsevier Ltd., pp.3-25.
- [1.17] Wang X, Liu D and Li J 2010 *Frontiers of Chemistry in China* **5** 45
- [1.18] Srinivas B, Balaji S, Babu M N and Reddy Y S 2015 *International Journal of Engineering Research-online* **3** 178
- [1.19] Tsoutsos T, Frantzeskaki N and Gekas V 2005 *Energy Policy* **33** 289
- [1.20] Choubey P C, Oudhia A and Dewangan R 2012 *Recent Research in Science and Technology* **4** 99
- [1.21] Parida B, Iniyam S and Goic R 2011 *Renewable and Sustainable Energy Review* **11** 1625
- [1.22] Mohd-Nasir S N F, Sulaiman M Y , Ahmad-Ludin N, Sopian K and Mat-Teridi M A 2014 *International Journal of Photoenergy* **2014** 370160
- [1.23] Noice L, Goncher G and Solanki R 2008 *PSU McNair Scholar Online Journal* **2** 309
- [1.24] Aguilera L, Vida I J, Wahnon P, Reining L and Botti S 2011 *Physical Reviews B* **84** 085145
- [1.25] Singh M, Jiu J, Sugahara T and Suganuma K 2014 *Applied Materials & Interfaces* **6** 16297
- [1.26] Todorov T, Gunawan O, Gokmen T and Mitzi D B 2013 *Progress in Photovoltaics* **21** 82
- [1.27] Shockley W and Queisser H J 1961 *Journal of Applied Physics* **32** 510
- [1.28] Etgar L 2013 *Materials* **6** 445
- [1.29] Sethi V K, Pandey M and Shulka P 2011 *International Journal of Chemical Engineering and Application* **2** 17
- [1.30] Li B, Wang L, Kang B, Wang P and Qiu Y 2006 *Solar Energy Materials and Solar Cells* **90** 549
- [1.31] Suhami S, Shahimin M M, Alahmed Z A, Chysky J and Reshak A H 2015 *International Journal of Electrochemical Science* **10** 28
- [1.32] Zhu Z, Waller D, Gaudiana R Morana M, Muhlbacher D, Scharber M and Brabec C 2007 *Macromolecules* **40** 1981

- [1.33] Chiang C K, Fincher C R ,Jr., Park Y W, Heeger A J, Shirakawa H, Louis E J ,Gau S C and MacDiarmid A G 1977 *Physical Review letters* **39** 1098
- [1.34] Nalwa, H. (1997). Handbook of organic conductive molecules and polymers. 1st ed. New York: Wiley.
- [1.35] Shirakawa H, Louis E J and MacDiarmid A G, Chiang C K and Heeger A 1977 *Journal of Chemical Society, Chemical Communication* **16** 578
- [1.36] Kelley T W, Baude P F, Gerlach C, Ender D E , Muyres D , Haase M A , Vogel D E , Theiss. S D 2004 *Chemistry of Materials* **16** 4413
- [1.37] Forrest S R 2004 *Nature* **428** 911
- [1.38] Tsutsui T and Fujita K 2002 *Advance Materials* **14** 949
- [1.39] Molapo K M., Ndangili P M, Ajayi R F, Mbambisa G, Mailu S M, Njomo N, Masikini M, Bake P and Iwuoha E I 2012 *International journal of electrochemical science* **7** 11859
- [1.40] Pope, M. and Swenberg, C.E. (1999). *Electronic Processes in Organic crystal and Polymers*. 2nd ed. USA: Oxford University Press.
- [1.41] Structur Van de Materie. *Intermezzo-Structuur*, 2012. [Online]. Available at: <https://mijninteresses.wordpress.com/2012/04/15/intermezzo-structuur/> (Accessed 16 March 2016).
- [1.42] Kundu S 2015 *International Journal of Applied Sciences* **1** 12
- [1.43] Cheng Y, Yang S H and Hsu C 2009 *Chemical Reviews* **109** 5868
- [1.44] Kittel, C. (2005). Semiconductors, *Introduction to Solid State Physics*. 8th ed. USA: John Wiley & Sons, Inc, pp.185-219.
- [1.45] Painter, P.C. and Coleman, M.M. (1997). *Fundamentals of polymer science: An introductory text*. 2nd ed. Lancaster Pa, D.C.: Technomic Publishing Company.
- [1.46] Kohler, A. and Bassler, H. (2015). The electronic structure of organic semiconductor, *Electronic Processes in organic semiconductors*. 1st ed. Weinheim, Germany: Wiley-VCH Verlag GmbH & Co. kGaA, pp.1-86.
- [1.47] Zhou H, Yand L and You W 2012 *Macromolecules* **45** 607
- [1.48] Chen Y-H, Hou J, Zhang S, Liang Y, Yang G, Yang Y, Yu L, Wu Y and Li G 2009 *nature photonics* **3** 649
- [1.49] Hoppe H and Sariciftci N S 2004 *Journal of Material Research* **19** 1924
- [1.50] Scharber M C, Mullbacher O, Koppe M , Denk P, Waldouf C , Heeper A J and Brabec C J 2006 *Advanced Materials* **18** 789
- [1.51] Treuting R G and Arnold S M 1957 *Acta Metallurgica* **5** 598

- [1.52] Schmit V, Wittemann J V, Senz S and Gosele U 2009 *Advanced Materials* **21** 2681
- [1.53] Wagner R S and Ellis W C 1964 *Applied Physics Letters* **4** 89
- [1.54] Hasan M, Huq M F and Mahmood Z H 2013 *SpringerPlus* **2** 151
- [1.55] Hung Y Jr, Lee S-L, Wu K-C, Tai Y and Pan Y-T 2011 *Optics express* **19** 15792
- [1.56] Pan Z W, Dai Z R, Xu L, Lee S T and Wang Z L 2001 *Journal of Physical Chemistry B* **105** 2507
- [1.57] Zakhrov N D, Werner P, Gerth G, Schubert L and Gosele U 2006 *Journal of Crystal Growth* **290** 6
- [1.58] Werner P, Zikharov D, Gerth G, Schubert L, Gosele 2006 *International Journal of Materials Research* **97** 1008
- [1.59] Morale A M and Lieber O M 1998 *Science* **279** 208
- [1.60] Zhang Y F, Tang Y A, Wang N, Yu D P, Lee C S, Bello I and Lee S T 1998 *Applied Physics Letters* **72** 1835
- [1.61] Nassiopoulou A G, Gianneta V and Katsogridakis C 2011 *Nanoscale Research Letters* **6** 597
- [1.62] Hochbaum A I, Gargas D, Hwang Y J and Yang P 2009 *Nanoletters* **9** 3550
- [1.63] Peng K, Lu A, Zhang R and Lee S T 2008 *Advanced Functional Materials* **18** 3026
- [1.64] Smith R L, and Collins S D 1992 *Journals of Applied Physics* **71** R1
- [1.65] Razek S A, Swillam M A and Allam N K 2014 *Journal of Applied Physics* **115** 194305
- [1.66] Ramanujam J, Shiri D and Verma A 2011 *Materials Express* **1** 105
- [1.67] Hutagalug S D, Fadhal M M, Areshi R A and Tan F D 2017 *Nanoscale Research Letters* **12** 425
- [1.68] Srirastava S K, Kumar D, Singh P K, Kar M, Kumar V, Husain M 2010 *Solar Energy Materials and Solar cells* **94** 1506
- [1.69] Li S , Ma W, Chen X , Xie K , Li Y, He X , Yang X , Lie Y 2016 *Applied Surface Science* **369** 232
- [1.70] Zhang C, Li S, Ma W, Ding Z, Wan X, Yang J, Chen Z, Zou Y, Qiu J 2017 *Journals of Materials Science: Materials in electronics* **28** 8510
- [1.71] Yu P, Wu J , Liu S, Xiong J , Jagadish C and Wang Z M 2016 *Nano Today* **11** 704

- [1.72] Jia X, Zhou C and Wang W 2017 *Nanoscale Research Letters* **12** 193
- [1.73] Buin A K, Verma A and Anantram M P 2008 *Journal of Applied Physics* **104** 053716
- [1.74] Buin A K, Verma A, Svizheko A and Anantram M P 2008 *Nano Letters* **8** 760
- [1.75] Ramayya E B, Vasileska D, Goodnick S M and Knezevic I 2008 *Journal of Applied Physics* **104** 063711
- [1.76] Verma A, Buin A K and Anantram M P 2009 *Journal of Applied Physics* **106** 113713
- [1.77] Singh N, Agarwal A, Bera L K, Liow T Y , Yang R, Rustagi S C, Tung C H, Kumar R, Lo G Q, Balasubramanian N and Kwong D L 2006 *IEEE Electron Device Letters* **27** 383
- [1.78] Byon K, Tham D and Fischer J E 2007 *Applied Physics Letters* **90** 143513
- [1.79] Koo S-M, Fujiwara A, Han J-P, Vogel M., Richer C A and Bonevich J E, 2004 *Nano Letters* **4** 2197
- [1.80] Borchert H 2010 *Energy and Environmental Science* **3** 1682
- [1.81] Lee J J, Lee S H, Kim F S, Choi H H, Kim J H 2015 *Organic Electronics* **26** 191
- [1.82] Azizi S, Braik M, Dridi C, Ouada H B, Ryback A, Devenas J 2012 *Applied Physics A* **108** 99
- [1.83] Spanggaard H, Krebs F C 2004 *Solar Energy Materials & Solar Cells* **83** 125
- [1.84] Dimitrov S D, Durrant J R 2014 *Chemistry of Materials* **26** 616
- [1.85] Moliton A and Nunzi J M 2006 *Polymer International* **55** 583
- [1.86] Thompson B C, Frechet B M J 2008 *Angewandte Chemie International Edition* **47** 58

2 ANALYTICAL TECHNIQUES

2.1 Introduction

In order to analyse data, discuss results and come up with solid conclusions, one needs to fully understand the characterising technique to be employed. In this chapter we discuss these analytical techniques in detail. The table below summarises the analytical techniques employed in this study.

Table 2. 1: Analytical technique used in this study

Technique	Information obtained
Scanning Electron Microscopy	Morphology and topography of SiNWs
High Resolution Transmission Electron Microscopy	Morphology of rr-P3HT/SiNWs at high resolution
Dektak Profilometry	Thickness and roughness of thin films
Hall Effect	Conductivity of rr-P3HT and hybrid films
Ultraviolet-visible spectroscopy	Optical properties of thin films
Photoluminescence	Electronic structures and degree of quenching

2.2 Scanning Electron Microscopy

2.2.1 Introduction

A scanning electron microscope (SEM) is the type of microscope that uses a focused beam of electrons to produce a three dimensional image of an object. The electrons interact with the atoms of the sample and provide different signals that contain information about the composition and physical features of the surface of the sample. SEM renders its usefulness to a wide range of disciplines including biomedical science, and semiconductor industries because of the short wavelength of electrons which range between 0.01 and 0.001 nm and the image resolution it can achieve which is 1nm [2.1]. The abundant and the most commonly used imaging signal in SEM is from secondary electrons. These are electrons which escape from the sample with energies below 50 eV [2.1]. The yield of secondary electrons that can be detected among other things depends on the angle of interaction between the beam of electrons and the sample. The starting point of the SEM characterisation is the emission of the beam of electrons from the electron gun (filament and Wehnelt cup) which is positioned on top of the instrument column [2.2] as shown in figure 2.1. An electron gun is made of a piece of Tungsten, usually a wire (filament) bent into a hairpin which acts as the cathode. This filament is heated by a passage of current to about 2800K while being held at high negative potential with respect to the anode and the rest of the microscope [2.3], thus producing the electron beam. This is referred to as thermionic emission of electrons. The electron beam is accelerated to an energy which is usually in the range of 1-30 keV toward the anode. Then, it is focused and demagnified until it reaches the sample with a diameter of only 2-10 nm as it passes through a condenser lens, objective lens, scanning coils and apertures. In addition to its focusing capability, an objective lens determines the intensity of the beam upon striking the sample and control the image brightness as well.

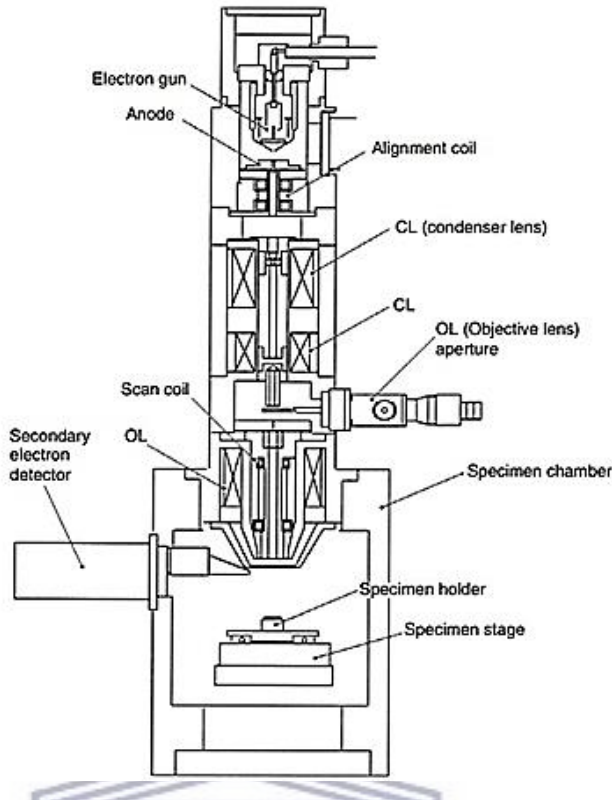


**Figure 2. 1: Schematic diagram of scanning electron microscope (JSM-5410,
courtesy of JEOL, USA)**

2.2.2 Resolution

The concept of resolution is very important in electron microscopy. It is defined as the closest spacing of two points which can be clearly seen through a microscope as to be separate entities. In an optical microscope, the resolution is limited by the diffraction effect and fineness of lenses. In this type of analysing technique, light must pass through a series of restricted openings including lenses and apertures. The fundamental maximum to the resolution of any optical system is given by the Ernst Abbe diffraction relation [2.4]:

$$d = \frac{0.61\lambda}{\mu \sin \alpha}, \quad (2.1)$$

where d is the limit of resolution, λ is the illumination wavelength, μ is the refractive index, and α is the aperture angle. The product $\mu \sin \alpha$ is called the numerical aperture. The resolution of the SEM depends on the wavelength of the electrons, the electron optical system that produces the electron beam and an interaction volume which is the volume of specimen material that interacts with the electron beam. The resolution of the SEM is not high enough to image individual atoms because the spot size and the

interaction volume are very large compared to the atomic diameter. Nevertheless, the SEM has certain advantages which include the ability to image a large area of the specimen, and the capability to image bulk materials. Furthermore, SEM provides a variety of analytical modes for measuring the composition and properties of the specimen.

2.2.3 Depth of focus, aperture size and working distance

The depth of focus denoted as D in figure 2.2 is defined as the range of positions at which an image can be viewed without appearing out of focus for a fixed position of an object [2.5]. In essence, the specimen will appear acceptably sharp in the magnified image within this length and the specimen outside this length will be enlarged into an out of focus blur which will deteriorate the whole image. It may be only a fraction of a micrometre in some cases and it depends on the aperture of the objective lens and the working distance (distance between the objective lens and the top part of the specimen surface). Fig 2.2 (a) and (b) show that D can be increased by reducing the size of the final aperture while the comparison of fig 2.2 (b) and (c) show that the working distance affects the depth of focus as well, i.e. a shorter working distance reduces D.

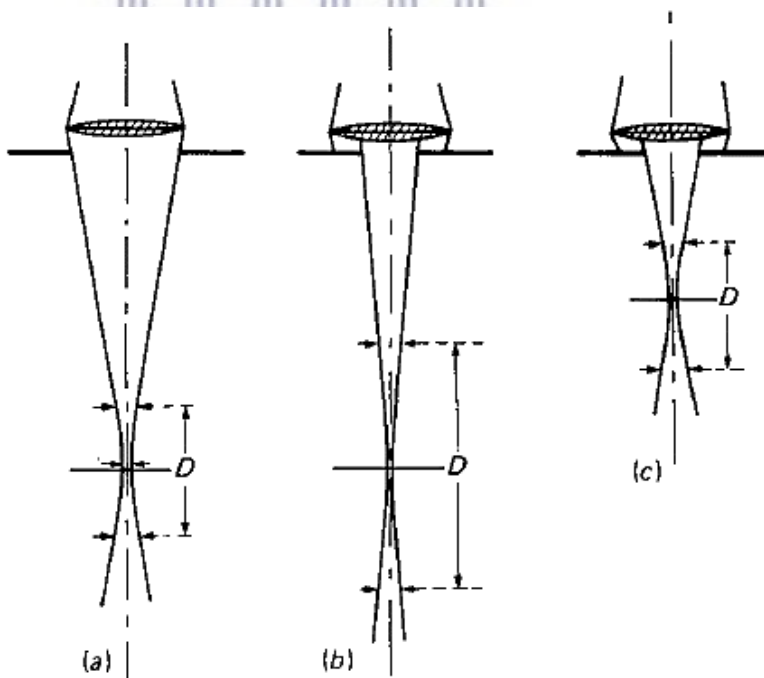


Figure 2. 2: Schematic depicting the relationship between the aperture size and the depth of focus (Fig 2.2 (a) and (b)), and the relationship between the working distance and the depth of focus (fig 2.2 (b) and (c)) [2.6].

2.2.4 Electron beam and specimen interaction

In order to be able to interpret the image, diffraction pattern or analytical spectrum that is produced by a microscope, it is important to understand the interaction between the electron beam and the specimen. In SEM, when primary electrons hit the specimen, some electrons enter and pass through the specimen (transmitted electrons), while others are scattered from the surface of the specimen to form an image. There are two types of scattering that might occur, elastic or inelastic scattering. Elastic scattering occurs when the electron trajectory changes, but the kinetic energy and the velocity remain constant. This type of scattering produces back-scattering electrons (BE), as shown in figure 2.3. In inelastic scattering, the trajectory of the primary electron is changed slightly while the energy is lost through interaction with electrons of the atoms in a specimen. Inelastic interaction produces various signals including secondary electrons (SE), cathodoluminescence, X-rays, auger electrons etc. as shown in figure 2.3.

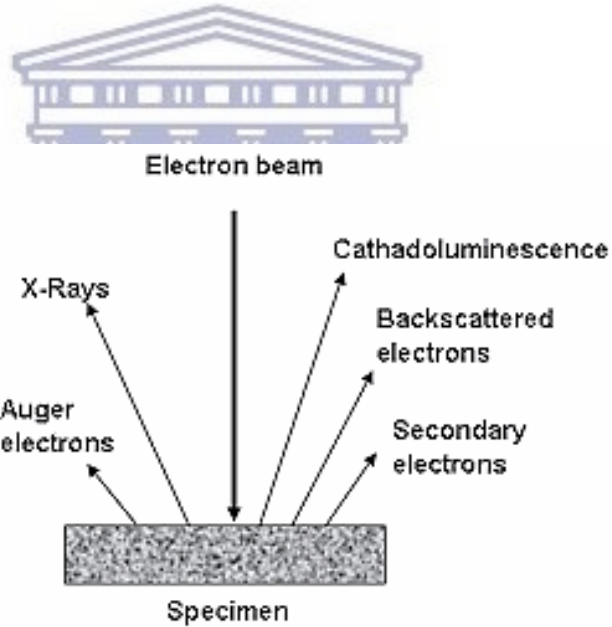


Figure 2. 3: Schematic representation of signals that may be used in SEM [2.7].

All these signals provide information about the specimen. The BE provide information about the atomic number contrast and topography contrast while SE gives information about the surface structure of the specimen. Cathodoluminescence gives electrical information, X-rays give chemical composition information about the surface while Auger electrons have low energy and are easily absorbed so they require an ultra-high vacuum system and specialised equipment for their efficient detection. In

explaining in-depth as to how these different signals shown in figure 2.3 are produced, we will need to define the term “interaction volume”. Interaction volume is the region within which electrons penetrate and scatter inside the specimen, see an illustration in figure 2.4. Even though these signals are generated within the interaction volume, they still however need to escape the specimen to be detected and that depends on the signal itself and the specimen.

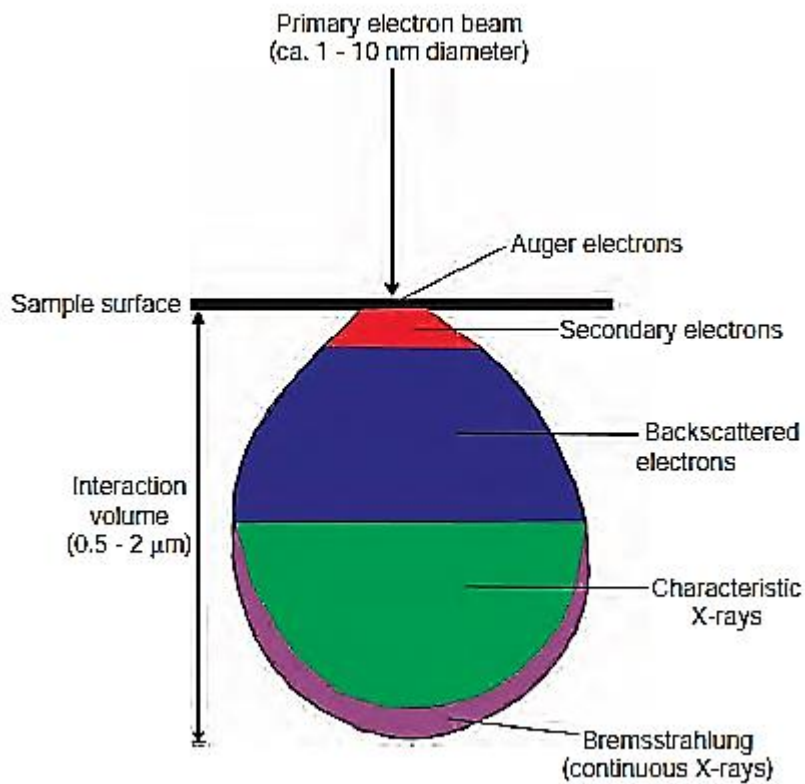


Figure 2. 4: The interaction volume between electron the beam and the specimen

[2.8]

As can be seen from figure 2.4, the X-ray signal is the large part of the interaction volume. This is because the electron beam has high energy as it reaches the specimen. This leads to deep penetration of electrons, and an ejection of the innermost electrons of the atoms of the specimen which both subsequently result in the generation of X-rays. The BE are produced when primary electrons are scattered from the nuclei of the atoms of the specimen due to the difference between the mass of the electron and the nucleus. Therefore the backscattered signal originates from a smaller region compared to X-rays as shown in figure 2.4. The SE are produced when primary electrons eject the outer most electrons of the atoms of the specimen with an energy less than 50 eV. Therefore the detected SE originate from the region which is little larger than the diameter of the incident beam, see figure 2.4 as well.

2.2.5 Detection of secondary and backscattered electrons

All SEMs have facilities for detection of SE and BE. The most commonly used electron signal for imaging in SEM is the SEs which is normally detected by a scintillator photomultiplier (PM) system known as an Everhart-Thornley detector [2.9]. When the SE escape from the specimen, they are collected by a Faraday grid surrounding the scintillator which has a bias voltage between 0 and 200 V. Apart from collecting the SE, the Faraday grid prevents the high voltage of the scintillator from affecting the incident electron beam as well. The SE first strike the aluminium covering the scintillator, and then get accelerated before reaching the scintillator because of its low energy (10-50 eV) to excite the scintillator. The scintillator detector then emits light which is transmitted through a light guide all the way to the PM tube which converts the photons into pulses of electrons, see figure 2.5.

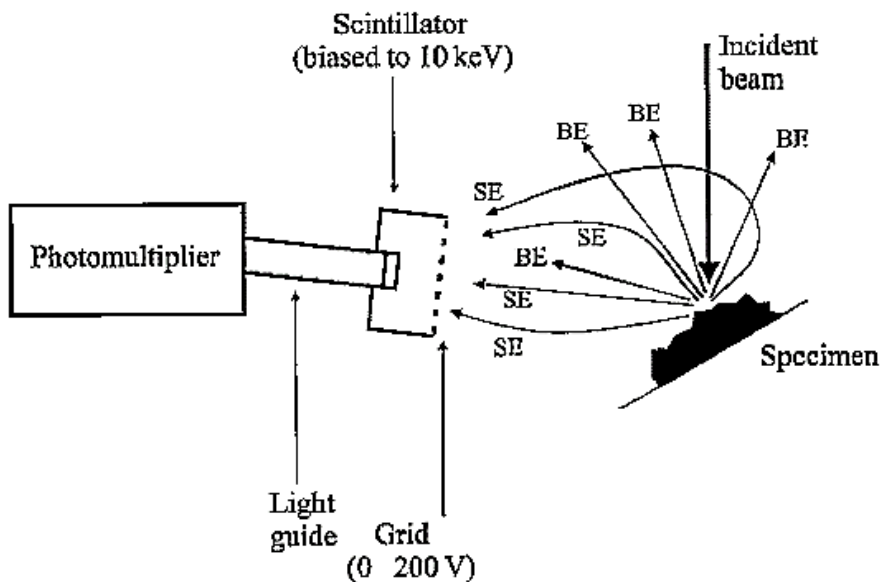


Figure 2. 5: Schematic representation of the secondary electrons detection [2.1].

The BE are detected by specialised BE detectors positioned above the sample and designed to maximize the solid angle. The widely used BE detectors include; the scintillator, solid angle, and through-the-lens detectors. Even though a fraction of BE that is directed toward the Everhart Thornely detector will be detected, it is not sufficient for the detection of BE because (i) only a few BE are travelling toward the SE detector and (ii) the biased detection grid has little ability to attract high energy BE.

2.2.6 Energy dispersive X-ray spectroscopy (EDS)

In SEM, when a specimen is struck with high energy particles like a beam of electrons, continuous and characteristic X-rays are produced. While the continuous X-rays are produced when any electrically charged particle of sufficient kinetic energy (KE) is rapidly decelerated, the origin of the characteristic X-rays lies in the atom of the target material [2.10]. To comprehend the phenomenon of characteristic X-rays, consider an atom as consisting of a central nucleus surrounded by electrons lying in various shells (K,L and M shells) as shown in figure 2.6 below. When an incident beam of electrons strikes a bound electron of an atom within the specimen, the struck electron is ejected from the inner shell (K shell) of the atom leaving a positively charged hole behind causing an atom to be in an excited high-energy state. Because atoms are more comfortable in a stable or relaxed state, this leads to an electron transition from the outer shell (e.g. L or M shell) to the K shell of the atom. This electron transition results in an emission of a photon (X-ray) with energy equivalent to the energy difference between the two shells. An electron transition from the L shell to the K shell produces a K_{α} X-ray, from the M shell to the K shell produces a K_{β} X-ray while from M to L shells produces L_{α} [2.10], as shown in figure 2.6. Each element has a unique set of energy levels (the gap between the shells), hence the transitions of an electron from the higher to the lower energy levels produce X-rays with energies that are characteristic to each element within the specimen.

UNIVERSITY of the
WESTERN CAPE

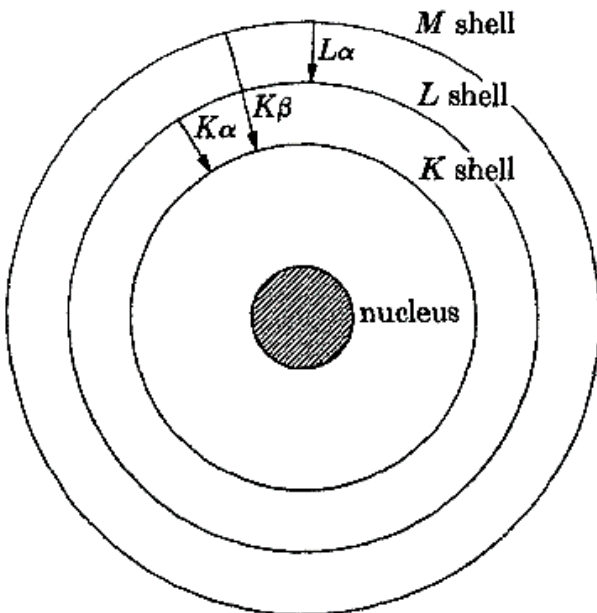


Figure 2. 6: Schematic representation of the generation of characteristic X-rays within an atom [2.10].

The number and the energy of X-rays emitted is measured by an energy dispersive spectrometer. This type of a detector consists of a semiconductor material, typically Si whose electrons are excited to a conduction band, leaving the equivalent number of positively charged holes in the outer shell upon the detection of incident X-rays. The number of electron-hole pairs generated determines the energy of the X-ray photon being detected which subsequently creates a charge pulse. This charge pulse is converted to a voltage pulse (which remains proportional to X-ray energy) by a charge sensitive preamplifier. The signal is then transmitted to a multichannel analyser (MCA) which separates pulses with respect to their voltage [2.11]. From the voltage measurements, the energy of each incident X-ray is determined and sent to the computer. The computer then displays the spectrum as a histogram of counts versus energy. Figure 2.7 shows the simulated X-ray spectrum as might be observed in a SEM. The sharp intensity maxima peaks, i.e. characteristic X-ray (solid lines) peaks are superimposed on a slowly varying background of continuous X-rays (dashed line) [2.11]. Since they are narrow and since their energies are characteristic of the target metal used, they are called characteristic lines which together form the characteristic X-ray spectrum of the sample.

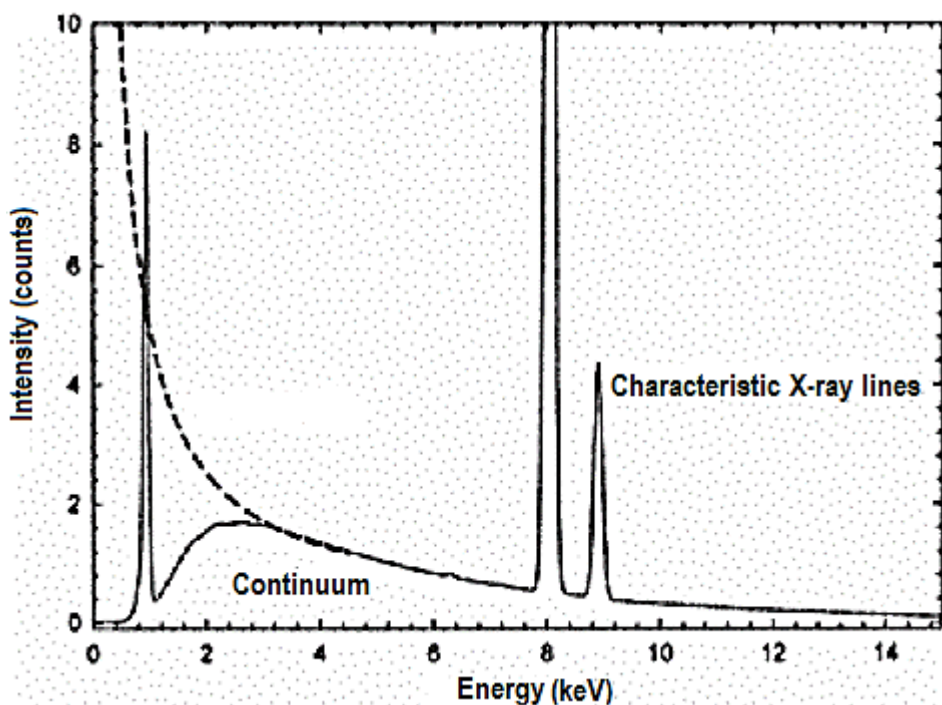


Figure 2. 7: Simulated EDS spectrum [2.11].

2.2.7 Sample preparation for SEM

In order for the sample to fit in the specimen chamber and to be mounted on the specimen stub it must be of appropriate size. The specimen must be clean, electrically conductive on the surface and electrically grounded in order to get good images without degradation. This is required so as to avoid electrons building up on the sample's surface during the electron beam-specimen interaction which could lead to the electron beam being deflected from its normal path. Obviously, already conductive sample need less attention when it comes to preparation. They only require to be cleaned and mounted correctly to ensure that they are grounded. However, non-conductive samples present a problem of electrons building up on the surface of the sample which is also known as charging. It is common to coat them with a thin layer of conductive material, normally Au or C which is efficiently done by sputter coating. Apart from conducting away electrons, the coating layer reduces thermal damage of the sample and enhances the BE and SE emission as well, thus leading to good results.

2.3 Transmission Electron Microscopy

2.3.1 Introduction

The Transmission Electron Microscope (TEM) is a device used in a range of scientific fields including physical, chemical and biological science to provide morphological, compositional and most importantly the crystallographic information of any given sample or specimen. The first TEM was developed by Max Knoll and Ernst Ruska for which Ruska was awarded a Nobel Prize in physics in 1986 [2.12, 2.13]. For the TEM technique, a beam of electrons is transmitted through the sample and the interaction of electrons as they transmit through the sample form an image. An image is magnified and focused onto an imaging device, typically a fluorescent screen. TEM is capable of imaging at significantly high resolutions due to the small wavelength of electrons and its high electron accelerating potential difference, 40-200 kV, or higher. This enables a microscopist to examine fine details to as small as a single column of atoms [2.12].

2.3.2 Basic operation

Most components found in a TEM are the same as those of the SEM. These components are assembled into a vertical microscope column of which the schematic presentation is depicted in figure 2.8. A TEM consists of an electron gun which acts as an illumination source situated at the top of the column. Below the electron gun are two condenser

apertures which demagnify the beam of electrons emitted by the gun and control its diameter and location as it reaches the specimen [2.14]. Since the specimen is electron transparent, additional apertures and lenses are required below the sample. These are; (i) objective and intermediate apertures, and (ii) diffraction, intermediate and projector lenses. The role of the apertures is to control the convergence angle of the transmitted electrons down the line toward the viewing screen. An objective lens forms the first intermediate image while the diffraction lens is responsible for the diffraction pattern. Intermediate and projector lenses are used to magnify the image produced by the objective lens until it is finally projected onto the fluorescent screen [2.15]. A charged coupled device (CCD) camera is used to capture the image [2.14].

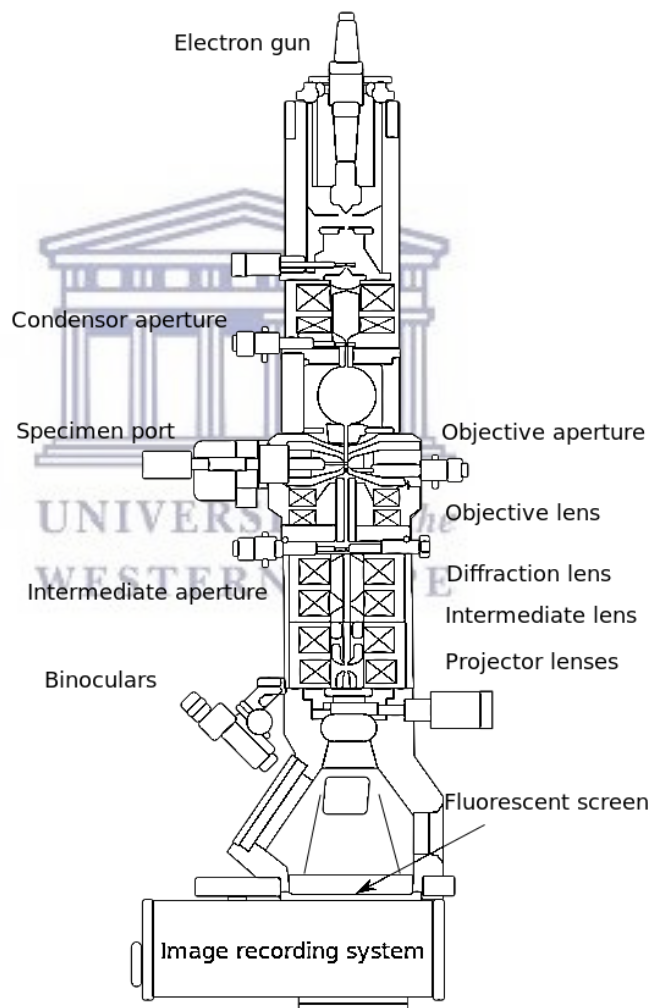


**Figure 2. 8: Schematic representation of a TEM and its important components
(JEM-1010, courtesy of JEOL Ltd.)**

2.3.3 Electron diffraction

Electron diffraction is a technique used to study matter (the sample) by bombarding them with an electron beam and analysing the resulting interference pattern. The two parameters of importance in electron diffraction are angular distribution of scattered electrons, and the intensity of scattering [2.16]. Electron diffraction yields essential information about crystal structures and their orientation. An understanding of factors that determine the intensity of scattered electrons provides an insight to more detailed information from a diffraction pattern and hence enables us to interpret the image of the crystalline material in a TEM with more clarity.

Consider an incident beam of electrons that are in phase with each other bombarding a crystalline specimen as shown in figure 2.9. Electrons interact with the atoms of the specimen, typically A and B as they pass through it. The scattered electrons (which can be considered as waves in this case) that are still in phase with each other will interfere constructively while those that are out of phase will interfere destructively resulting in a diffraction pattern on a viewing screen. The constructive interference at D occurs if the path length of the beam scattered by the atoms A and B differ by an integral number of wavelengths. This means that $CB + BE = n\lambda$, where $n = 1, 2, 3 \dots$, and λ is the electron wavelength. From simple trigonometry, it is apparent that $BE = CD = dsin\theta$, hence the condition for constructive interference is:

$$2dsin\theta = n\lambda. \quad (2.2)$$

This is known as Bragg's law and it tells us that very few elastically scattered electrons emerge from the specimen unless they are at an angle θ which is the solution to equation 2.2 [2.16]. This equation can be simplified to:

$$2d\theta = \lambda. \quad (2.3)$$

For electron diffraction it is conventional to consider only the first order of diffraction, i.e. $n = 1$ and deal with higher orders by using the corresponding multiples of Miller indices. Also, the wavelength of electrons is very short ($\lambda = 0.0037$ nm) and the interplanar spacing for most material is usually small, which results in a small diffraction angle where $sin\theta$ is approximately equal to θ . This makes electron diffraction much easier than XRD which works with larger angles.

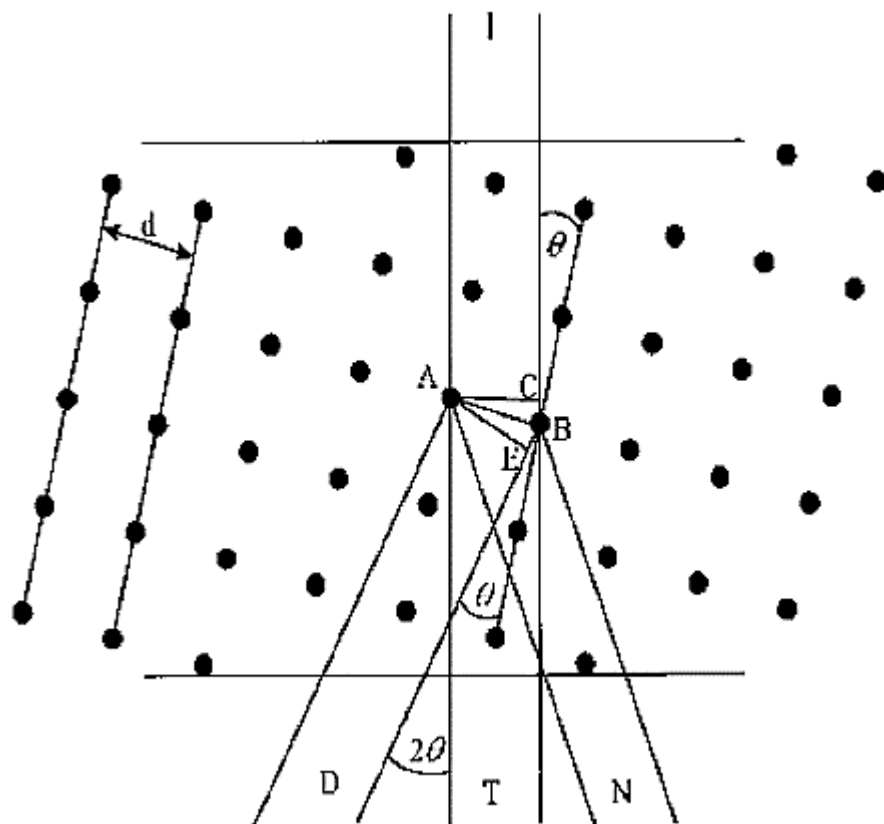


Figure 2. 9: The schematic representation of a cross section of a crystalline specimen bombarded by a beam of electrons (I). Electrons may emerge on the other side of the specimen having scattered (D and N) or unscattered (T) [2.16].

Using the Miller index notation for a cubic crystal with a lattice constant a , the interplanar spacing d with the indices (hkl) in equation 2.2 above can be calculated as follows:

$$d_{hkl} = \frac{a}{\sqrt{h^2+k^2+l^2}}. \quad (2.4)$$

In order to understand the geometry of electron diffraction and the behaviour of scattered and unscattered electrons emerging from the specimen much better let us consider a simple ray diagram as shown in figure 2.10. When a beam of electrons hit the specimen some electrons are unscattered which means they do not interact with the specimen and hit the screen situated a distance L from the specimen at O . Other electrons are scattered through an angle of 2θ by the atoms of the crystalline specimen and hit the screen at A , which is a distance r from O . Using simple geometry, it is apparent from the figure 2.10 that:

$$\tan 2\theta = \frac{r}{L}. \quad (2.5)$$

For small angles of diffraction, equation 2.5 can be simplified to:

$$2\theta = \frac{r}{L}. \quad (2.6)$$

Combining equation (2.3) and (2.6) we find:

$$rd = L\lambda, \quad (2.7)$$

where $L\lambda$ is called the camera constant which is independent of the specimen since both the electron wavelength and camera length L are constant. One can thus obtain the d spacing of a specimen given the camera constant of the instrument by simply measuring the distance between the scattered and unscattered electrons, r . It is important to point out that in reality there are lenses between the specimen and the fluorescent screen, so L is not a physical distance but notional distance which can be changed by the user.

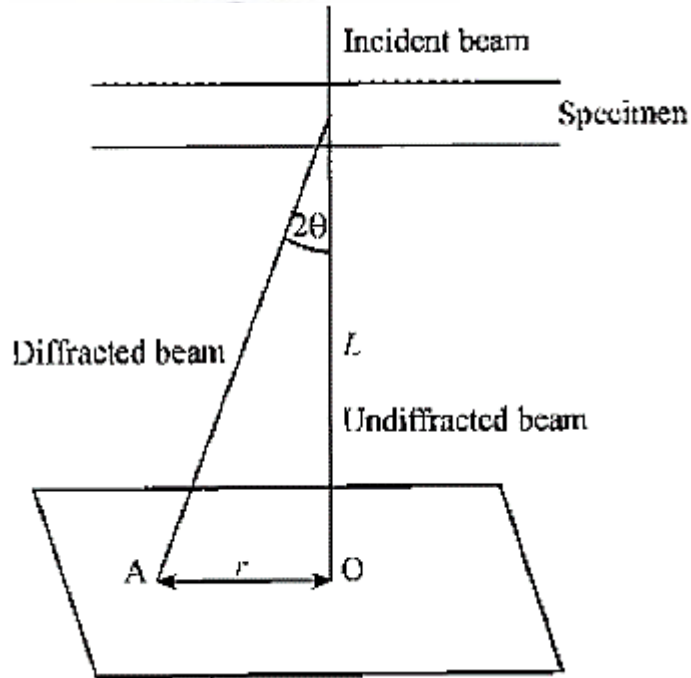


Figure 2. 10: Schematic diagram showing the geometry of diffraction pattern information [2.16].

2.3.4 The formation of a diffraction pattern.

Consider a parallel beam of electrons in a TEM from just above the specimen and down the column to the fluorescent screen shown in figure 2.11. Below the specimen there is an electromagnetic objective lens which collects all transmitted electrons scattered from one point of the specimen to one point on the screen causing an image of the sample to

be formed. Electrons diffracted in the same direction OA, A'O' come together to form a spot P. Analogously the diffraction spot Q is formed by electrons diffracted at an equal angle on the opposite side of the unscattered electron beam. This is the back focal plane of the microscope and is where the diffraction pattern is formed. By manipulating the magnetic lenses of a microscope, the diffraction pattern may be observed by projecting it onto the screen instead of an image.

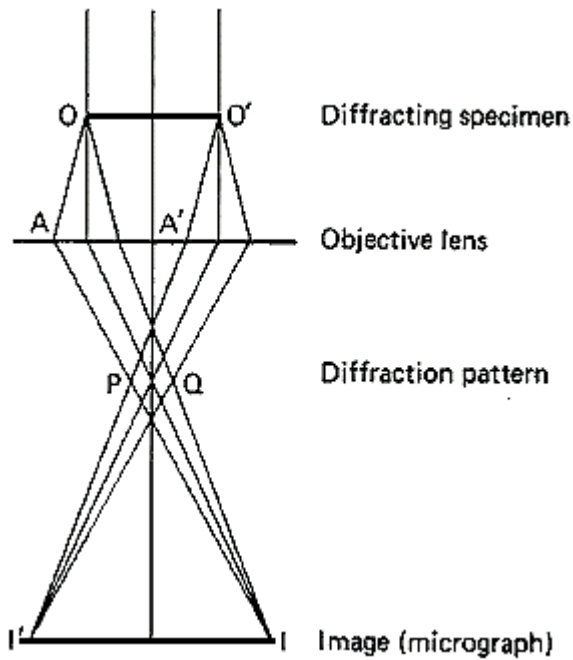


Figure 2. 11: The ray diagram of a projection microscope showing position of diffraction pattern and an image [2.6].

Different diffraction patterns arise from different materials of various microstructure, some of these diffraction patterns are shown in figure 2.12. It is important to note that not all planes of crystal structures present in a specimen will diffract the electron beam but only those planes that are lying parallel to the beam of the electrons will. A single crystal specimen whose planes are aligned with the incident beam of electrons will give rise to a diffraction pattern with a regular array of spots as depicted in figure 2.12 (a). Figure 2.12 (b) shows a specimen consisting of crystals with various crystal orientations, a diffraction pattern for this specimen is the sum of individual spot patterns and it begins to form circles. For a specimen containing a number of crystals with different crystal orientations (i.e. polycrystalline) a diffraction pattern with continuous rings of different radii will be observed, figure 2.12 (c).

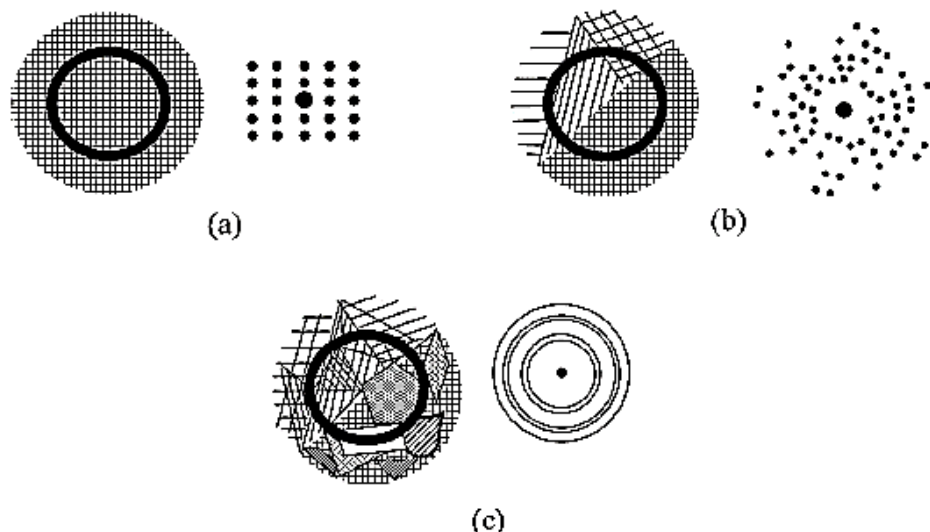


Figure 2. 12: Shows various types of diffraction patterns produced by specimens of different microstructure; (a) is a single perfect crystal, (b) consist small number of grain and (c) consist a large number of randomly oriented grains [2.16].

2.3.5 Sample preparation for TEM

For TEM analysis, attention needs to be paid to sample preparation. It is crucial to have a sample that provides sufficient essential information with minimum amount of interpretation required. There is a wide variety of preparation methods that are employed depending on the type of material being examined. Nonetheless, the important conditions that must be met by the sample for TEM investigations includes the following [2.6]:

- (i) The sample must be of appropriate size to fit in the specimen holder of the microscope.
- (ii) It must be thin enough ($\sim 10\text{-}1000\text{ nm}$) to allow sufficient transmission of electrons and yet retain the structure of the original sample at any level within the depth of field.
- (iii) It must be robust enough to handle electron bombardment in high vacuum.

The sample preparation method employed in this study will be discussed under experimental section of chapter 3 and 4.

2.4 Stylus Profilometry

2.4.1 Introduction

The Dektak 6M stylus profilometer is a stylus-based instrument that is used to measure thin film thickness and surface roughness. It is a contact measuring technique that drags a very low force (1-15 mg) diamond-tipped stylus across the surface of the sample [2.17]. The instrument was designed particularly for Si samples which inform that the samples should be planar. Nonetheless, depending upon the chosen stylus force, hard and soft materials can be profiled as well. The instrument is user friendly in the sense that it has a video camera which is used mainly for positioning the sample and tracing the stylus during the measurement process. In addition to that, the software allows useful profile manipulations like, profile levelling, zero referencing and magnification [2.17].

2.4.2 Working principle

Consider the schematic diagram of the Dektak 6M profilometer depicted in figure 2.13 below. The measurements of a moving sample underneath the stylus are taken electromechanically by a profiler. Here, a well calibrated stage moves together with the sample underneath the stylus based on the scanning parameters chosen [2.17]. As the stage moves the sample, the stylus which is mechanically connected to a linear variable differential transformer (LVDT) is translated in the vertical direction due to surface variation of the sample. Subsequently, the LVDT detects and produces electrical signals according to the stylus movement by comparing the alternating current (AC) reference signal proportional to the position of change. This analogue signal is then conditioned, converted to a digital format and stored in the computer memory for display, manipulation and printing.

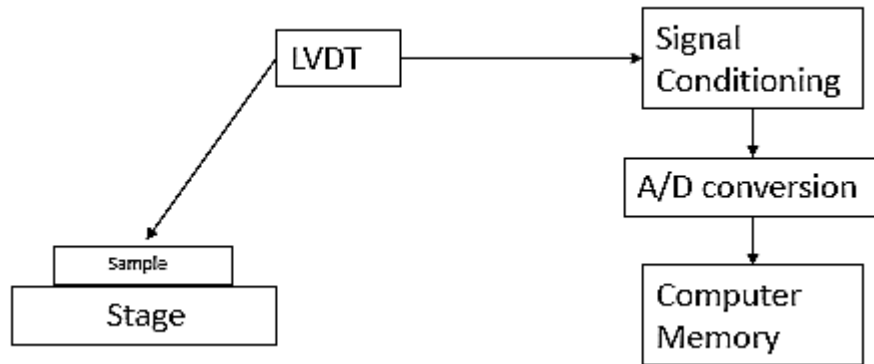


Figure 2. 13: Schematic representation of Dektak 6M architecture [2.17]

2.4.3 Horizontal scan resolution

A maximum of 30 000 points per scan can be achieved by the Dektak 6M profilometer [2.17] and a fixed number of 300 data points can be captured every second. This means that the scan length (5 μ m to 30 mm) and duration (3 to 100 seconds) dictates the horizontal resolution of the profilometer [2.17]. Therefore, increasing the scanning duration subsequently increases the number of data points processed which ensures enhanced resolution. Any thickness variation between 50 Å and 2620 kÅ can be detected by this instrument [2.17].

2.5 Hall Effect

2.5.1 Introduction

The Hall Effect which was first discovered by Edwin Hall in 1879 is the creation of a voltage difference across an electrical conductor that is transverse to an electric current in a conductor and a magnetic field perpendicular to the current [2.18]. The underlying principle of the Hall Effect is a Lorentz force, i.e. the force on a point charge due to an electromagnetic field [2.19]. Hall Effect measurements are used quite a lot in the electronic industry; from basic material research and development to device manufacturing. The Hall voltage (V_H) is the primary parameter that is obtained from the Hall Effect measurement system, other parameters like carrier mobility (μ), carrier concentration (n), Hall co-efficient (R_H), resistivity (ρ) and magnetoresistance are all derived from the Hall voltage. The I-V characterisation can be obtained from the Hall measurement system as well.

2.5.2 Theory

Consider a thin flat uniform conducting material with a width w and thickness d that contains n mobile charge carriers per unit volume orientated such that its flat surface is perpendicular to the uniform magnetic field \mathbf{B} as illustrated in fig 2.13. The electric current, given by the following equation is passed through the conductor, where q is the electric charge and v_d is the drift velocity of a moving charge carrier:

$$I = nqv_d wd . \quad (2.8)$$

Whether the current is a movement of holes or electrons in opposite directions, the magnetic force as a result of the magnetic field depletes the moving charge carriers toward the edges of the conductor perpendicular to both the magnetic field and direction of electric current flow [2.20]. The magnetic force acting on a given mobile charge since the charge moves perpendicular to the magnetic field is calculated by:

$$\mathbf{F}_B = qv_d \mathbf{B} . \quad (2.9)$$

The depletion of charge carriers results in electrons accumulating on one edge of the conductor perpendicular to current flow while holes accumulate on the other. This consequently creates an electric field opposing the magnetic force known as the Hall electric field (\mathbf{E}_H). When the magnetic force is equivalent to the electric force generated by the Hall electric field, an equilibrium state is reached:

$$\mathbf{F}_m = \mathbf{F}_e = qv_d \mathbf{B} = \frac{qV_H}{w}, \quad (2.10)$$

where V_H is the output voltage caused by the electric field of the accumulated charges. Using equation (2.8) and (2.10), V_H can be written in terms of the applied current and the magnetic field as:

$$V_H = \frac{IB}{nqd}. \quad (2.11)$$

The value of the Hall voltage is directly proportional to the current flowing through the conductor and magnetic field strength, and inversely proportional to the number of charge carriers and thickness of the conducting material.

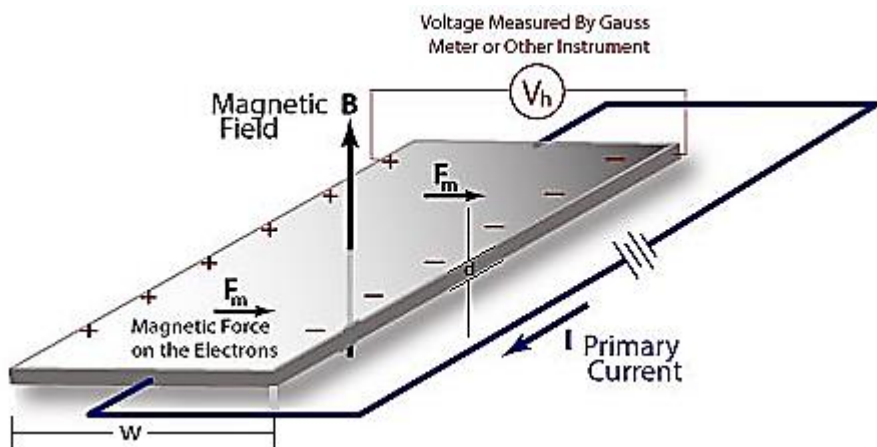


Figure 2. 14: The schematic representation of Hall Effect theoretical model [2.21]

2.6 Ultraviolet – Visible Spectroscopy

2.6.1 Introduction

Ultraviolet-visible (UV-Vis) spectroscopy is a material analysing technique that uses photons in the (i) near infrared, (ii) visible and (iii) near ultraviolet regions to measure the absorbance or the transmittance of molecules of the material. It is used for quantitative determination of different analytes, such as transition metal ions, highly conjugated organic compounds and biological macro molecules [2.22]. Spectroscopy analysis is commonly carried out in solution; however we will focus mostly on thin film absorbance analysis in this study. Different molecules absorb radiation of different wavelengths; hence an absorption spectrum shows a number of absorption bands corresponding to structural groups within the material. UV-Vis results are normally supported with fluorescence spectroscopy which deals with the transition from the excited state to the ground state, while absorption measures the transition from the ground to the excited state [2.22].

A spectrophotometer is pertinent to UV-Vis spectroscopy. It can be either a single or double beam instrument which consist of; (i) a light source, (ii) a monochromator, (iii) sample holder and (iv) a detector. The light source is often a tungsten filament which is continuous from 300 to 2500 nm, a deuterium arc lamp (190-400 nm), xenon arc lamp (160-2000 nm), or more recently LED [2.22]. The light produced from these light sources has a wide range of wavelengths so a monochromator is an optical tool which is used to select a narrow range of light wavelength. The detector is typically a PM tube, a

photodiode array or CCD and it is used to collect light of different wavelength from different pixels or groups of pixels at the same time.

2.6.2 Theory

When a certain material is irradiated with photons in UV-Vis (200-800 nm) region, it absorbs a certain percentage of photons while the rest is transmitted through the film. The absorbed radiation causes electronic transitions in the atoms or molecules of the material from the ground state to the excited state. The energy of UV-Vis radiation that is absorbed is equal to the energy difference between these two states. The ratio of radiation transmitted through the film of thickness t (I_t) to that transmitted through a reference (I_0) is referred to as transmittance (T) of the film and is given by:

$$T = \frac{I_t}{I_0}. \quad (2.12)$$

Transmittance has no units since it is a percentage and this is used to obtain the absorbance (A) of the film by the following equation:

$$A = \ln\left(\frac{I_0}{I_t}\right) = \ln\left(\frac{1}{T}\right). \quad (2.13)$$

UV-Vis spectroscopy obeys the Beer- Lambert law which states that, when a beam of monochromatic light passes through a thin film of an absorbing substance, the rate of decrease of intensity of radiation with thickness of the absorbing film is proportional to the incident radiation as well as the concentration of the of the material [2.23]. The mathematical expression of Beer- Lambert law is given by:

$$A = \varepsilon cl, \quad (2.14)$$

where ε is the molar absorptivity, c is the molar concentration and l is the length of the sample cell. From equation 2.14 it is clear that the photon absorption of the film depends on the number of molecules suitable for absorbing photons of given wavelengths.

2.6.3 UV-Vis mechanism

The absorption of UV-Vis radiation corresponds to the excitation of the outer most electrons. Different energy absorptions are possible based on the nature of the bond of molecules within the material. However, the most favoured transition is from the HOMO to the LUMO. In most molecules, usually the lowest occupied energy orbital is the σ bonding orbital. The π bonding orbitals are at intermediate occupied energy level while a non-bonding orbitals lie at higher energy levels. When energy is absorbed by

the molecule, electrons can be excited from bonding to antibonding states, this is depicted in figure 2.15.

For the $\sigma \rightarrow \sigma^*$ transition, an electron from the σ bonding orbital is excited to the σ^* antibonding orbital. The energy required for this transition is large, therefore the absorption maxima due to this specific transition are not observed in the typical UV-Vis spectra (200-800 nm). In saturated compounds containing atoms with lone pairs, non-bonding electrons are capable of $n \rightarrow \sigma^*$ transitions. Normally, these require less energy than $\sigma \rightarrow \sigma^*$ transitions and it is important to note that only few organic functional groups have $n \rightarrow \sigma^*$ peaks. Absorption spectroscopy of organic compounds is based mostly on $n \rightarrow \pi^*$ or $\pi \rightarrow \pi^*$ transitions. These absorptions occur in the UV-Vis region due to the presence of unsaturated groups in the molecule called chromophores. Chromophore is defined as any isolated covalently bonded group that shows a characteristic absorption in the UV-Vis region. Some typical chromophores are listed in Table 2.2 [2.22].

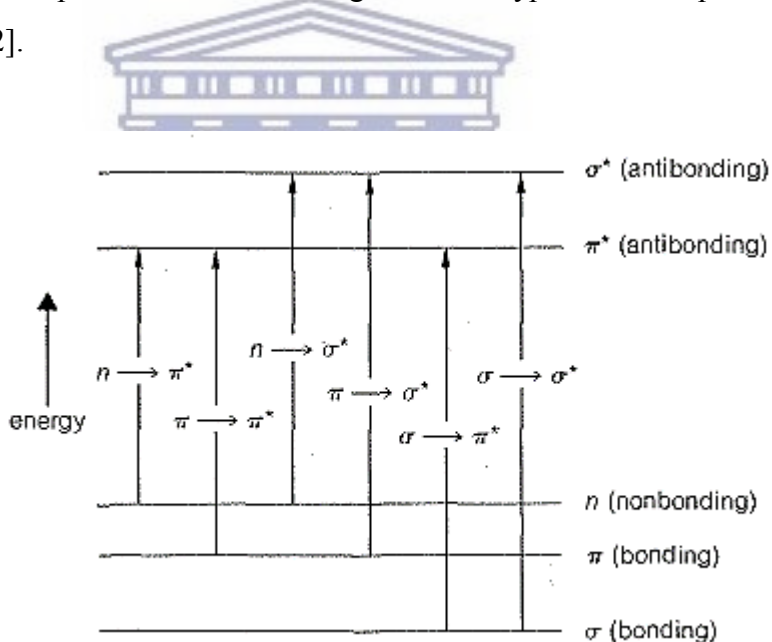


Figure 2. 15: Various possible transitions between the bonding and anti-bonding electronic states of a molecule [2.24].

Table 2. 2: Typical chromophores

Chromophore	Typical Compound	Electronic transition	Wavelength (nm)
>C=C<	Ethene	$\pi \rightarrow \pi^*$	180
>C=O	Propanone	$\pi \rightarrow \pi^*$	185
		$n \rightarrow \pi^*$	277
	Benzene	$\pi \rightarrow \pi^*$	200
-N=N-	Azomethane	$n \rightarrow \pi^*$	347
-N=O-	Nitrosobutane	$n \rightarrow \pi^*$	665

2.6.4 Experimental set-up

The UV-Vis set-up available at the Department of Physics and Astronomy (UWC) is shown in figure 2.16 below. In this set-up, the sample in the cuvette holder is irradiated with the beam of light that is continuous over the wavelength of 190-1200 nm produced by deuterium and tungsten light sources. Some of the incoming light is absorbed by the sample while the transmitted light is sent to the spectrometer. The spectrometer senses the light being transmitted through the sample and converts this information into digital signal for display on the computer monitor. The absorbance of the sample can be obtained by using equation 2.13.

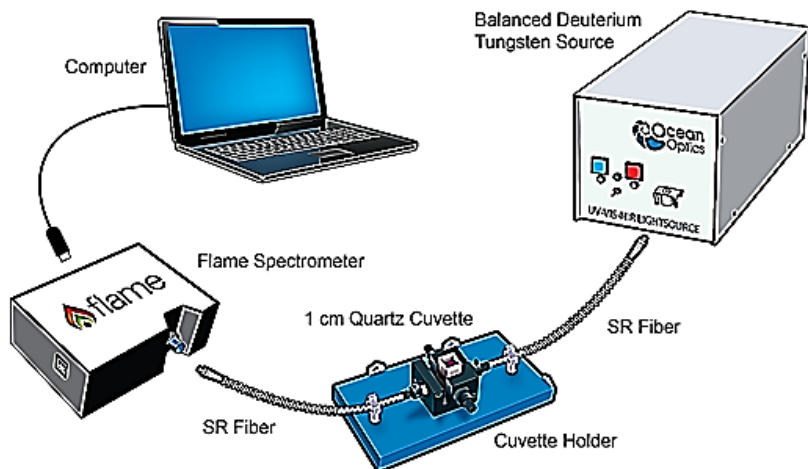


Figure 2. 16: Simplified Schematic of a double beam UV-Vis spectrophotometer [2.25].

2.7 Photoluminescence

2.7.1 Introduction

Photoluminescence (PL) is the light emission from any form of matter after an absorption of photons. It is one of many forms of luminescence and is initiated by photoexcitation [2.26]. After photon excitation, different relaxation processes take place in which other photons are re-emitted including fluorescence and phosphorescence. The time period between absorption and emission may vary, ranging from short femtoseconds-regimes for emission involving free carriers in organic semiconductors [2.27], up to milliseconds for phosphorescent processes in molecular systems. In some special cases, decay of photon emission may even last for several minutes or hours. This technique is used to investigate the energy and impurity levels of the material, hence providing optical and fundamental electronic properties about the material.

2.7.2 Theory

Let us consider what happens to a molecule after it has absorbed a photon. Assume that electrons of a molecule initially occupy the lowest vibrational energy level, a singlet state labelled S_0 in figure 2.17. From the figure it can be observed that the absorption of photons rapidly excites (10^{-15} s) the molecule to one of several vibrational energy levels in the first excited (S_1) or the second excited state (S_2), which are both in singlet states. Then, the excited states decay rapidly by vibrational relaxation (10^{-10} s) which is a radiationless decay. Internal conversion (ic) is another radiationless deactivation that

occurs when a molecule in the lower vibrational energy level of an excited state passes directly into a higher vibrational energy level of lower state. Due to these radiationless decays, a molecule in an excited state may return to the ground state without emitting a photon.

Fluorescence occurs when a molecule in a lowest vibrational energy level of an excited state decays to a lower electronic state by emitting a photon. In this case, photons having a longer wavelength than the exciting photon are emitted only after 10^{-8} - 10^{-6} s [2.28]. This is caused by a non-radiative transfer of energy from the excited species to other molecules, i.e. external conversion (ec), e.g. collision of excited species with gas molecules, such as O₂ [2.28]. During these excitation and decay processes the orientation of the electron spin is preserved. Sometimes triplet states can be generated from ordinary singlet states by intersystem crossing (isc). An isc occurs when a molecule in a lower vibrational energy level of a higher electronic state passes to a higher vibrational energy level of a lower electronic state with a different spin state. An example of isc is shown in figure 2.17 between a singlet excited state S₁ and a triplet state T₁. A molecule in the T₁ state decays after isc by vibrational relaxation or in some cases by phosphorescence, a slow photon radiation process ($T_1 \rightarrow S_0 + h\nu$) which takes 10^{-4} - 10 s or even longer. Phosphorescence is usually observed only if ec is reduced by cooling or immobilization. The wavelengths of phosphorescence are even longer than that of fluorescence, as depicted in figure 2.17.

The intensive fluorescence peak is found in aromatic compounds with low energy transitions, i.e. $\pi \rightarrow \pi^*$ while $n \rightarrow \pi^*$ transitions show weak fluorescence. On the other hand, phosphorescence is most favourable for molecules with $n \rightarrow \pi^*$ transitions, which have a higher probability for an isc than a $\pi \rightarrow \pi^*$ transition. For example, phosphorescence is observed with aromatic molecules containing carbonyl groups or heteroatoms. Aromatic compounds containing halide atoms have high efficiency for phosphorescence. In general an increase in phosphorescence corresponds to a decrease in fluorescence.

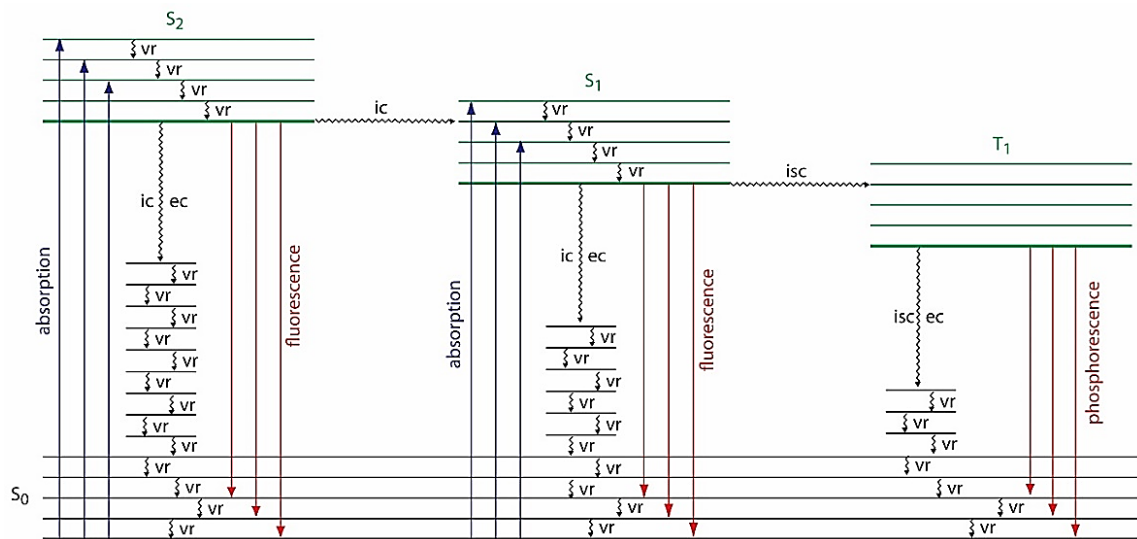


Figure 2. 17: Energy diagram showing absorption of light and the processes involved in the emission of light as fluorescence and phosphorescence [2.29].

2.7.3 Experimental set-up

Consider the basic components of the spectrofluorometer (i.e. sources, excitation monochromator, sample-compartment module, emission spectrometer, detector, SpectrAcq (controller) and the computer) as shown in figure 2.18 below [2.30]. The main component of the system is the SpectrAcq controller. This is a key component of the system because it is used to transfer the information from and to the computer. In addition, it controls components like the monochromator, compartment module and the spectrometer. A source of radiation produces photons that are reflected and focused to the excitation monochromator. In the monochromator, the beam of light is filtered to allow a single wavelength of light to reach the sample compartment. In the sample compartment, the incoming monochromatic light interacts with the sample. In fact, the sample absorbs the incoming radiation and then re-radiates it to the emission spectrometer. The emission spectrometer filters the emitted radiation from the sample and sends the signal to an InGaAs (Indium Gallium Arsenide) array detector. By stepping the monochromator or spectrometer or both through a wavelength region, and recording the variation in the intensity as a function of wavelength, a spectrum is produced on the screen of the computer [2.30].

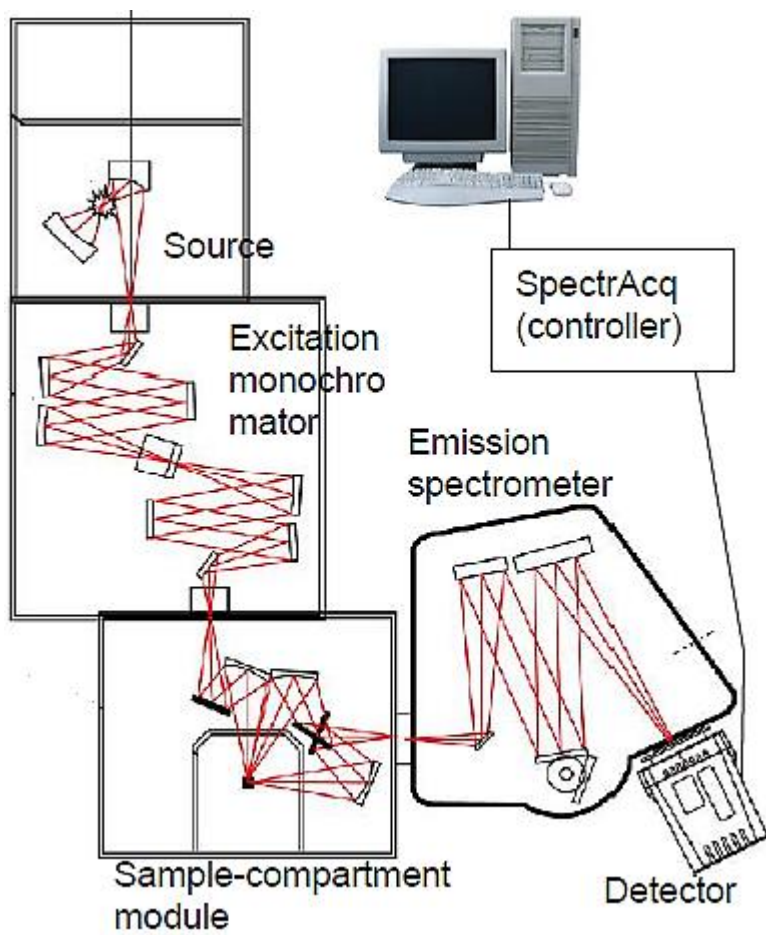


Figure 2. 18: Schematic diagram of the NanoLog spectrofluorometer showing the main features of the system [2.30].

UNIVERSITY of the
WESTERN CAPE

References

- [2.1] Goodhew, P.J., Hampshire, J. and Beanland, R. (2001). The Scanning Electron Microscopy, *Electron microscopy and analysis*. 3rd ed. London and New York :Taylor and Francis, pp 122-168.
- [2.2] Wischnitzer, S. (1989). The Electron Microscope, *Introduction to electron microscopy*. 2nd ed. New York: Pergamon Press, pp 38-108.
- [2.3] Lyman, C. (1990). Basic SEM imaging, *Scanning electron microscopy, X-ray microanalysis, and analytical electron microscopy*.New York: Plenum Press, pp 3-7.
- [2.4] Wischnitzer, S. (1989). Basic Theory of Electron Microscopy, Introduction to electron microscopy. 2nd ed. New York: Pergamon Press, pp 6-37.
- [2.5] Goodhew, P.J., Hampshire, J. and Beanland, R. (2001).Microscopy with light and electrons, *Electron microscopy and analysis*. 3rd ed. London and New York :Taylor and Francis, pp 1-19.
- [2.6] Watt I., (1997). The electron microscope family, *The Principle and Practice of Electron Microscopy*. 2nd ed. Great Britain : Cambridge University Press, pp 59-135.
- [2.7] Hafner B., (2015). *Scanning Electron Microscopy Primer*, Characterization Facility: University of Minnesota-Twin Cities.
- [2.8] Fahlman, B. (2007). Materials characterization, *Materials chemistry*. The Netherlands: Springer, pp 357-418.
- [2.9] Lyman, C. (1990). Backscattered Electron Imaging, *Scanning electron microscopy, X-ray microanalysis, and analytical electron microscopy*. New York: Plenum Press, pp 51-54.
- [2.10] Cullity, B. (1956). Properties of X-rays, *Elements of X-ray diffraction*. Addison-Wesley Publishing Company. Inc, pp 1-25.
- [2.11] Garratt-Reed, A. and Bell, D. (2003). Principles, *Energy-dispersive X-ray analysis in the electron microscope*. Oxford: BIOS, pp 5-17.
- [2.12] Williams D. and Carter C. (2009). *Transmission Electron Microscopy: A Textbook for Materials Science*. 2nd ed. New York: Springer Science & Business Media, pp 3-22.
- [2.13] Rose H H 2008 *Science and Technology of Advanced Material* **9** 30.
- [2.14] Goodhew, P.J., Hampshire, J. and Beanland, R. (2001). The transmission electron microscopy, *Electron microscopy and analysis*. 3rd ed. London and New

- York :Taylor and Francis, pp 66-121.
- [2.15] Reimer, L. and Kohl, H. (2010).The Transmission Electron Microscope, *Transmission electron microscopy*. New York, NY: Springer, pp 57-88.
- [2.16] Goodhew, P.J., Humphreys, J. and Beanland, R. (2001). Electron diffraction, *Electron microscopy and analysis*. 3rd ed. London and New York :Taylor and Francis, pp 40-65.
- [2.17] Dektak 6M manual (2002), *Overview of the system*, Digital Instruments Veeco Metrology Group, pp 3-18.
- [2.18] Hall E H 1879 *American Journal of Mathematics* **2** 287
- [2.19] Ramsden E (2006) Hall-Effect Physics, *Hall-effect sensor: Theory and Application*. 2nd ed. Oxford: Elsevier Inc, pp 1-9.
- [2.20] Ebrahimi F (2016) Finite –Element Modelling and Analysis of Hall Effect and Extraordinary Magnetoresistance Effect: *Finite Element Analysis New trends and Development*. 2nd ed. ExLi4EvA, pp 201-224.
- [2.21] Josh's Hall Effect Cache (2017). [Online]. Available at: <https://sites.google.com/site/joshshalleffectcache/> (Accessed on 03 October 2017).
- [2.22] Thomas, M.J.K. and Ando, D.J. (1996). *Ultraviolet and Visible Spectroscopy*. 2nd ed. Chichester, England :Wiley & Sons.
- [2.23] Griner, H.C. and Threlfall T.L. (1992). Principles, *UV-Vis spectroscopy and its applications*. Berlin Heidelberg: Springer-Verlag, pp 3-9.
- [2.24] Roberts J.D. and Caserio M.C. Separation and purification. Identification of organic compounds by spectroscopic techniques, Basic principles of organic chemistry.2nd ed. Menlo Park, California: W.A. Benjamin. Inc, pp 257-340.
- [2.25] Ocean Optics (2018), Absorbance. [Online] Available at <https://oceanoptics.com/measurementtechnique> (Accessed 19 June 2018)
- [2.26] McNaught, A.D. and Wilkinson, A. (1997), Compendium of Chemical Technology, International Union of Pure and Applied chemistry (IUPAC), 2nd ed . Online corrected version.
- [2.27] Hayes G R and Deveaud B 2002 *Physica Status Solidi* **190** 637
- [2.28] Kellner, R., Mernet, J.M., Otto, M. and Widmer, H.M. (1998). UV-Vis Spectroscopy, Emission and Luminescence, *Analytical Chemistry*. Federal Republic of Germany: WILEY-VCH Verlag GmnH, pp 527-539.
- [2.29] Chem.libretext.org. *Photoluminescence Spectroscopy*. (2016).

[Online].Available at:

[http://chem.libretexts.org/Textbook_Maps/Analytical_Chemistry_Textbook_Maps/Map:_Analytical_Chemistry_2.0_\(Harvey\)/10_Spectroscopic_Methods/10.6:_Photoluminescence_Spectroscopy](http://chem.libretexts.org/Textbook_Maps/Analytical_Chemistry_Textbook_Maps/Map:_Analytical_Chemistry_2.0_(Harvey)/10_Spectroscopic_Methods/10.6:_Photoluminescence_Spectroscopy) (Accessed on 18 August 2016)

[2.30] HORIBA Instruments Incorporated (2012), System Description, *NanoLog Spectrofluorometer-System Operation Manual*. NanoLog rev.C J81096



3 METAL ASSISTED CHEMICAL ETCHING OF SILICON WAFER FOR THE FORMATION OF SILICON NANOWIRES

3.1 Introduction

Si is an extremely important semiconducting material in microelectronics. Si nanostructures in particular have received tremendous attention over the past decades due to their potential for nano devices fabrications. MACE of semiconductors is fundamentally a wet and directional etching technique which was described by Li and Bohn after the first publication of MACE of Si was reported by Malinovska et.al.in 1997 [3.1, 3.2]. Nanostructures synthesised using this method have demonstrated their potential applications in a variety of fields including solar energy conversion, thermal power conversion, energy storage as well as sensors due to the following reasons [3.1]. To begin with, MACE is a simple and cost-efficient Si nanostructure synthesis method which enables scientists to control the size of grown nanostructures like the diameter, length, cross-section etc. Another remarkable feature of MACE is the fact that it enables control of the orientation of Si nanostructures relative to the substrate.

MACE synthesis of SiNWs can be divided into two steps. The first step involves electroless deposition of a noble metal like Ag. There are different methods with which metal deposition can be done i.e., spin or spray coating, thermal evaporation or sputtering of thin films, charged beam deposition from reactive precursors, electroless

deposition, etc. [3.2]. The latter has gained considerable interest because of its simplicity and is often employed when there is no precise morphology requirement of the resulting silver nanoparticle (AgNP) film. Figure 3.1 (a) shows the deposition of AgNPs from HF, silver nitrate (AgNO_3) and deionised (DI) water (H_2O) solution onto a Si wafer [3.3, 3.4]. During the deposition of Ag, a cathodic electrochemical reaction occurs on the Si surface and the oxidation of the Si wafer underneath AgNPs begins [3.5]. The second step of MACE of Si includes immersion of the AgNP-coated Si wafer into the HF/ H_2O_2 / H_2O etching solution, wherein oxidation of the Si wafer underneath the AgNPs is enhanced and etched away by HF [3.5]. During the etching process, pits are formed immediately underneath the AgNPs, and this result in AgNPs sinking toward the base of the Si wafer. The areas which were uncovered by the AgNPs remain unetched and results in the formation of SiNWs, see figure 3.1 (b), (c) and (d).

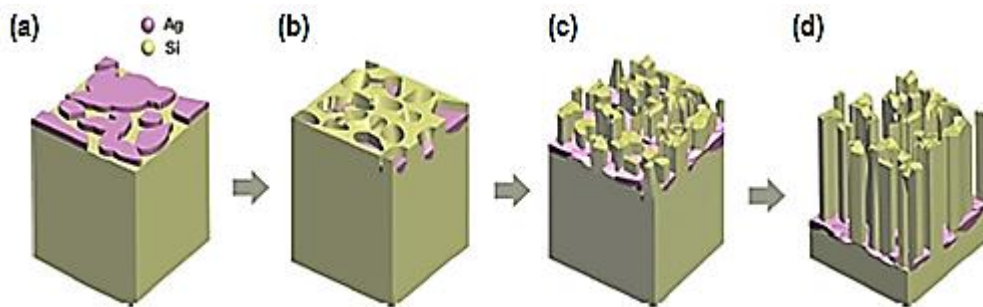


Figure 3. 1: Schematic illustration of MACE of Si for the realisation of SiNWs
[3.6].

3.2 MACE mechanism

3.2.1 Formation of silver nanoparticles

The formation mechanism of SiNW arrays through MACE involves an oxidation and etching of the Si substrate using the metal nanoparticles (NPs) as a catalyst, H_2O_2 as an oxidant and HF as the etching components [3.7]. Consider as in figure 3.2(a) below, when a Si substrate is immersed into the HF/ AgNO_3 solution it is coated by silver ions (Ag^+). The Ag^+ get deposited onto the Si substrate in the form of metallic silver nuclei by capturing electrons from Si-Si bonds [3.8]. The Ag nuclei deposited on the Si substrate have higher electronic activity than the Si atoms, hence the latter constantly supply electrons for Ag^+ reduction which subsequently results in the formation of AgNPs nucleates. Simultaneously, the Si substrate underneath the AgNPs begins to be oxidized due to O from H_2O molecules as an oxidant, see figure 3.2 (b). On these

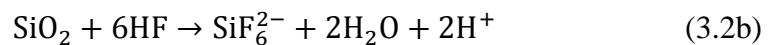
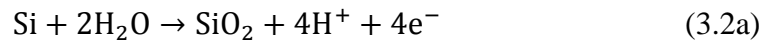
locations the Si substrate is oxidized to silicon dioxide (SiO_2) which is subsequently etched into the etching solution by HF in the form of SiF_6^{2-} , leading to AgNPs sinking down into the substrate, as depicted in figure 3.2 (c).

The chemical reactions can be outlined by the two half-cell reactions as follows [3.7, 3.8]:

Cathode reaction:



Anode reaction:



The overall reaction can then be described by:

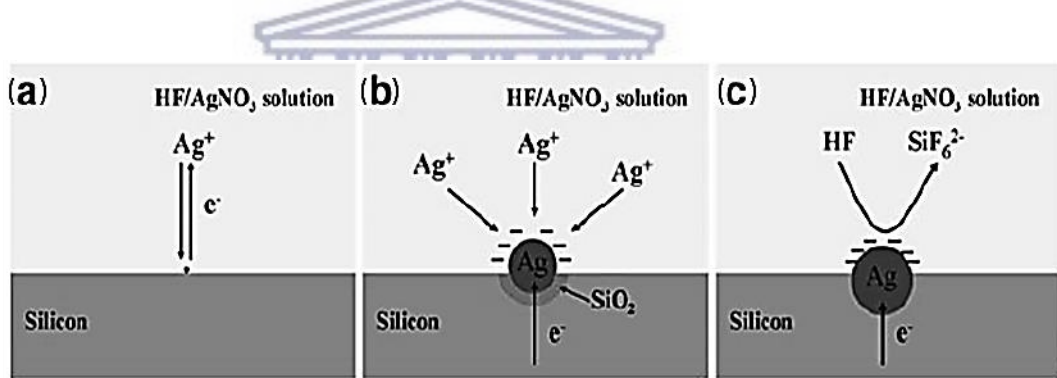


Figure 3. 2: Mechanism diagram of electroless Ag deposition on the Si substrate in HF/AgNO_3 solution, (a) Formation of Ag nucleation, (b) Ag particles growth and Si oxidation and (c) Ag particle trapped in the pit created by the dissolution of SiO_2 [3.7].

Ag nucleation and growth which occurs immediately upon the Si wafer immersion into an electroless solution containing Ag^+ was shown to be a complex, dynamic process. It allows Ag to dissolve, redeposit and/or migrate to more energetically favoured locations [3.9]. Using surface energy arguments, a large distribution of small Ag particles is formed and quickly combines with one another into larger lumped NPs through dynamic redistribution of Ag as depicted in figure 3.3. Here a negatively charged Ag nucleus due to the attraction of electrons from the Si donates electrons to

other Ag nuclei at the surface of the Si wafer [3.10]. This transfer of electrons reduces the attraction of incoming Ag^+ on the location where the electron moved from and increases the electron attraction on the location where the electron moved to. The reduction leads to Ag nuclei increasing in size while the oxidation leads to Ag nuclei reducing in size up until they combine with the bigger nuclei. Therefore, free Ag exchange between NPs is possible. This can lead to the formation of dendrite structures of deposited Ag when a Si substrate is immersed in a solution containing HF and Ag^+ for a relatively long time [3.1].

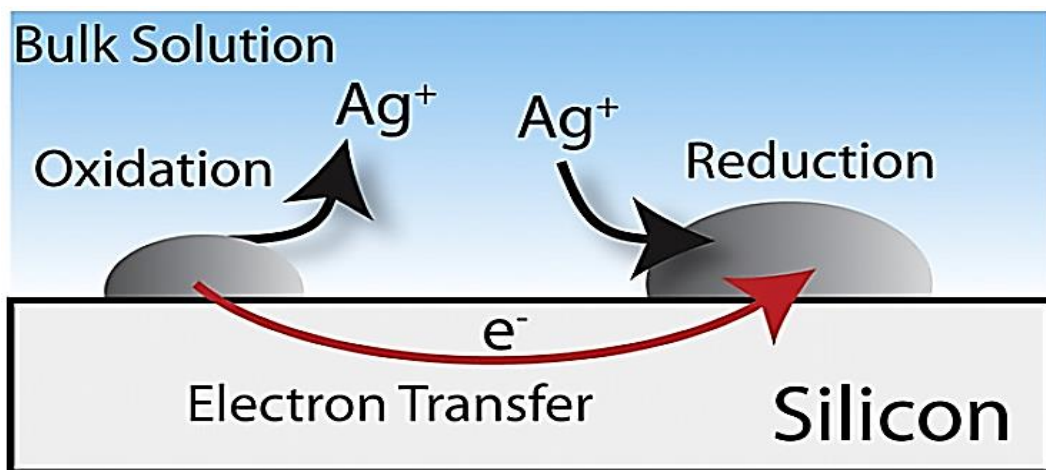


Figure 3. 3: This diagram represent the dynamic electrochemical redistribution of Ag between nanoparticles [3.9].

It has been proposed that nucleation occurs preferentially at the surface defect caused by dopants of Si, hence AgNPs density on the Si wafer increases with doping concentration [3.11]. Zachary et al. showed the progressive growth of deposited AgNPs on a p-type (100) Si wafer [3.9], see figure 3.4. It was observed that the quantity of AgNPs per unit area and the shape of these NPs depended strongly on the immersion time. During initial nucleation, the NPs are isolated on the Si substrate and grow independently in 3 dimensions (3-D), see figure 3.4 (a). As the immersion time of the Ag coated Si substrate is increased, the 3 dimensional individual growth of NPs decreased and the growth of NPs diameters is then attributed to the combination of small NPs into large NPs which ultimately resulted in an essential increase of uncovered surface of the substrate, as depicted in figure 3.4 (b) and (c). Further prolonging of immersion duration results in a rapid increase of NP diameters with little to no increase of the uncovered surface of the Si substrate, see figure 3.4 (d).

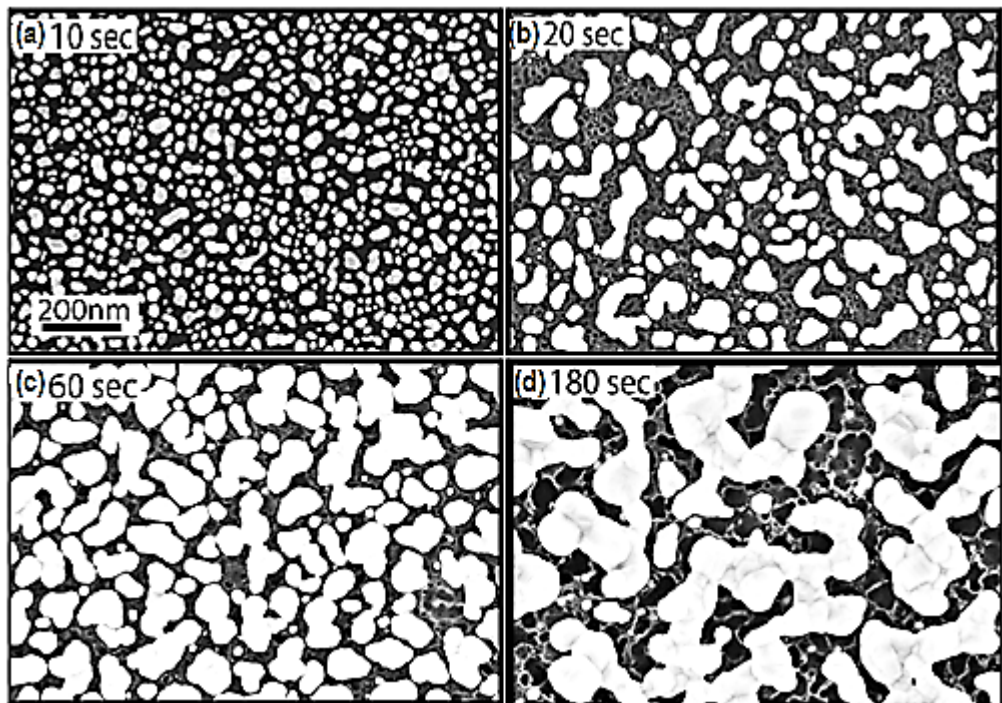
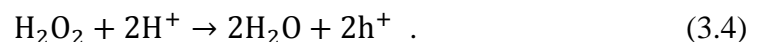


Figure 3. 4: The dependence of deposited AgNPs distribution and shapes with time on a p (100) Si substrate, as shown by Zachary et.al [3.9].

3.2.2 Formation of SiNWs

When the AgNP-coated Si wafer is immersed in a bath containing HF and an oxidiser such as H_2O_2 , the oxidation of Si underneath the AgNPs continues and the dissolution of the oxidised Si occurs analogously, as illustrated in figure 3.5 (a) [3.12]. During this process H_2O_2 acts as a hole (h^+) donor and oxidant while HF is used to dissolve the oxidised Si. With Si underneath the AgNPs constantly oxidised and dissolved, this leads to further sinking of the AgNPs which subsequently results in SiNW formation as shown in figure 3.5 (b) and (c) [3.6]. During the formation of SiNWs the AgNPs deposited on the Si wafer enhance the etching rate by catalysing the H_2O_2 reduction [3.13]. The chemistry of Si dissolution reactions in the presence of H_2O_2 and HF involve cathodic and anodic reactions. The side of the AgNPs facing the etching solution act as cathode sites while the side facing the Si act as anode sites. These chemical reactions can be written as follows [3.14]:

Cathode reaction (at metal):



The anode reaction of the Si interface can be written as:



while the overall reaction becomes:

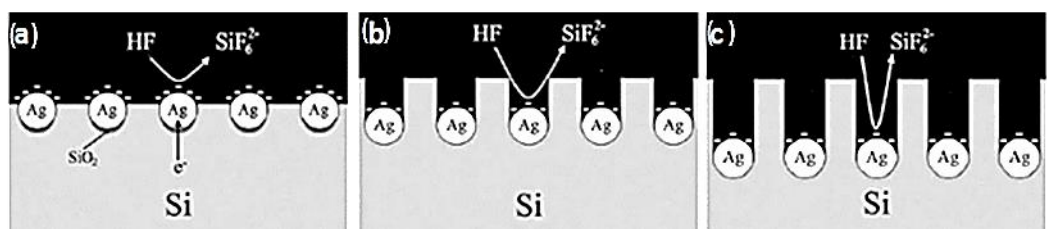
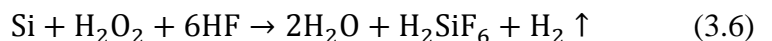


Figure 3. 5: Mechanism of Ag nanoparticle- assisted chemical etching of silicon which lead to the formation of SiNWs [3.8].

In response to the limited application of vertically aligned SiNWs researchers have developed methods to detach these SiNWs from a bulk Si wafer and transfer them onto another substrate. One method of detaching SiNWs from the bulk Si wafer is to control the etching direction of Si by simply varying the concentration ratios of HF to H₂O₂ in the etching solutions. It has been proposed and demonstrated that if a bulk Si wafer having vertically aligned SiNWs and AgNPs at the bottom as shown in figure 3.5 (c) is immersed into the etching solution with high concentration of H₂O₂, then the bases of the SiNWs become etched. The increased concentration of H₂O₂ donates more holes to Si which causes the oxidation rate of Si in contact with AgNPs to strongly increase [3.15]. Since the etching of oxidized Si cannot catch up with this strong oxidation rate, AgNPs react with the edges of SiNWs. The vertical etching of Si decreases and AgNPs sink into the edges of the base of SiNWs. Finally the bases of SiNWs are etched and become fragile. After removing the AgNPs the sample resembles the structures as shown in figure 3.6 below, and it is much simpler to cut off these wires from the bulk wafer at this point.

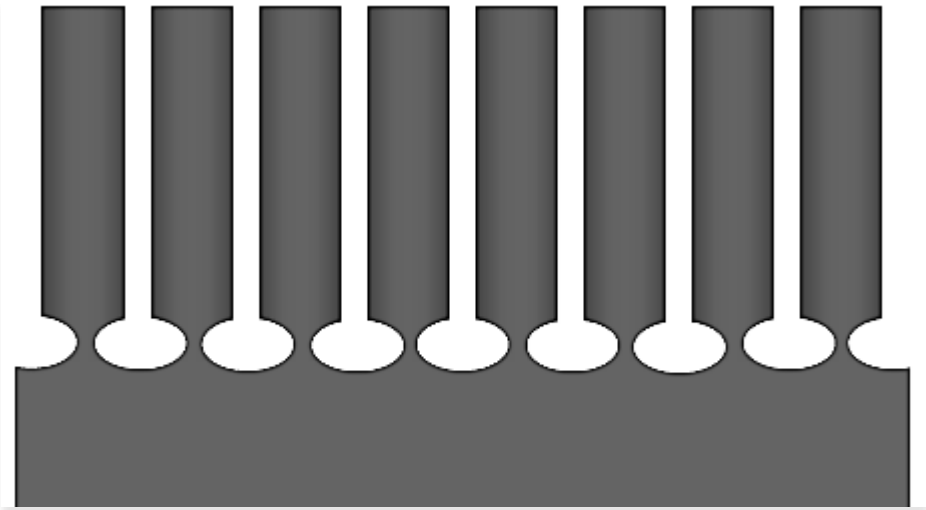


Figure 3. 6: Schematic representation of base etched SiNWs [3.15].

3.3 Experimental

3.3.1 Solution preparation

Solutions for SiNWs synthesis were prepared as shown in figure 3.7. The first solution was prepared by adding 5.2 ml of 48 % HF into 44.8 ml of DI water (H_2O) to make 5% HF solution. The second solution consisted of 170.2 mg of $AgNO_3$, 9.1 ml of HF and 40.9 ml of DI H_2O [3.16]. The third solution which is the normal etching solution (I) consisted of 2.6 ml of 34.0 % H_2O_2 , 9.1 ml HF and 38.4 ml of DI water [3.16]. The fourth solution consisted of 10 ml of H_2O_2 , 10 ml of HF and 30 ml of DI water; this is referred to as a high HF/ H_2O_2 concentration etching solution (II) [3.7]. Table 4.1 summarises the aforementioned solution preparation. The fifth solution was 70% nitric acid (HNO_3) while the sixth was just DI water. All chemicals used were purchased from Sigma Aldrich except H_2O_2 which was obtained from Merck.

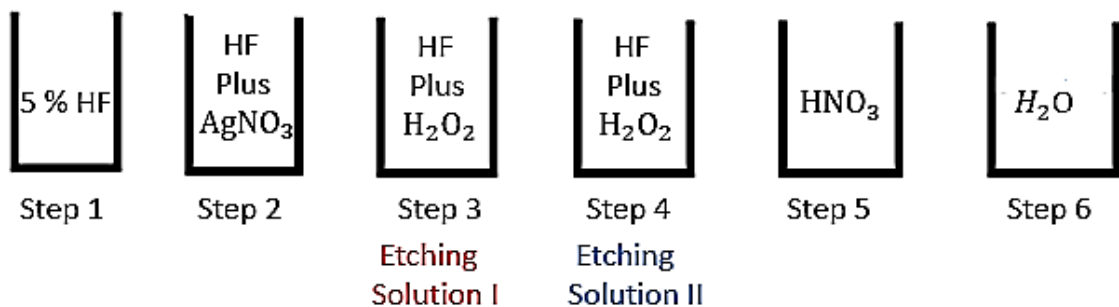


Figure 3. 7: Synthesising solutions and steps followed during SiNWs formations.

Table 3. 1: Summary of the solution preparation

Solution	48% HF (ml)	34 %H ₂ O ₂ (ml)	DI water (ml)	AgNO ₃ (mg)
5% HF sol	5.2	-	44.8	-
Metallisation sol	9.1	-	40.9	170.2
Etching sol (I)	9.1	2.6	38.4	-
Etching sol (II)	10	10	30	-

3.3.2 Synthesis process

Before the etching process could proceed, a 380 µm thick n-type Si wafer with a resistivity 1-10 Ω.cm was cut into 4 cm² pieces. These smaller pieces of Si wafer were cleaned by sonication in acetone and ethanol for 5 minutes each, consecutively. Then the wafers were rinsed in DI water and left to dry in ambient. After the cleaning process the wafers were immersed in 5% HF for 1 minute in order to remove the oxide layer before AgNP deposition could commence; this formed the first step of SiNW synthesis as shown in figure 3.7. The second step involved the immersion of previously cleaned wafers into a HF/AgNO₃/H₂O solution for AgNP deposition. The vertical etching of the Si wafer which is step 3, occurred as soon as AgNP-coated wafers were immersed in the HF/H₂O₂/H₂O solution. Step 4 is the horizontal etching of the Si wafer; this occurred when the previous vertically-etched Si wafers were immersed in a high concentration of HF and H₂O₂, solution (II). These wafers were immersed in this solution for different durations from 2-8 minutes with an increment of 2 minutes. The fifth step was the removal of AgNPs from the bases of SiNWs by immersing the wafer in HNO₃ for 3 minutes [2.2, 3.17]. The sixth and final step includes the removal of residual AgNPs by rinsing the synthesised SiNW samples in DI water. It is important to mention that in between the synthesising step, the Si wafer was rinsed in DI water to remove remains from the previous step.

3.3.3 Detachment of SiNWs

In order to detach SiNWs from the bulk Si wafer, the base etched SiNWs samples were immersed in 5% HF for 3 minutes to remove the oxide layer from the wires [3.18]. The wafer was then immersed in a binary solvent (1:1) of dichlorobenzene (DCB) and chloroform (CF), and sonicated in an ultrasonic bath for 10 minutes during which the

fragile bases of the SiNWs break, leaving them in the binary solvent. Then the remaining SiNW-free bulk Si wafer was removed from the solution containing the wires.

3.4 Results and discussion

3.4.1 Silver nanoparticle deposition

MACE of the Si wafer begins with AgNP deposition. Previously, researchers have attempted to optimise the electroless AgNP deposition by varying the concentration of AgNO_3 , HF acid and immersion time, where it was observed that there is a trade-off among the three parameters and that AgNP deposition continues until the wafer is removed from the metallization bath [3.13], [3.19, 3.20]. In this study, AgNPs were deposited by immersing the Si wafer in the metallization bath consisting of 170.2 mg of AgNO_3 , 9.1 ml HF and 40.9 ml H_2O for the duration of 60 s [3.16]. The morphology of the as-deposited AgNPs is shown in figure 3.8 (a). Figure 3.8 (a) clearly reveals that most of the Si surface is covered by spherical AgNPs that are randomly distributed on the surface. One may observe that the as-deposited AgNPs vary in size which is a result of non-uniform Ag^+ ion flux landing on the Si wafer. Analysis of AgNP size distribution is shown using the histogram in figure 3.8 (b), which indicates an average AgNP diameter of $\sim 288 \pm 5 \text{ nm}$.

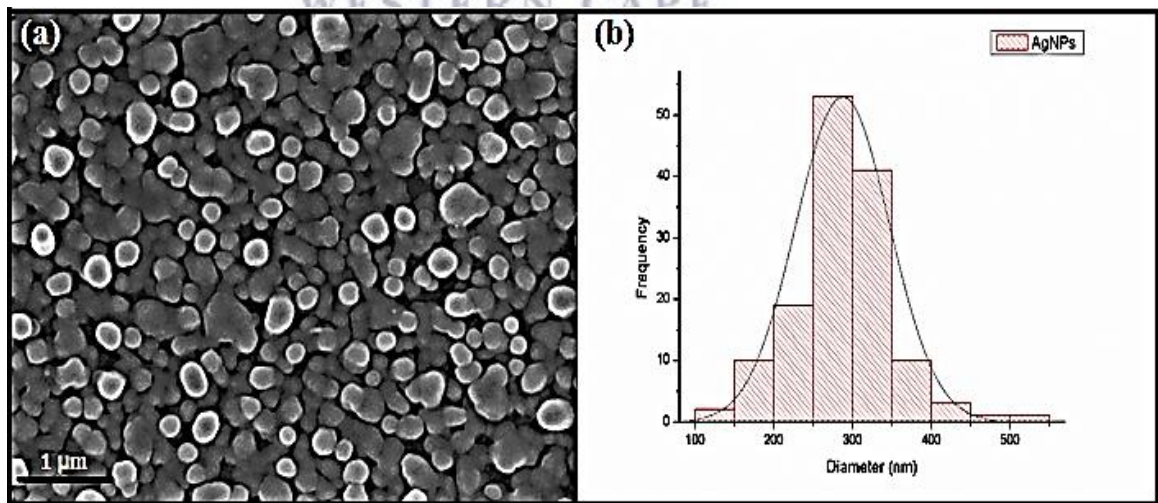


Figure 3.8: (a) SEM image of AgNPs deposited on an n-type Si (100) wafer by immersion in an aqueous solution of AgNO_3 and HF at room temperature for 60 seconds and (b) size distribution histogram of AgNPs.

Quantitative EDS analysis was performed on a AgNP-deposited Si wafer to determine the chemical composition of NPs observed in figure 3.5 (a). Figure 3.9 show the EDS spectrum obtained which indicates predominant signals for Si and Ag with the weight percentage of 76.5 % and 22.3 % respectively. However, additional signals of C and O are also observed. The C signal is due to the fact that the sample was coated with a C layer prior to the insertion into the SEM as it is a requirement that a sample to be analysed must be conductive to avoid charge build up on the surface of the sample. The O signal is believed to originate from the H₂O that formed part of the metallization solution and/or oxidation of the sample surface, since AgNPs deposition was done in ambient conditions. Therefore figure 3.9 verifies that deposits are indeed mainly pure Ag.

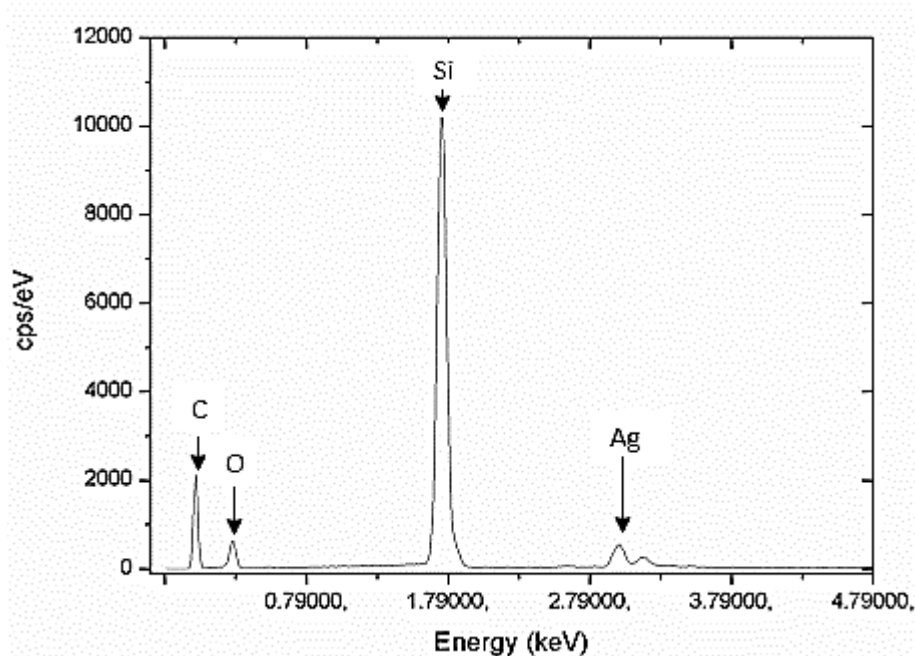


Figure 3. 9: EDS spectrum of AgNPs on the n-type Si (100) wafer.

3.4.2 Silicon nanowires formation

The mechanism of SiNW formation has been discussed in this chapter where chemical reactions involved in the mechanism were also outlined. Here we discuss the morphology of the as-synthesised SiNWs. Depending on the size of deposited AgNPs, H₂O₂ and HF concentrations, and etching time, different Si nanostructures can be realised. Figure 3.10 (a) shows the cross sectional image of AgNPs/SiNWs formed after etching the AgNP- coated Si wafer in the aqueous solution of HF/H₂O₂/H₂O for 10 minutes. It is evident from the figure that even for shorter etching time vertically

aligned SiNWs are realized. AgNPs are found at the bottom of SiNWs and in spaces between wires. The length of the realised SiNWs is $\sim 1.1 \mu\text{m}$ as measured by SEM. Figure 3.10 (b) shows the cross sectional image of AgNPs/SiNWs that was etched on the same aqueous solution for 20 min. As expected, the length of as-grown SiNWs has increased to $\sim 4.5 \mu\text{m}$. This is in accordance with the MACE mechanism of Si for the formation of SiNWs proposed in literature. The etching of Si proceed and the lengths of SiNWs increase for as long as H_2O_2 and HF are still available in the reaction vessel [3.21, 3.22]. AgNPs are also observed at the SiNWs/Si interface which confirms the growth mechanism that was discussed earlier, i.e. that AgNPs dictate the morphology of the resulting SiNWs in terms of diameter and density. In essence, the Si wafer underneath AgNPs is etched away by HF and form pits while the sites that were uncovered by AgNPs remain unetched and becomes SiNWs [3.23, 3.24]. On the basis of evidence in the micrographs in figure 3.10 (a) and (b), it is confirmed that the length of SiNWs indeed depends on the etching duration. The SiNWs observed in figure 3.10 (b) are homogenous compared to the ones realised in figure 3.10 (a). This implies that the etching of Si in HF/ H_2O_2 / H_2O becomes directional with time [3.25]. The morphology of the samples after the immersion in HNO_3 and rinsed in DI water are shown in figure 3.10 (c) and (d). Figure 3.10 (c) shows the cross section of AgNP-free SiNWs. It is apparent from the figure that HNO_3 does not influence the morphology of SiNWs but rather dissolves the AgNPs. The top view micrograph of vertically aligned SiNWs depicted in figure 3.10 (d) exhibits the formation of bundle-like structures at the tips of some SiNWs. Researchers have attributed this feature to a number of things. Some ascribe it to the Van der Waals forces between tips of SiNWs that take part during the etching process [3.26], while others ascribe this conglomeration to the strong mutual attractive force between newly formed SiNWs caused by dangling bonds and electrostatic charge [3.25].

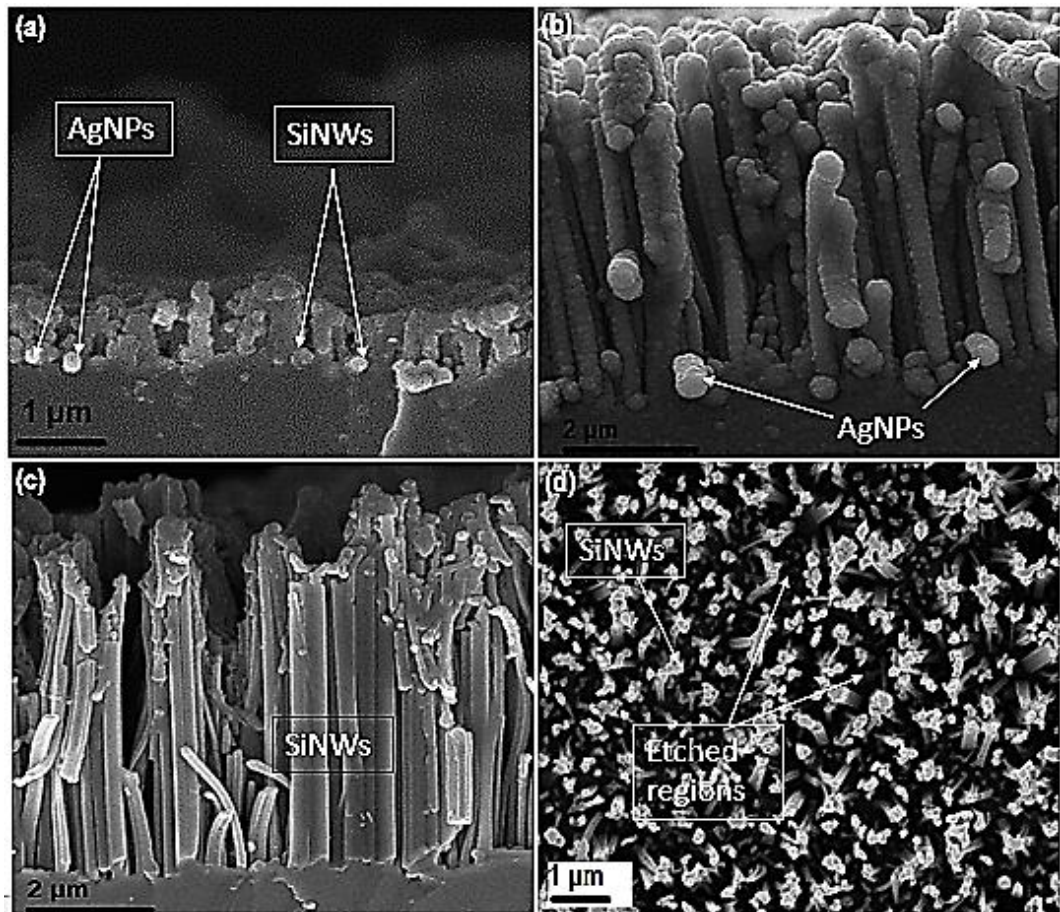


Figure 3. 10: SEM micrographs of (a) and (b) cross sectional images of AgNPs/SiNWs etched for 10 and 20 minutes respectively, (c) and (d) the cross sectional and top view image of AgNP-free SiNWs etched for 20 minutes, respectively.

Notwithstanding the presence of bundle-like structures on the tips of some SiNWs, we set out to determine the diameters of the SiNWs. Figure 3.11 (a) and (b) shows the diameter-distribution histogram of SiNWs and the quantitative EDS spectrum of as-synthesised n-type SiNWs, respectively. The graph in figure 3.11 (a) shows that as-synthesised SiNWs have different diameters. This illustrates that it is not very straightforward to control the size of SiNWs synthesised using MACE. Nonetheless, the average diameter of as-synthesised SiNWs is $\sim 226 \pm 4$ nm. Figure 3.11 (b) shows the EDS spectrum of SiNWs after the immersion of the sample into the HNO_3 solution. The EDS spectrum shows that the chemical composition of the sample is predominantly Si with a weight percentage of 98.2 %. Some imprints of O with a weight percentage of 1.8 % could be traced as well, which could be attributed to the same reasons mentioned during the discussion above of the EDS results of AgNPs on the Si wafer. It was

gratifying to obverse no evidence of Ag on the sample. This means that 3 minutes immersion of the SiNW samples into the HNO₃ solution is sufficient to dissolve all AgNPs at the NWs tips and also in the valley among SiNWs. These results are in accordance with EDS results from literature [1.63], [3.27].

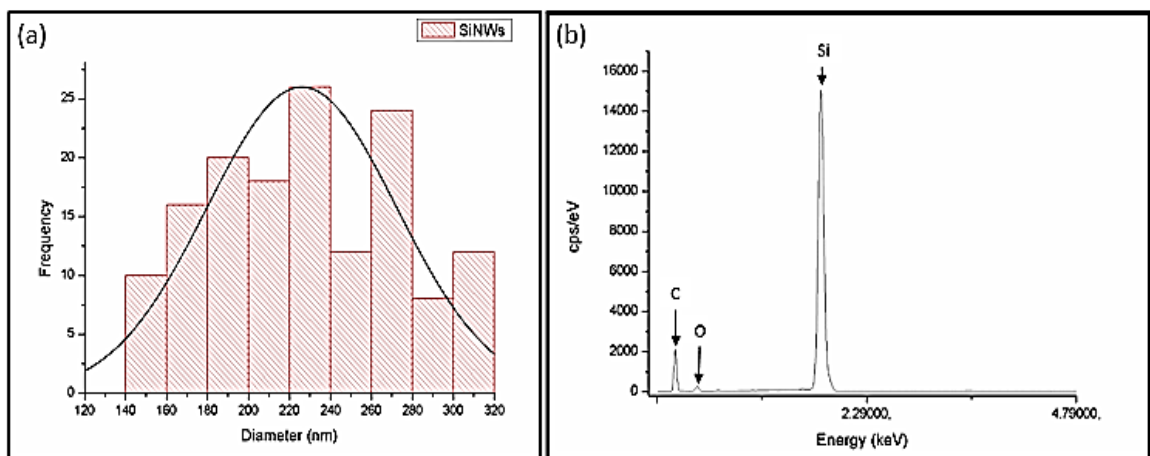


Figure 3. 11: (a) Histogram distribution of SiNW diameters and (b) the EDS spectrum of as-synthesised n-type SiNWs.

3.4.3 Horizontal etching

The as-synthesised SiNWs were not removed from the Si wafer by means of mechanical force. Rather, the bases of SiNWs were chemically etched by controlling the H₂O₂ concentration and subjected to sonication to break off the NWs. The SEM micrographs of the root-etched SiNWs are shown in figure 3.12. The sample that was immersed in solution II for 2 minutes (Figure 3.12 (a)) depicts poor lateral etching. From figure 3.12 (b), (c) and (d), which are the samples that were immersed in solution II for 4 minutes, 6 minutes and 8 minutes, respectively, the base etching of SiNWs is clearly visible. In addition, it is apparent from figure 3.12 that the degree of lateral or horizontal etching of the bases of SiNWs increases with immersion time. A comparison of the images in figure 3.12 (a)–(d), shows no significant variation in the length of SiNWs. These results are in correspondence with the results obtained by Liu et al., and Rajkumar et al. [3.7, 3.28]. In their findings, they attributed the enhanced horizontal etching to the high oxidation rate of the Si wafer around the AgNPs due to an increase of H₂O₂ concentration. Here H₂O₂ acts as a driving force in the oxidising mechanism. It supplies more holes to the Ag atoms of AgNPs and convert them to Ag⁺ ions which then attract more electrons from the Si surface leading to a high oxidation rate. For a fixed HF

concentration, the etching rate remains unchanged. The Ag/Ag⁺ have higher electronegativity than Si, and AgNPs interact with Si in all directions [3.7] [3.28]. This means that the AgNPs start to oxidise and sink into the bases of SiNWs resulting in SiNWs with fragile bases as can be seen in figure 3.12 (d) in particular. It can be suggested from figure 3.12 that the side wall etching of SiNWs increases as the immersion time of samples in solution II is prolonged.

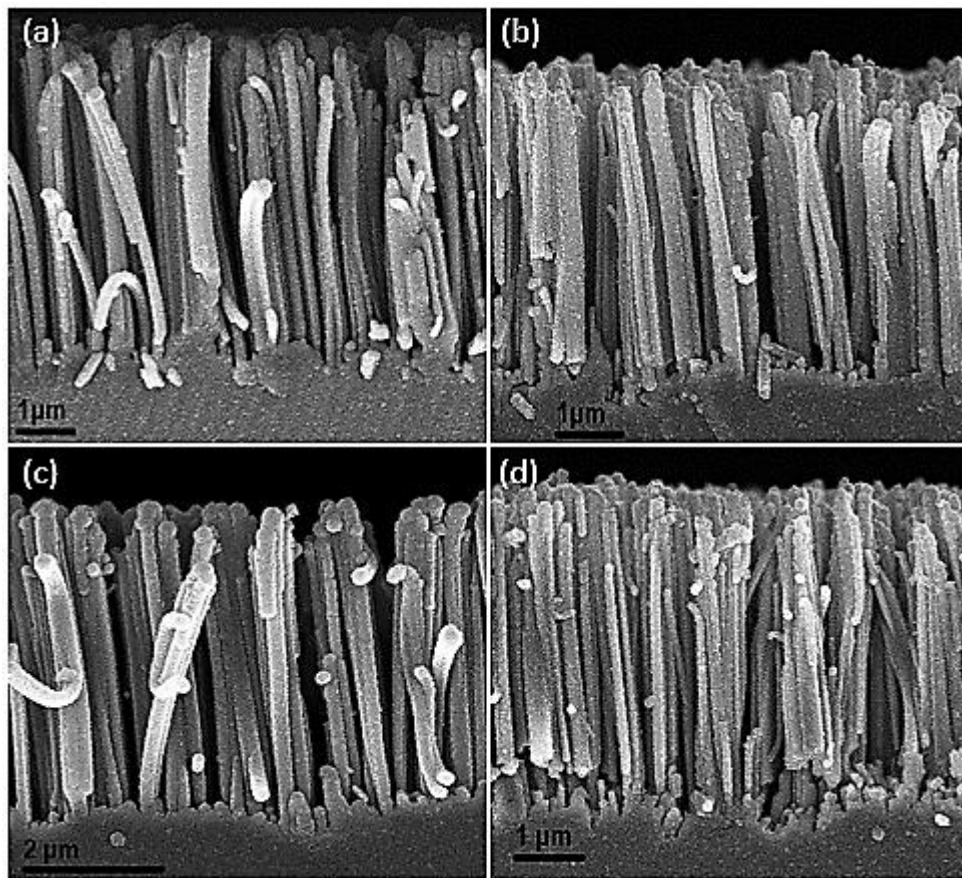


Figure 3. 12: SEM cross-sectional micrographs of base etched SiNWs in the etching solution II for (a) 2 minutes, (b) 4 minutes, (c) 6 minutes and (d) 8 minutes.

The horizontal etching of the bases of SiNWs could be seen from the cross sectional micrographs depicted in figure 3.12. However, to further our understanding as to what really happens during sonication we analysed the Si wafer after detachment of SiNWs. Figure 3.13 shows the top view micrographs of Si wafers after sonication for 10 min in the binary solvent of DCB and CF with a ratio of (1:1). It is evident from figure 3.13 (a) that immersing samples in solution II for 2 minutes did not remove all the wires from the wafer. Very short stubs of the remaining SiNWs could still be observed on the wafer after sonication. Some SiNWs were still adhering to the wafer as shown in figure 3.13 (b), which was immersed in solution II for 4 minutes. However, figure 3.13 (b) shows

much better results compared to figure 3.13 (a) in terms of detachment. The horizontal-lying SiNWs on the wafer could be rootless and have remained not because they are still attached on the wafer, but because they were not properly shaken to remain in the SiNWs/DCB/CF solution. Figure 3.13 (c) and (d) depict samples that were immersed in solution II for 6 and 8 minutes, respectively. In both cases the SiNWs were removed from the wafer completely. However, the degree of removal was not the same; figure 3.13 (d) shows that immersing SiNWs samples in solution II for 8 minutes was slightly extreme because the remaining wafer was starting to be affected by H₂O₂. These results are in accordance with what was observed in figure 3.12, which confirms the suggestion that the bases of SiNWs become fragile with increasing immersion time in solution II, which contains a higher concentration of H₂O₂. Based on these results, immersing the SiNWs sample in solution II for 6 minutes for etching the bases of SiNWs to ease the detaching process was considered our optimised condition.

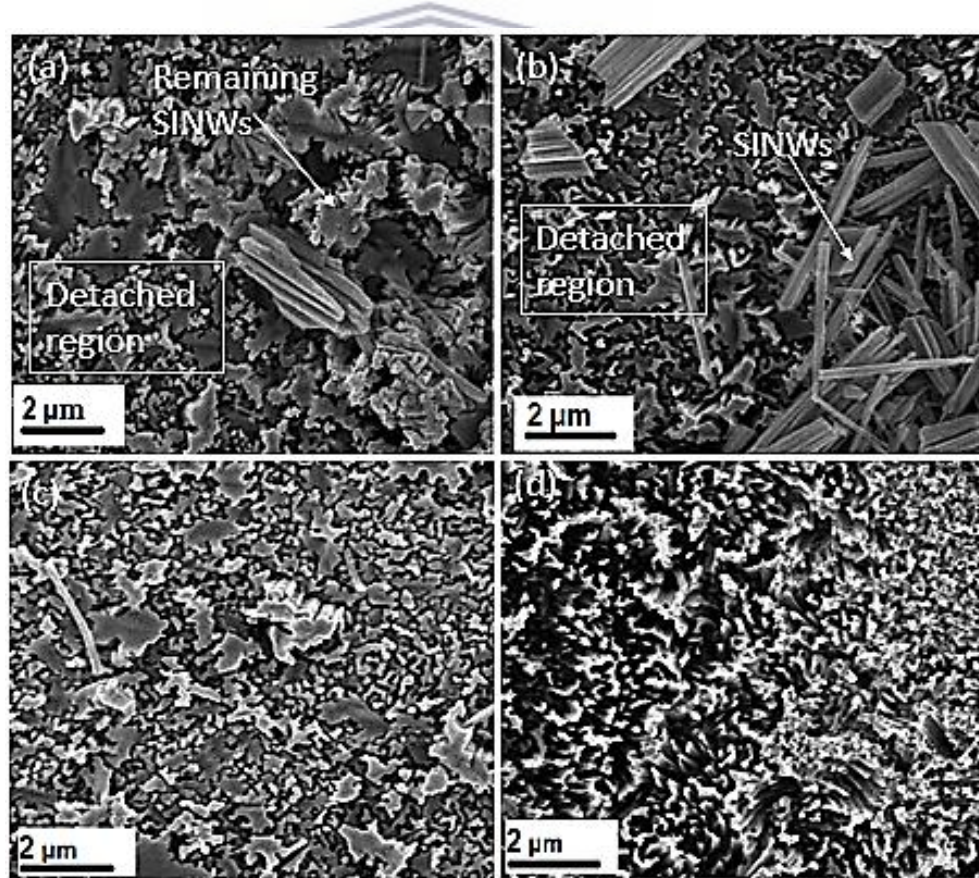


Figure 3. 13: SEM images of n-type Si wafers after SiNWs detachment through sonication. These samples, (a), (b), (c) and (d) were immersed in etching solution II for 2, 4, 6 and 8 minutes, respectively.

3.4.4 Transfer of SiNWs onto another substrate

Four solutions of SiNW/DCB/CF were prepared during the detachment of SiNWs through sonication. The difference among these solutions was the duration for which SiNWs samples were immersed in solution II, which was responsible for etching the bases of SiNWs. Based on the results that have been presented in the current chapter, one can surmise that the concentration of SiNWs in the binary solvent of DCB: CF varies amongst the four solutions. Therefore the same volume of 50 µl from each SiNW/DCB/CF solution was drop-casted on the glass substrate and the solvent was allowed to dry in order to examine post detachment morphologies of SiNWs. Figure 3.14 shows the top view micrographs of SiNWs deposited on the glass substrate; the scale bar is the same for all images. The SiNWs were randomly deposited on all glass substrates as can be observed from figure 3.14 (a-d). In addition, the as-deposited SiNWs vary in length which suggests that NWs break randomly during sonication. Bunches of SiNWs were observed in figure 3.14 (a), where the bases of the wires were etched for 2 minutes. This suggests that for shorter etching-time of the bases the SiNWs are detached in clusters. The variation in diameters of wires pronouncedly observed in figure 3.14 (b) (4 min) in particular is not surprising since it was observed from figure 3.11 (a) that SiNWs of the same sample are not necessarily of the same diameter. The morphologies of SiNWs observed in figure 3.14 (c), which were horizontally etched for 6 min shows interesting results. Here, the wires are approximately of the same length and the degree of the variation in the diameter of these wires is at a minimum which could be advantageous for fabrication of solar cells. Figure 3.14 (d) reveals that further increasing the horizontal etching time deteriorates the detaching process.

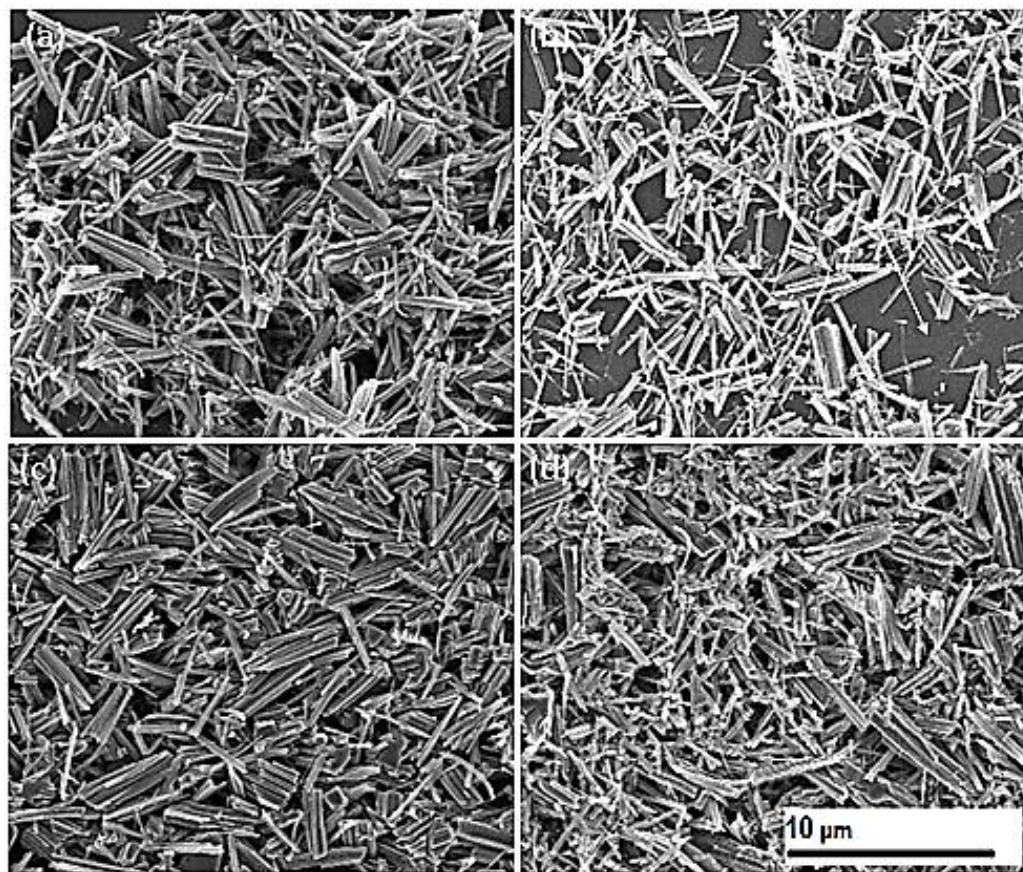


Figure 3. 14: SiNWs deposited on a glass substrate. These correspond to the wafers depicted in figure 3.13 above.

3.4.5 TEM characterisation of SiNWs

The in-depth examination of the nanostructure and crystallinity of as-synthesised SiNWs was carried out using TEM characterisation. According to figure 3.15 (a), SiNWs produced have smooth surfaces with no pores observed. This observation is consistent with the results obtained by Bai et al [3.29] and Peng et al [3.30]. Figure 3.15 (b) shows a high-magnification image of the single SiNW where it is evident that the core of the wire is crystalline (dark colour) and the surface is covered by an amorphous layer in the form of SiO_x (pale colour) [3.31, 3.32]. This is in correspondence with what is depicted by figure 3.11 (b), that there are traces of O within SiNWs which we can now confidently attribute to SiO_2 . The high resolution (HR) TEM image and selected area electron diffraction pattern (SAED) shown in figure 3.15 (c) and (d), respectively, confirms that the core of the SiNWs retain the single crystalline structure of the starting Si wafer; this is in consistent with conventional wisdom, [3.33-3.34]. This means that during etching the AgNPs, HF and H_2O_2 do not destroy the integrity and continuity of

the Si lattice [3.29, 3.35]. According to the HRTEM micrograph in figure 3.15 (c), an interplanar spacing (d-spacing) of 0.129 nm corresponds to axial orientation of [001], which confirms that except for the shells of wires which comprise an amorphous layer , no other impurities can be observed (i.e. satisfactory purity of the as-prepared SiNWs) . This corresponds with the various results from literature, [3.32, 3.36].

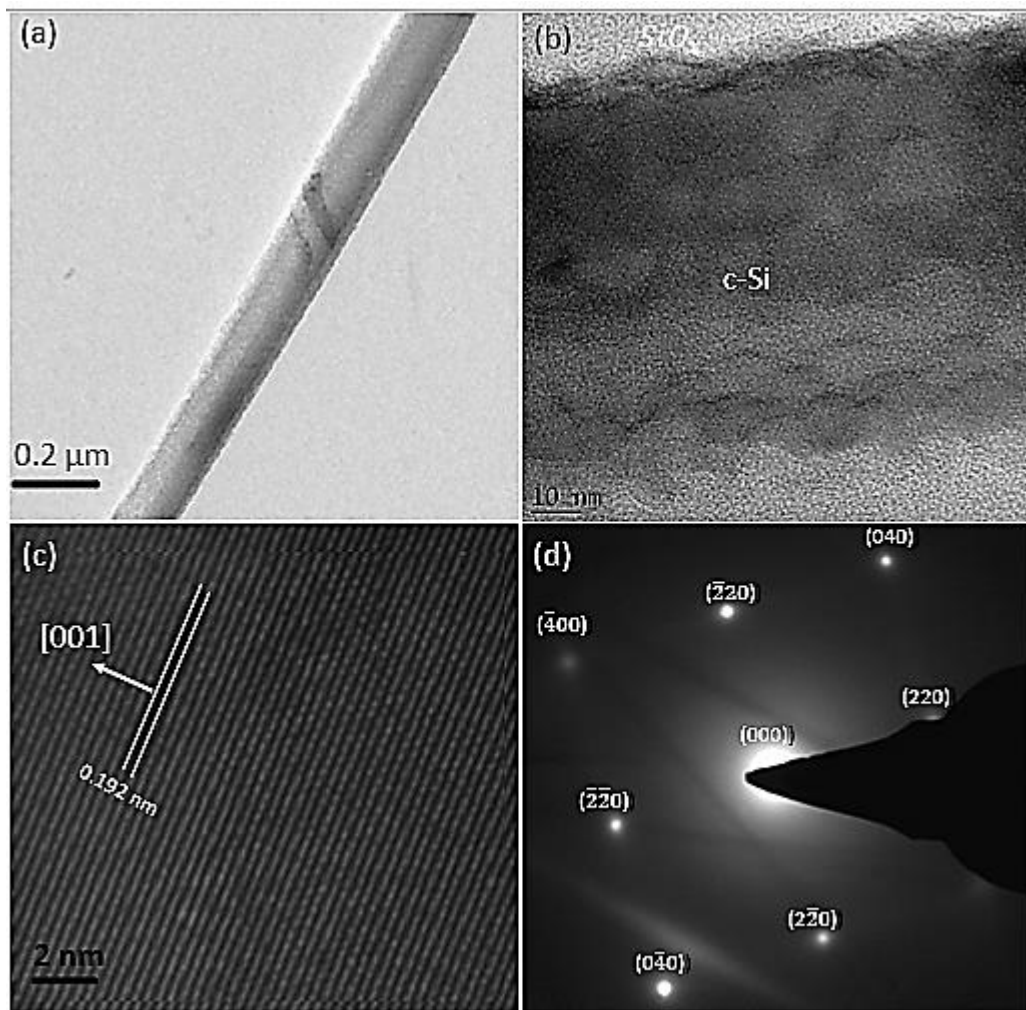


Figure 3. 15: TEM characterisation of an as-synthesised single SiNW, with (a) and (b) low and high magnification TEM micrographs, (c) is the HR-TEM micrograph and (d) is the SAED pattern of as-synthesised wire.

3.4.6 Optical properties of SiNWs

The length of SiNWs after the base etching did not significantly change. Therefore the optical measurement (i.e. UV-vis-NIR and photoluminescence) were taken for the sample that was horizontal etched in a high concentration of HF and H₂O₂ for the duration of 6 minutes. Figure 3.16 shows the optical absorption spectrum of SiNWs which shows that SiNWs exhibit some extent of anti-reflecting property. It is evident

from the spectrum that the overall absorption of incident radiation (photons) by the as-deposited SiNWs is above 35% for the whole wavelength range (300-1200 nm). In addition, SiNWs exhibit more absorption intensity between 345 nm and 641 nm wavelengths which can reach the maximum of 57%. These results are in accordance with previous studies done by Liu et.al and Qu et.al where they observed that SiNWs exhibit high absorption of photon energy compared to the bare Si wafer across the entire UV-vis region [3.7, 3.37]. They attributed this reduced reflection or high absorption of photon energy behavior to superior quantum confinement of photons due to surface texturing of the Si wafer upon etching [3.7].

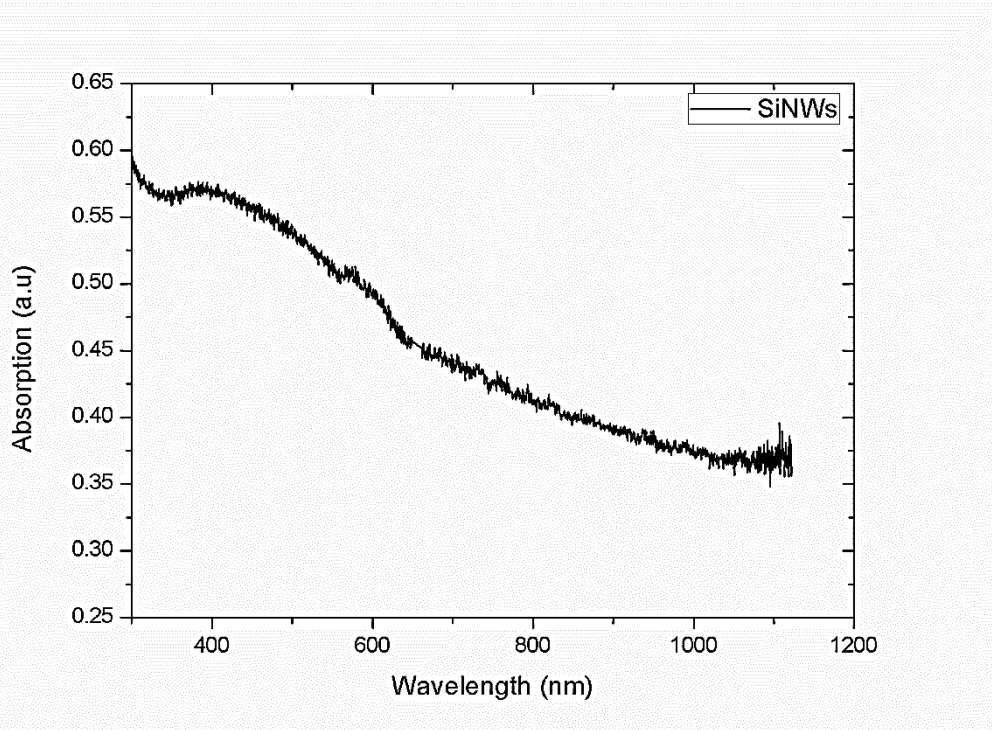


Figure 3. 16: Optical absorption spectrum of n-type SiNWs over a wavelength range of 300-1200 nm.

The intensity, the peak position and decay time of SiNWs or any PL semiconducting material are very sensitive to the doping level amongst other things [3.38]. Figure 3.17 depicts the PL spectrum exhibited by SiNWs that were deposited on the glass substrate in a spectral region of 710-730 nm with a maximum PL peak around 720 nm. The broad and roughly symmetric PL peak observed from the figure is in accordance with what has been discussed in literature [3.38, 3.39]. In literature, this behavior is attributed to the direct radiative recombination of excitons in small Si crystals at the nanowire side

walls due to the Si band gap which is increased and modified from indirect to direct with respect to porosification-induced Quantum Confinement (QC) [2.11, 3.38-3.39].

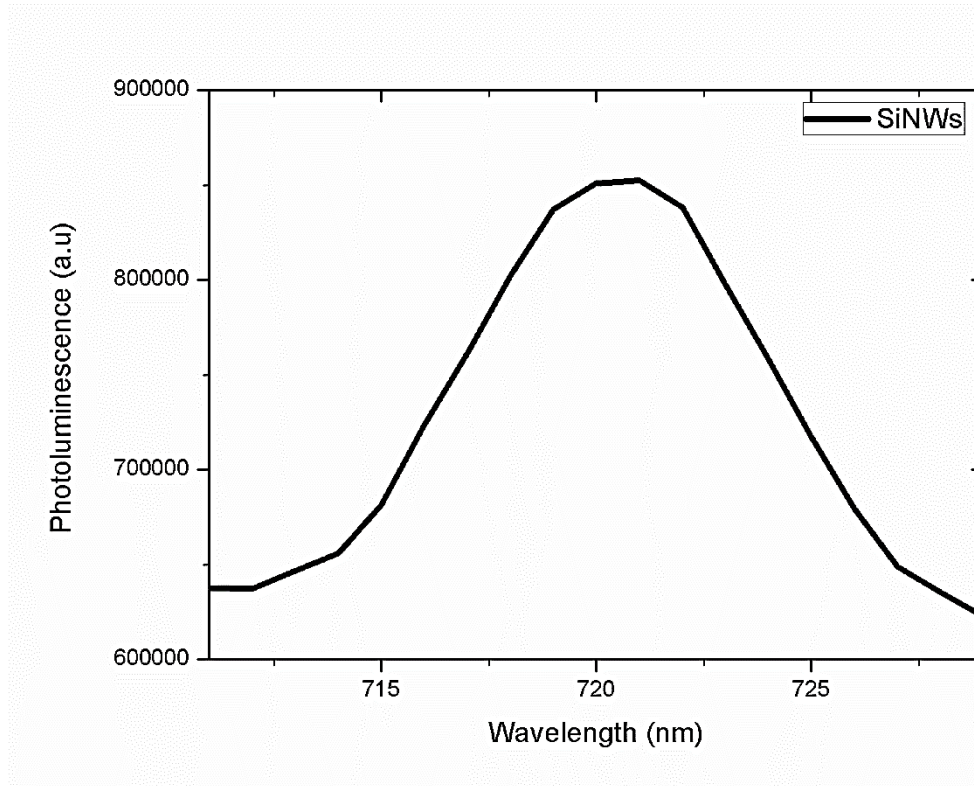


Figure 3. 17: Photoluminescence spectrum of n-type SiNWs.

3.5 Conclusion

In conclusion, SiNWs have been synthesised using a conveniently controllable technique, MACE. The results obtained are consistent with the MACE mechanism proposed in literature. It was observed that the initial step of the synthesis process (AgNP-deposition) amongst others, control the morphology of the resulting SiNWs to such an extent that the randomness of deposited AgNPs result in the variation of SiNW-size in the same sample. We demonstrated the technique of detaching SiNWs from the bulk Si wafer by controlling the direction of metal assisted etching and subjecting the samples to sonication which resulted in a massive yield of SiNWs. The wires obtained revealed high Si purity with low levels of O impurity which was attributed to natural oxidation. It was quite remarkable to observe that the SiNWs retained the crystallinity of the mother Si-wafer, which meant that the chemicals that were used, i.e. AgNPs, HF and H₂O₂ do not destroy the integrity and continuity of the Si lattice.

References

- [3.1] Huang Z, Geyer N, Werner P, de Boor J and Gosele U 2011 *Advanced Materials* **23** 285
- [3.2] Dimova-Malinovska D, Sendova-Vassileva M Tzenov N and Kamenova M 1997 *Thin Solid Films* **297** 9
- [3.3] Wan L, Gong W, Jiang K, Li H, Tao B and Zhang J. 2008 *Applied Surface Science* **254** 4899
- [3.4] Brahit N, Bouanik S A and Hadjersi T 2012 *Applied Surface Science* **258** 5628
- [3.5] Asoh H, Arai F and Ono S 2009 *Electrochimica Acta* **54** 5142
- [3.6] Fang H, Wu Y, Zhao J and Zhu J 2006 *Nanotechnology* **17** 3768
- [3.7] Liu Y, Ji G, Wang J, Liang X, Zuo Z and Shi Y 2012 *Nanoscale Research Letters* **7** 663
- [3.8] Peng K, Hu J, Yan Y, Wu Y, Fang H, Xu Y, Lee S and Zhu J (2006) *Advanced Functional Materials* **16** 387
- [3.9] Smith Z R, Smith R L and Collins S D 2013 *Electrochimica Acta* **92** 139
- [3.10] Vinod P N 2005 *Semiconductor Science and Technology* **20** 966
- [3.11] Qu Y, Liano L, Li Y, Zhang H, Huang Y and Duan X 2009 *Nanoletter* **9** 4539
- [3.12] Toor F, Miller J B, Davidson L M and Nichols L 2006 *Nanotechnology* **27** 412003.
- [3.13] Chartier C, Bastide S and Clement C L 2008 *Electrochimica Acta* **53** 5509
- [3.14] Li X and Bohn P W 2000 *Applied Physics Letters* **77** 2572
- [3.15] Shiu S C, Syu H F, Hung S C and Lin C F 2010 *Nanotechnology Joint symposium* 474
- [3.16] Liu K, Qu S, Zhang X, Tan F and Wang Z 2013 *Nanoscale Research Letters* **8** 88
- [3.17] Amri C, Ouertani R, Hamdi A and Ezzaouia H 2017 *Materials Science in Semiconductor Processing* **63** 176
- [3.18] Davenas J, Boiteux G, Cornu D and Rybak A 2012 *Synthetic Metals* **161** 2623
- [3.19] Xia W, Zhu Y, Wang H and Zeng X 2014 *CrystEngComm* **16** 4289
- [3.20] Zaghouani R B, Manai L, Rezgui B D and Bessais B 2015 *Chemistry Journal* **3** 90
- [3.21] Lin L, Guo S, Sun X, Feng J and Wang Y 2010 *Nanoscale Research Letters* **5** 1822

- [3.22] Bachtouli N, Aouida S, Bessais 2014 *Microporous and Mesoporous Materials* **187** 82
- [3.23] Nafie N, Braham C, Rabha M B, and Bouaicha M 2014 *Physica Status Solidi C* **11** 331
- [3.24] Sivakov V A, Bronstrup G, Pecz B, Berger A, Radnoci G Z, Krause M and Christiansen S H, 2010 *Journal of Chemical Physics C* **114** 3798
- [3.25] Zhang M-L, Peng K-Q, Fan X, Jie J-S Zhang R-Q, Lee S-T and Wong N-B 2008 *Journal of Chemical Physics C* **112** 4444
- [3.26] Bai F, Li M, Song D, Yu H, Jiang B and Li Y 2012 *Journal of Solid State Chemistry* **196** 596
- [3.27] Vinzons L U, Shu L, Yip S P, Wong C-Y, Chan L L H and Ho C J 2017 *Nanoscale Research Letters* **12** 385
- [3.28] Rajkumar K, Pandian R, Sankarakumar A, Rajendra Kumar R T 2017 *American Chemical Society Omega* **2** 4540
- [3.29] Bai F, Li M, Song D, Yu H, Jiang B and Li Y 2012 *Journal of Solid State Chemistry* **196** 596
- [3.30] Peng K, Lu A, Zhang R. and Lee S 2008 *Advanced Functional Materials*, **18** 3026
- [3.31] Wu L, Li S, He W, Teng D, Wang K and Ye C 2014 *Scientific Reports* **4** 3940
- [3.32] Su Z, Dickinson C, Wan Y, Wang Z, Wang Y, Sha J and Zhou W. 2010 *CrystEngComm* **12** 2793
- [3.33] Li S, Ma W, Zhou Y, Chen X, Xiao Y, Ma M, Zhu W and Wei F 2014 *Nanoscale Research Letters* **9** 196
- [3.34] Lee G, Schweizer S and Wehrspohn R 2014 *Applied Physics A* **117** 973
- [3.35] Ashrafabadi S and Eshghi H 2018 *Journal of Materials Science: Materials in Electronics* **29** 6470
- [3.36] Zhang C, Li S, Ma W, Ding Z, Wan X, Yang J, Chen Z, Zou Y and Qiu J 2017 *Journal of Materials Science: Materials in Electronics* **28** 8510
- [3.37] Qu Y, Zhong X, Li Y, Liao L, Huang Y and Duan X 2010 *Journal of Materials Chemistry* **20** 3590
- [3.38] Huang Z and Liu J 2015 *JSM Nanotechnology and Nanomedicine* **3** 1035
- [3.39] Gonchar K, Zubairova A, Schleusener A, Osminkina L and Sivakov V 2016 *Nanoscale Research Letters* **11** 357

4 INCORPORATION OF SINWS INTO RR-P3HT MATRIX FOR SOLAR CELL APPLICATION.

4.1 Introduction

Research towards the development of low cost renewable sources of energy has gained tremendous interest over the last two decades. Inorganic PVs based on cSi are ubiquitous and exhibit good PCE. However, high temperatures and high vacuum required for the processing of Si and fabrication of this type of PV leads to high production cost, which needs to be minimised. On that note, other PV technologies such as those based on organic semiconductors have emerged as alternative candidates for the fabrication of PV technologies at low cost [4.1, 4.2], on flexible substrates. Conjugated polymers, thiophenes in particular paved the interest in conducting polymer materials and their applications [4.3]. P3HT with its regioregular (head-to-tail) isomer, first synthesised by Rick McCullough in 1992 has been a model polymer for various fundamental studies relating to thin film morphology and charge transport [4.4]. The regioregularity of P3HT is of great importance for specific characteristics of the polymer such as charge carrier mobility, charge transport and overall electrical conductivity of the film [4.5]. In organic photovoltaics (OPVs), the PCE is affected by the morphology of the active layer, the structure and the choice of electron D and A materials, the ratio of these materials and the interaction in the D-A interface within an active layer [4.6]. The major setback associated with OPVs amongst others involves the

low PCE, which is related to limited charge carrier mobility, as a result of a rapid recombination rate within the active layer [4.7]. In dealing with shortcomings associated with OPVs, methods such as incorporating inorganic materials into polymer matrices have been developed and employed [4.8-4.10].

Hybrid solar cells combine advantages of both organic and inorganic materials. Here the conjugated polymer absorbs light and acts as the electron D, whereas the inorganic material act as an electron A and transporter in the structure. In our hybrid films, rr-P3HT is employed for its good optical absorption and hole transporting ability arising from the crystalline ordering, whereas SiNWs offer high surface area per volume ratio providing a large interface for exciton dissociation, therefore leading to high mobility of electrons [4.11]. The quality of the hybrid films strongly depend on the deposition technique, film processing conditions, choice of solvent and the nature of the substrate [4.12-4.13]. The optimisation of the processing conditions used to prepare hybrid films with an objective to maximize the electrical properties is still a difficult task in which molecular and macromolecular parameters have to be taken into account [4.5]. Different thin film deposition techniques have been explored in literature; however the sol-gel method (spin coating in particular) was employed in the present study.

4.2 Spin coating technique

4.2.1 Introduction

Spin coating is a frequently-used technique in industries and technology sectors to deposit uniform thin films of desired materials mainly on flat substrates. With a spin coater the thickness of films produced range from a few nanometres to hundred micrometres. The first spin coating procedure was done for coating of paint and pitch by Emslie et.al in 1958 [4.14]. However, to date, the technique finds its usefulness in various applications such as PVs, colour television screens, coatings of photoresist on Si wafers, sensors, protective coatings, optical coatings and membranes [4.15-4.16]. More often, the coating material is polymeric and is applied in the form of solution from which the solvent then evaporates to leave a solid film on a substrate. The thickness of the film depends on the rotational speed, the viscosity and concentration of the solution, and the type of the solvent used [4.17]. Even though spin coating has proved not to be an ideal technique to use when extremely thin and high uniform films are desired, it

holds some advantages such as fast and cheap film fabrication, spin coating repeatability, easy control and handling of chemicals and substrates [4.18].

4.2.2 Spin coating mechanism

During the spin coating process, a small amount of coating material is delivered on the centre of the substrate. The substrate is then spun at high speed in order to spread the coating material over the surface of the substrate. Rotation continues until the desired thickness of the film is obtained. The process can be divided into four stages: deposition, spin-up, spin-off and solvent evaporation as shown in figure 4.1 below [4.19].

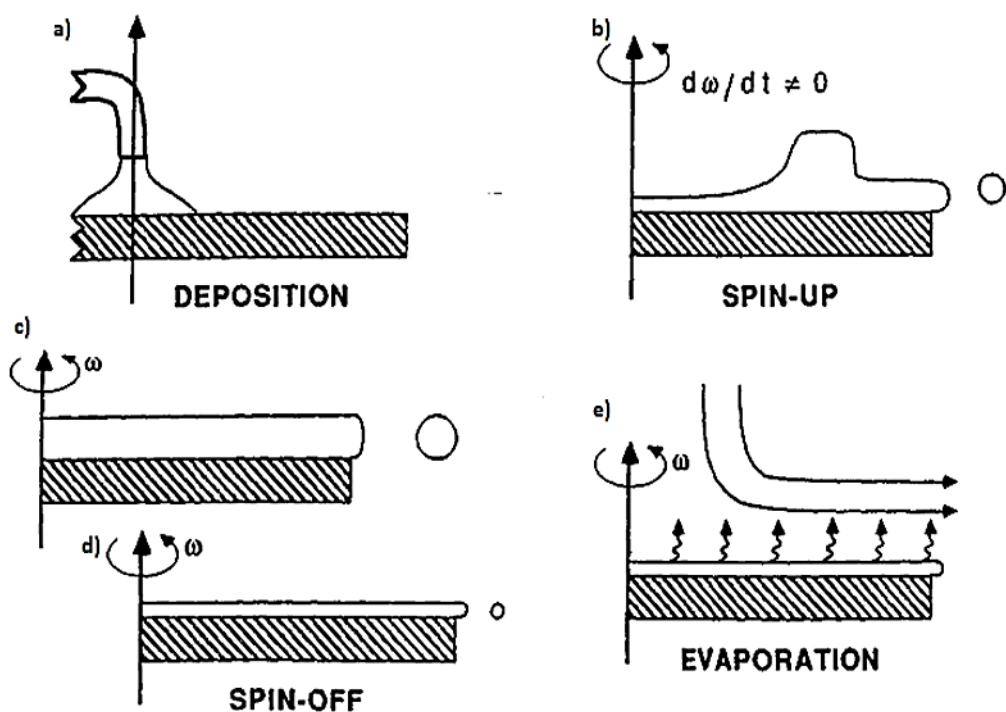


Figure 4. 1: Different stages of spin coating deposition process [4.19].

Deposition is the stage of delivering the fluid to be coated onto the surface of the substrate, as in figure 4.1 (a). The solution of the material of interest can be deposited onto the substrate which is either stationary (static dispense) or rotating at low speed (dynamic dispense). Dynamic dispense is frequently used for solutions and substrates that have poor wetting ability where a rotational speed of 500 rpm is commonly used to spread the fluid over the substrate due to the centrifugal force before spin-off takes over [4.19, 4.20]. Dynamic dispense leads to less waste of the fluid since it is not necessary to dispense an excess amount of the fluid to wet the entire surface of the substrate.

Spin-up is the second stage of spin coating whereby the substrate is rotationally accelerated to its desired speed. During this stage, the fluid is flung off the edges of the substrate rapidly due to aggressive rotational motion as shown in figure 4.1 (b). During this stage, different mechanisms come into play whereby fluid inertia and surface tension have essential influence [4.14]. During early seconds of this stage, the fluid amount which is far more than the coating to be produced requires, is flung off the substrate. Further, spiral vortices might be present due to the initial paths of the fluid on the substrate. These would form as a result of twisting motion attributed to inertia of the fluid as the rotational speed of the substrate is increased. Suddenly, the fluid becomes thin enough to be completely co-rotating with the substrate such that the fluid inertia and shearing thinning will no longer be important, as shown in figure 4.1 (c).

Spin-off is the third stage of spin coating that begins shortly after the inertial effects become negligible. This means that at this stage, initial conditions play little to no role in the film thinning. Here the substrate is rotating at a constant rate, and the thinning of the fluid is strongly due to the fluid viscous force. This stage is characterised by gradual fluid thinning as shown in figure 4.1 (d). The flow is balanced between the viscous and centrifugal forces and concentration of the fluid is uniform over the whole substrate. The fluid is assumed to be Newtonian with the viscosity depending significantly on the concentration [4.14]. It is often possible to observe progressive interference of colors as the coating thickness reduces [4.18, 4.20-4.23]. Edge beads are usually observed at the corners of the substrate during this stage because the fluid flow is radially outward. Therefore, depending on the surface tension, viscosity and rotational speed, there may be small beads of different coating thickness compared to the final thin film around the rim of the substrate.

Solvent evaporation is the final stage of the spin coating process, as shown in figure 4.1 (e). During this stage, the fluid viscosity rises rapidly so that the out-flow stops. Further fluid thinning is primarily due to solvent drying whereby the fluid concentration rises over the surface of the substrate resulting in the solidification of the fluid [4.24]. The drying rate of the fluid depends on the number of factors including solvent volatility, temperature and humidity around the coated substrate [4.21]. The film produced at the end of this stage is not completely solid; there is residual solvent which is removed by post thermal treatment such as baking the sample.

4.2.3 Spin coating experimental setup

A G3P-series Spin coater purchased from Specialty Coating Systems was used in this study. The machine is normally used in laboratory or manufacturing working environment. An overview of this spin coating system can be sophisticated, however for this work it was simplified as shown in figure 4.2 below. The main components of this spin coating system includes, the chuck, basin, lid, pump and nitrogen supply. The chuck was machined to close the tolerances and provide an extremely flat, rigid surface for mounting the substrates of different sizes, weights and shapes. The basin collects all excess coating solution during the spin cycle which was wiped as waste after the coating process was done. Hence it was important to balance the amount of dispersed solution between having enough to cover the whole substrate while having minimum waste at the same time. The lid of a G3P-series spin coater is used to hold the dispense bracket which has multiple needle mounting holes. However, in this case it was used mainly for the protection of the operator and others from injuries as the substrate and/or coating solution can fly off the rotating chuck during spin coating. The pump is used for vacuum supply; the machine will not complete a cycle without vacuum. Normally, the top surface of the chuck has a cross scroll pattern which is useful in distributing the vacuum from the pump over the chuck surface to hold the substrate, while spinning at high spin speed. In addition, the cross pattern also allows the rapid vacuum release from the pump. The nitrogen gas cylinder supplies the interior of the machine with N₂ to maintain positive pressure. This purge is required as a safety factor to fill and remove dangerous gasses from the interior of the machine. The machine does not operate without N₂ supply or clean, dry air. A two-step regulator was used to control and maintain pressure flow. In this study, minimum gas, only sufficient enough to keep the spin coater on, was required.

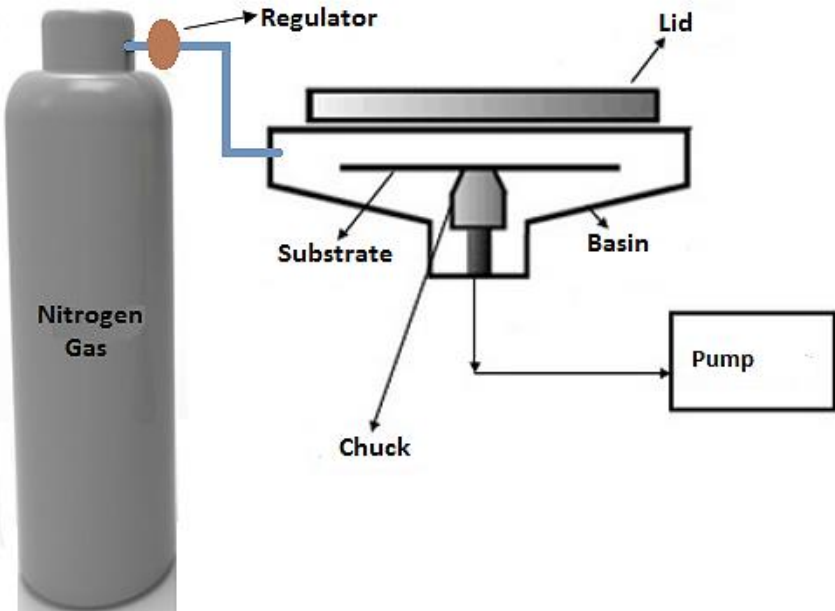


Figure 4. 2: Schematic representation of spin coating experimental setup [4.25].

4.2.4 Samples preparation and device fabrication

The conjugated polymer rr-P3HT (Sigma Aldrich) with a molecular weight average between 54000-75000 gmol⁻¹, was used as purchased without any further purification or modification. SiNWs were synthesized via MACE process as explained in the experimental section in chapter 3. Using the optimized SiNWs ink, obtained from etching the roots of SiNWs in etching solution II for 6 min, three solutions of different SiNWs concentrations by weight ratio were prepared: rr-P3HT: 0.3 wt% SiNWs, rr-P3HT: 0.7 wt% SiNWs, and rr-P3HT: 1.3 wt% SiNWs. The fourth solution of rr-P3HT dissolved in the binary solvent of DCB: CF (1:1) was used as a reference. These solutions were stirred overnight on a digital hot plate stirrer (Lasec) at rotational speed and temperature of 250 rpm and 23 °C respectively. Microscope slides with 1-1.2 mm thickness (Lasec) on which hybrid solutions were to be deposited, were consecutively cleaned in boiling hellmanex solution, and isopropanol in an ultrasonic bath and then rinsed in boiling DI water. The solutions were then deposited at 900 rpm for the duration of 100s using a G3P-series spin coater (Specialty Coating Systems) to form photoactive BHJ hybrid layers.

SCs were prepared on pre-patterned ITO coated glass obtained from Ossila and these substrates were cleaned in an analogous manner as for the characterization glass substrates. The first layer to be deposited was a PEDOT: PSS (solution obtained from

Sigma Aldrich) thin film which was spin coated at 5000 rpm for 30s and then dried on a 150° C hot plate for 5 minutes. The purpose of this layer was to serve as hole transporting layer and fill the voids on the surface of ITO. Subsequently, the active layers which consisted of rr-P3HT and different weight ratios of SiNWs (rr-P3HT:0.3 wt% SiNWs, rr-P3HT:0.7 wt% SiNWs and rr-P3HT:1.3 wt% SiNWs) were deposited at 900 rpm for 100s and then dried on a 150° C hot plate for 30 minutes. This was followed by the deposition of a 150 nm thick Al back contact which acted as the cathode electrode. This was obtained using the CADAR (Cluster Apparatus for Device Application Research) system housed in the Department of Physics and Astronomy at UWC. The deposition parameters i.e. deposition current, deposition pressure and the duration were 95 A, $\sim 5 \times 10^{-4}$ mBar and 2 minutes, respectively. Finally, the cells were encapsulated using encapsulation epoxy and glass cover-slips, to slow down the device degradation.

4.3 Results and discussion

4.3.1 Morphology

One of the key parameters that control the morphology of the active layer is the composition of materials of interest, i.e. the weight percent (wt %) ratio of the D and the A materials. To gain an insight of the organisation of SiNWs within the polymer matrix, the morphology of the films was characterized via SEM. The SEM micrographs of the rr-P3HT matrices incorporated with different SiNW concentrations are depicted in figure 4.3. It has been reported that film uniformity depend strongly on the choice of organic solvent used [4.26]. In this study, the binary solvent of DCB and CF was used due to the high solubility of the rr-P3HT in the former and quick evaporation of the latter, which together constructively influence the films produced. It is evident from figure 4.3(a) that the deposition conditions and post-deposition treatment used provided homogeneous films. It was satisfying to observe from figure 4.3 (b-d) that the incorporated SiNWs are imbedded in the polymer matrix and that SiNWs in the rr-P3HT matrix are randomly distributed across the active area. However, traces of SiNWs emerging out of the films could still be observed which led to the surface of the active layer to become rough with increasing load of SiNWs. These results are in correspondence with the results obtained by Braik et.al and Dkhil et.al [4.27, 4.28]. On the one hand, it is believed that a high concentration of SiNWs enlarges the D-A

interface, which could be suitable for effective exciton dissociation within the rr-P3HT: SiNWs active layer. On the other hand, the large number of wires could act as recombination sites; other complementing techniques such as Hall Effect and PL are employed to determine whether or not the concentration of SiNWs is favourable for successful charge separation.

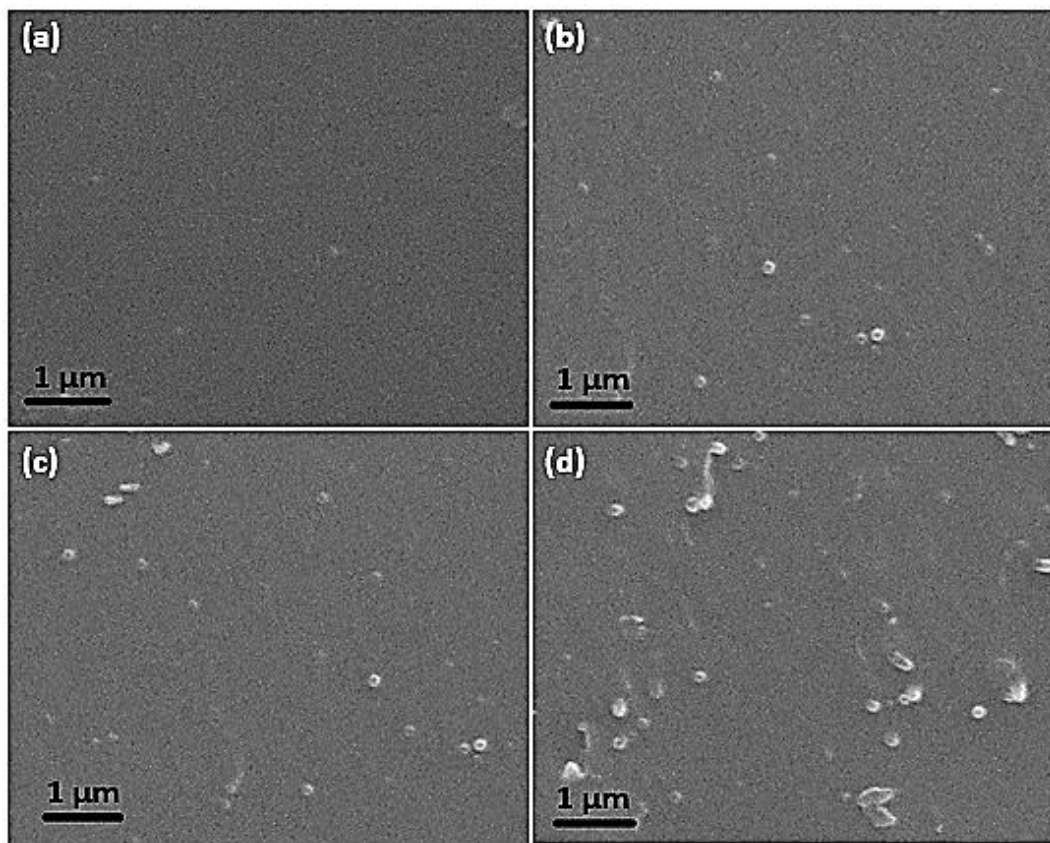


Figure 4.3: SEM micrographs of the photoactive hybrid layers; (a) rr-P3HT, (b) rr-P3HT: 0.3 wt % SiNWs, (c) rr-P3HT: 0.7 wt% SiNWs and (d) rr-P3HT: 1.3 wt% SiNWs.

4.3.2 Thicknesses of the hybrid films

The thickness of the photoactive layer and all other layers making up a SC is a very important factor to consider during SC fabrication. Figure 4.4 displays the dependence of the hybrid film thickness on the concentration of the solution of rr-P3HT and different weight percent ratio of SiNWs. It is noticeable from figure 4.4 (a) that the increasing concentration of SiNWs introduces spikes on the surface of the film. This confirms our earlier suggestion that a rough film results from incorporating high concentration of SiNWs. It is clear from figure 4.4 (b) that the thickness of the film increases with an increasing amount of SiNWs. This is in agreement with the results

obtained by Flack et al [4.29] who reported that the film thickness increases with increasing precursor solution. The solution with low concentration of SiNWs, i.e. P3HT:0.3 wt % SiNWs provided a thinner film probably due to massive material outflow as a result of reduced surface tension and low viscosity of the solution. The viscosity of the solution and thus its surface tension increased as the concentration of SiNWs was increased. In that regard, the thicknesses obtained from the solution concentrations of P3HT: 0.7 wt% SiNWs and P3HT: 1.3 wt % SiNWs were improved in terms of thickness due to reasonable and desired material outflow behaviour.

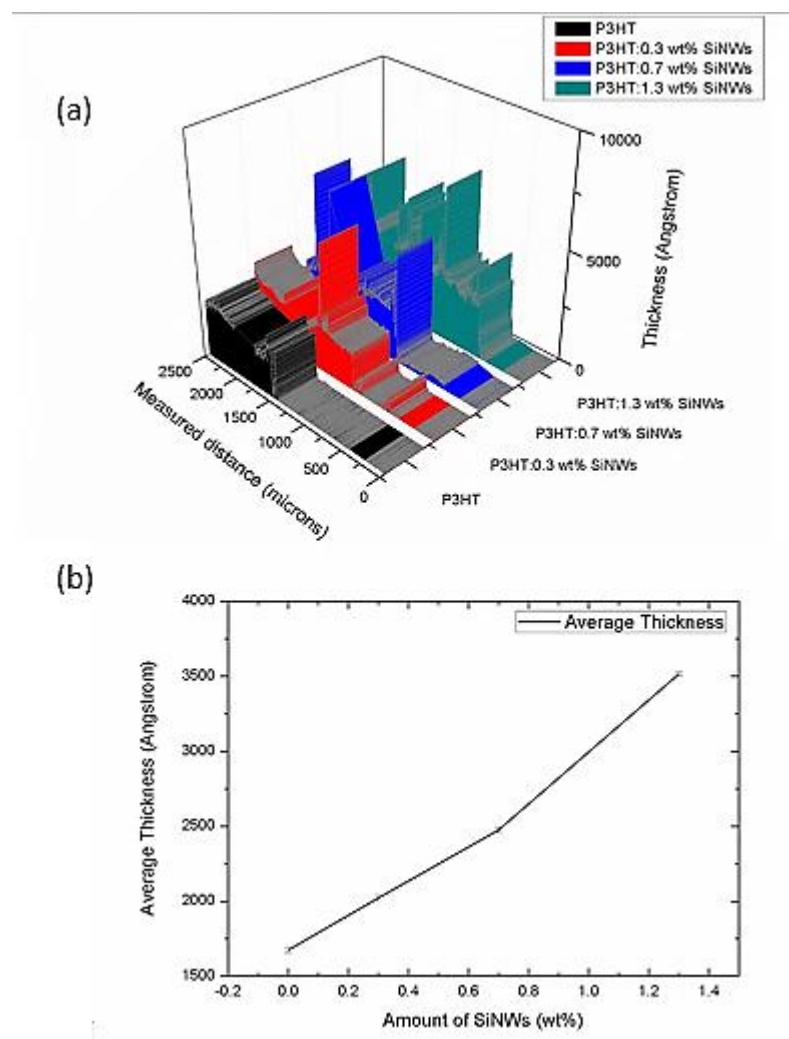


Figure 4.4: Dependence of thickness on the amount of SiNWs incorporated into the rr-P3HT matrix, (a) shows the thickness profiles whereas (b) shows the average thickness of the films.

4.3.3 Absorption properties

When molecules of a polymer absorb light of an appropriate wavelength, an electron can be promoted to a higher energy orbital. Ultraviolet and visible light have sufficient energy to cause this electronic transition. Here we will discuss the absorption spectrum of the rr-P3HT thin film and later compare it to rr-P3HT: SiNWs thin film absorption spectra of different weight percent ratios of SiNWs. Figure 4.5 shows a deconvoluted UV-vis absorption spectrum of rr-P3HT thin film on a glass substrate that was prepared from a solution concentration of 25 mg/ml in a binary solvent of DCB: CF (1:1). The spectrum was measured from 325 nm to 675 nm and it was deconvoluted into four Gaussian fits to clearly depict different contributions that could not have been observed from the clear spectrum. The UV-vis spectrum in figure 4.5 depicts four absorptions peaks centered at 388 nm, 522 nm, 562 nm and 607 nm respectively. These peaks are attributed to vibronic transitions (i.e. $\pi-\pi^*$) originating from the crystalline-phases [4.30, 4.31]. Javagatrup et.al observed an additional peak that they attributed to the amorphous phase, which was not observed in our case.

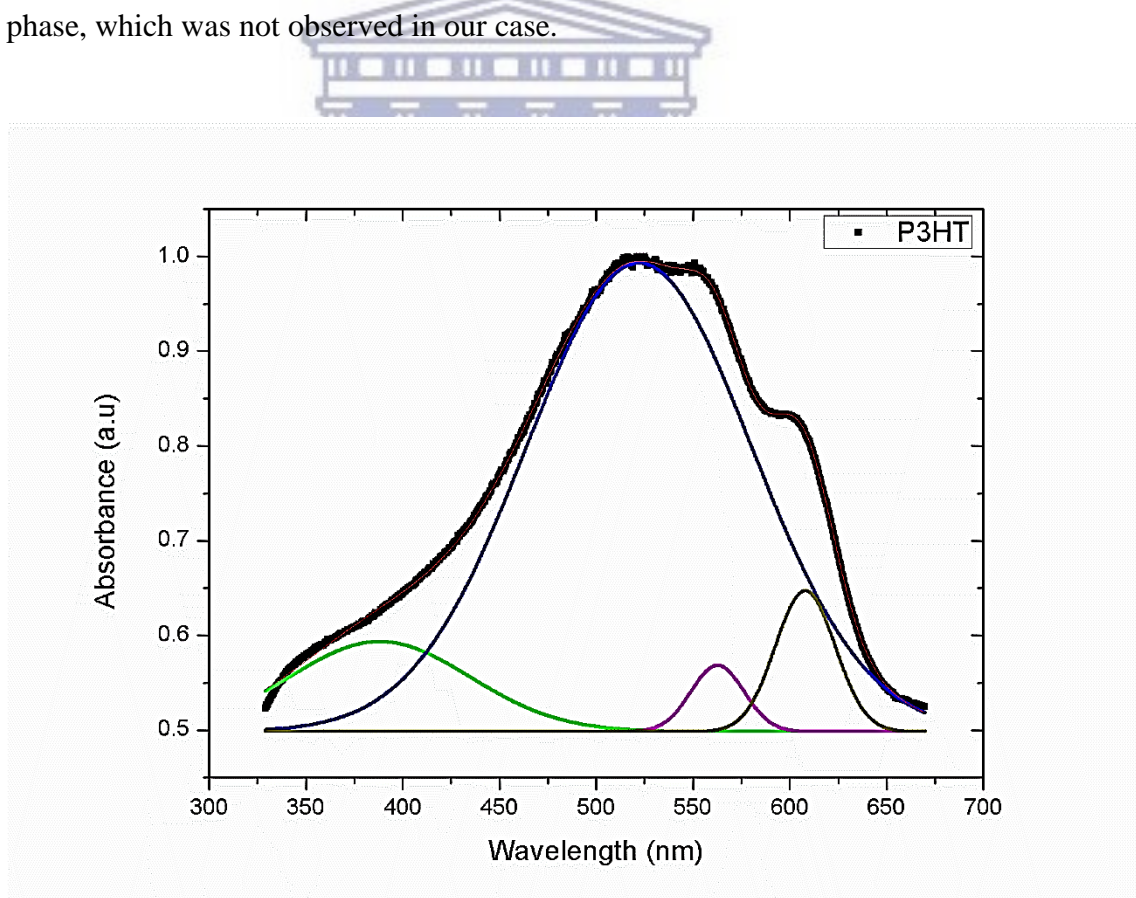


Figure 4. 5: Gaussian deconvoluted UV-Vis absorption spectrum of rr-P3HT thin film.

In order to demonstrate the effect of SiNWs on the active layers of the devices, we compared light absorption spectra of rr-P3HT and rr-P3HT: SiNWs of different blend ratios as shown in figure 4.6. It was noticeable from the spectra that the shape of the absorption spectrum of rr-P3HT thin film is retained upon addition of SiNWs with an increase in the absorption intensity. This proves that there is an interaction between rr-P3HT molecules and SiNWs, and suggests better structuring of rr-P3HT domains in the presence of SiNWs. The highest absorption peak is observed for rr-P3HT: 0.7 wt % SiNWs and as is observed in the case of rr-P3HT: 1.3 wt% SiNWs solution, further addition of SiNWs compromises the absorption spectrum even though it is still higher in terms of absorption intensity than that of pure rr-P3HT. These results are in contradiction with the work of Braik et.al who employed the same materials and observed that there is a quenching of the absorption peak of rr-P3HT upon SiNW incorporation [4.27].

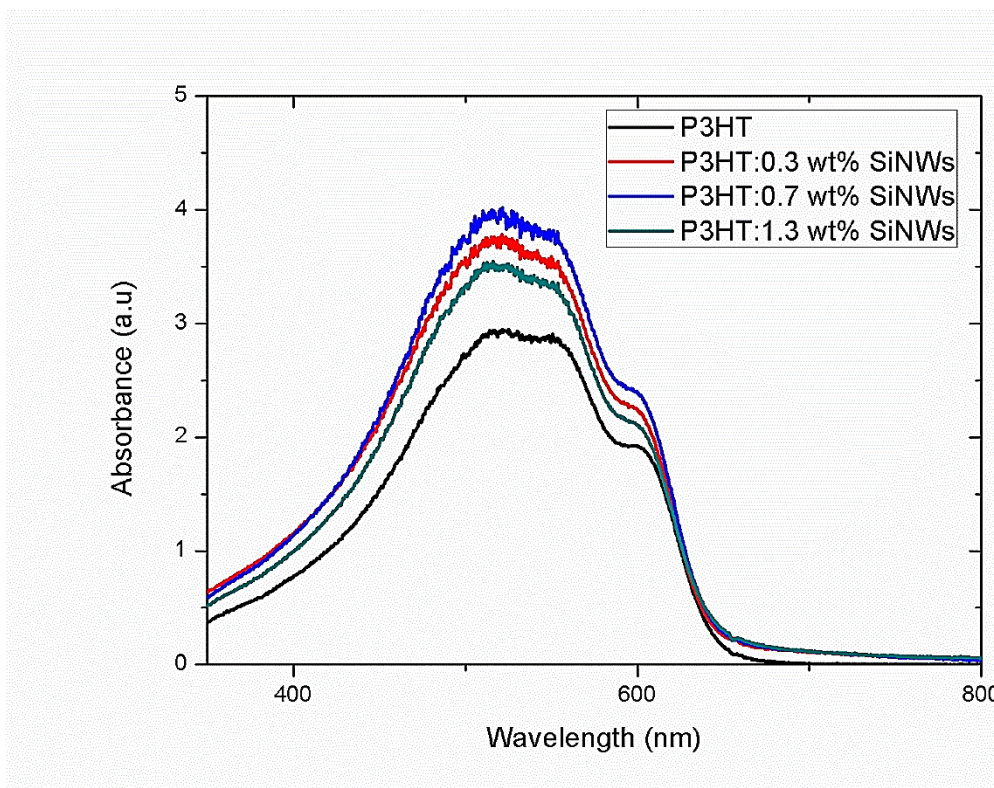


Figure 4. 6: UV-vis absorption spectra of thin films of rr-P3HT and rr-P3HT: SiNWs with different SiNWs weight percent ratios.

4.3.4 Emission properties

PL is a technique that is used to examine the energy level of a material to help us understand the electronic properties and impurity levels of that particular material. It is a

process by which a material absorbs light of appropriate wavelength and re-radiates it through various mechanisms. Again, we discuss the emission spectrum of the rr-P3HT thin film first and compare it to emission spectra of different hybrid films. Figure 4.7 shows the PL emission spectrum of the photon excited rr-P3HT film. The spectrum is deconvoluted into two emission peaks by a Gaussian fitting procedure to obtain the electronic states in the photo-excited rr-P3HT film. The PL spectrum exhibits two emission peaks that are resolved at 643 nm and 688 nm. The PL emission peak situated at 643 nm is attributed to a pure electronic transition from the LUMO to the HOMO whereas the peak at 688 nm is assigned to the first vibronic band [4.32].

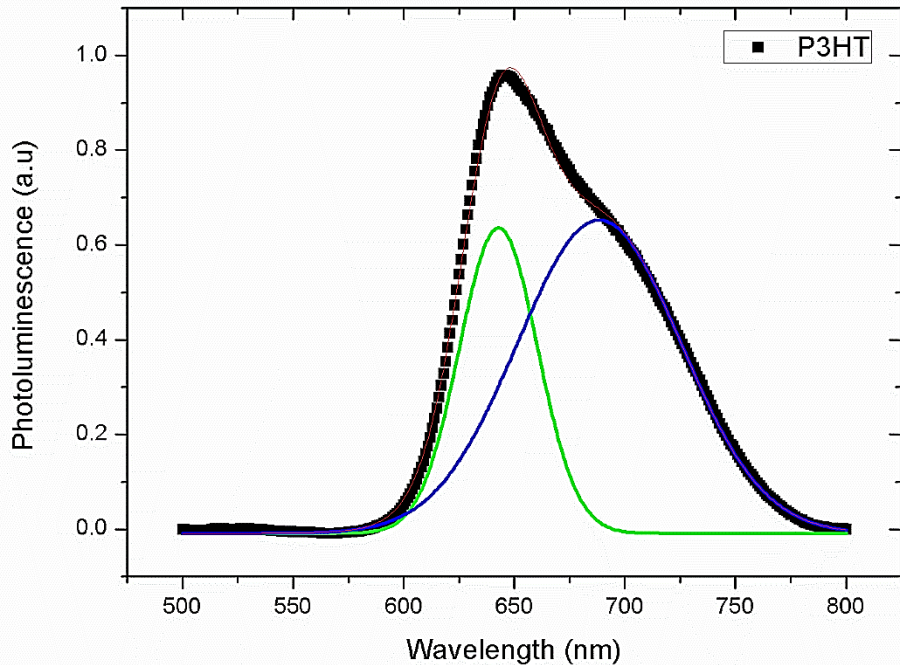


Figure 4. 7: Gaussian deconvoluted photoluminescence emission spectrum of rr-P3HT thin films.

PL spectra of rr-P3HT: SiNWs hybrid films of different concentration of SiNWs (i.e. 0.3 wt%, 0.7 wt% and 1.3 wt%) were collected to examine the effect of SiNWs on the photon emission property of rr-P3HT thin film. Figure 4.8 shows the comparison of the PL. It is evident from the figure 4.8 that the emission peak of rr-P3HT located between 600 and 800 nm is gradually quenched by adding SiNWs. The maximum quenching (i.e. lowest emission peak intensity) is observed for rr-P3HT: 0.7 wt% SiNWs. This is an indication of favourable charge separation at the D-A interface. Further addition of SiNWs into the polymer matrix, i.e. rr-P3HT: 1.3 wt % SiNWs results in a red shift and

an increase in emission intensity of the PL peak. The increase in the emission intensity and a redshift observed may be due to the formation of SiNWs aggregates, which decreases the D-A interfaces [4.28, 4.33]. These emission properties of rr-P3HT: SiNWs of different concentration do not contradict the literature, however there are features like the broadening of spectra upon addition of SiNWs which have not been reported before. This may be attributed to the photon absorption that could be associated with SiNWs.

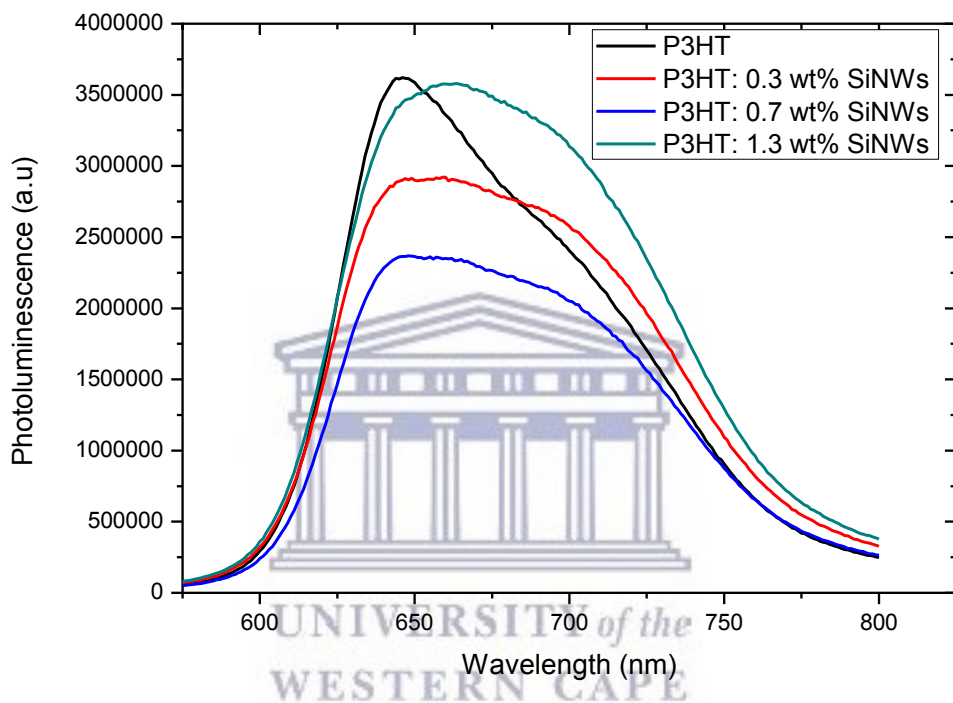


Figure 4. 8: Photoluminescence emission spectra of thin films of rr-P3HT and rr-P3HT: SiNWs with different SiNWs weight percent ratios.

4.3.5 High Resolution TEM analysis

HR-TEM was used to further examine the details of the ordering of rr-P3HT layer and the interaction of rr-P3HT: SiNWs in the D-A interface. The TEM and HR-TEM samples were prepared by drop-casting the solutions on the holey-carbon copper grid and we assume that the observations would be the same for thin films. The degree of crystallinity in high molecular weight of pure rr-P3HT depends on the processing conditions and has been determined to be in the range of 4-18% [4.34]. In that regard, rr-P3HT thin films fabricated under different conditions including post thermal treatment could exhibit different degrees of crystallinity. The rr-P3HT thin film as

depicted in figure 4.9 consists of some crystalline domains orientated with respect to the incident electron beam (circled regions) and featureless zones. The crystalline domains are ascribed to periodic fringe patterns corresponding to regular π stacked chains with characteristic lamellar period, while the non-crystalline areas could be amorphous zones or rr-P3HT periodic lamellar patterns whose orientation relative to the electron beam prevent their observations [4.35]. The inset in figure 4.9 displays the SAED of the rr-P3HT thin film which depicts low crystallinity. Quite a number of d-spacings could be observed, however only two crystalline domains possessing d-spacings of 0.38 and 0.18 nm could be indexed and were found to correspond to (010) and (020) reflections, respectively. This is in contradiction with previous studies in literature such as those done by Motaung et.al in which they revealed that rr-P3HT structure shows the (100), (200), (300) and (010) reflections with corresponding d spacing's of 1.73, 0.83, 0.52 and 0.37 nm respectively [4.36-4.37]. This discrepancy could have arisen due to different film deposition methods which may have caused different orientation of polymer backbone and side chains with respect to the substrate in their case, or it could be evidence of impurities in our thin films. This necessitated us to perform EDS analysis in order identify the elemental composition of our thin films and also examine the level of impurities if present.

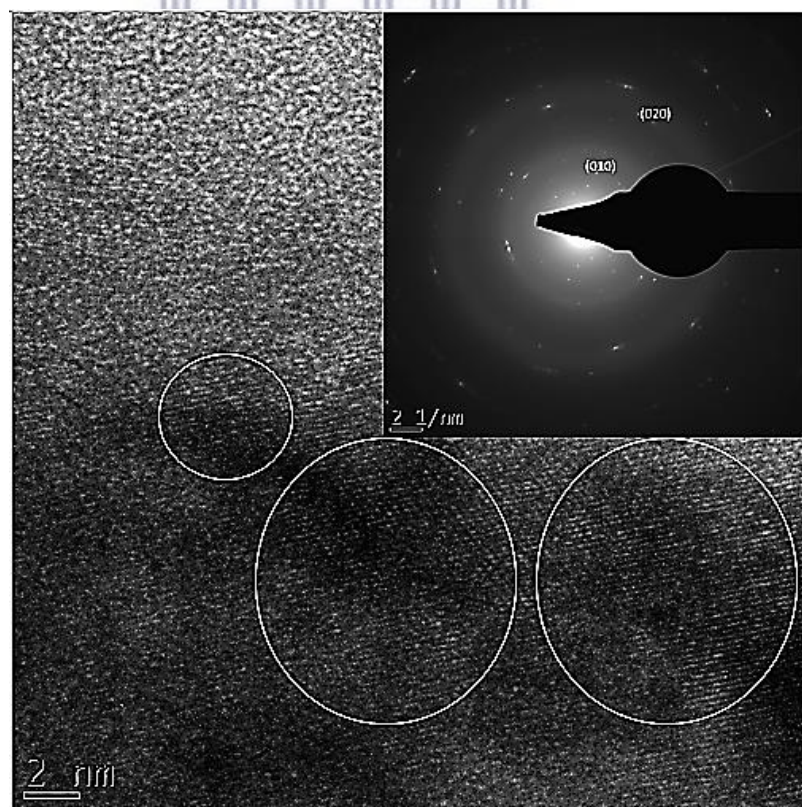


Figure 4. 9: HR-TEM micrograph of rr-P3HT thin film. The inset displays the SAED pattern of the rr-P3HT.

Figure 4.10 depicts the EDS spectrum which demonstrates a predominant signal of C and S which correspond to elements comprising rr-P3HT since it has a chemical formula of $[C_{10}H_{14}S]$. Within the polymer, S atoms are located in a stack of polythiophene backbones while C and H atoms are found in the alkyl side chains [4.35]. In addition, weak O and Cu signals are evident in the EDS spectrum. The Cu signals are detected due to the holey-carbon copper grid that was employed as back supporting substrate during TEM measurement. In our belief, the O signal is attributed to oxidation of the sample surface prior the insertion into the microscope since all sample preparation are done in ambient condition. This EDS spectrum confirms that our films are impurities-free which leave us with only one explanation for ring patterns that could not be indexed, i.e. they originate from the polymer stacking on the glass substrate that is different from that obtained by other researchers. This EDS spectrum is in accordance with the results observed by Abdellah et.al [4.38].

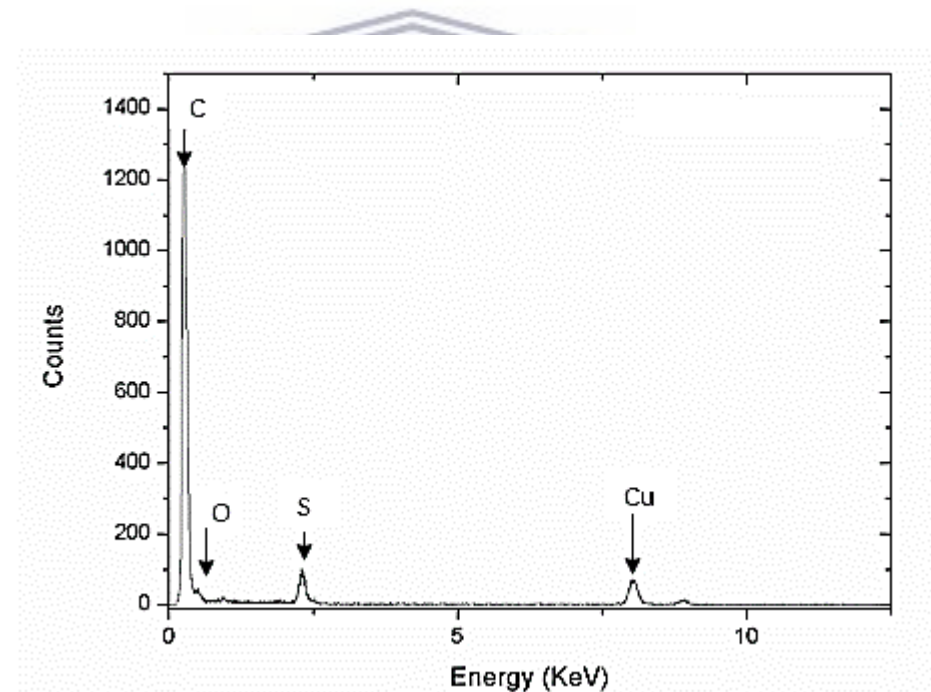


Figure 4. 10: EDS spectrum of the rr-P3HT film.

The TEM micrograph in figure 4.11 (a) shows that within the matrix, rr-P3HT cover parts of the SiNWs. The HR-TEM micrograph in figure 4.11 (b) indicates that the hybrid film consist of some crystalline domains orientated with respect to the incident electron beam (circled regions in figure 4.11 (b)) and featureless zones. The crystalline domains could be ascribed to both rr-P3HT and SiNWs, and the amorphous domain

only to rr-P3HT. As is evident from figure 4.11 (b), the clearly pronounced single crystallinity of SiNWs observed in chapter 3 (figure 3.15 (b)) has been tempered upon mixing them with the polymer. However, this required further investigation which was performed by SAED of the hybrid films.

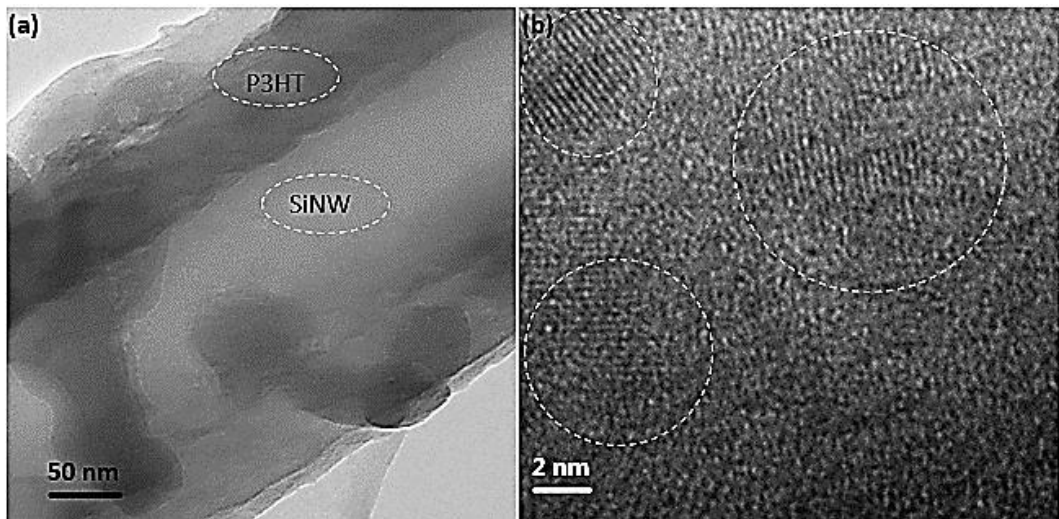


Figure 4. 11: TEM images, (a) SiNWs covered by rr-P3HT and (b) crystallographic information on rr-P3HT: 1.3 wt% SiNWs.

Figure 4.12 shows the SAED pattern of the rr-P3HT: 1.3 wt% SiNWs hybrid film. This depicts a feature that is a combination of both SiNWs and rr-P3HT SAED patterns obtained earlier (i.e. clearly visible spot patterns and fading ring patterns from the SiNWs and rr-P3HT, respectively), as indexed in figure 4.12 (b). It is quite remarkable to observe that the SAED pattern of the hybrid is just the superposition of SAED patterns of the SiNWs and rr-P3HT. This provides a confirmation that there is no chemical interaction between the SiNWs and rr-P3HT, but rather a physical interaction since the polymer attached to the walls of the SiNWs.

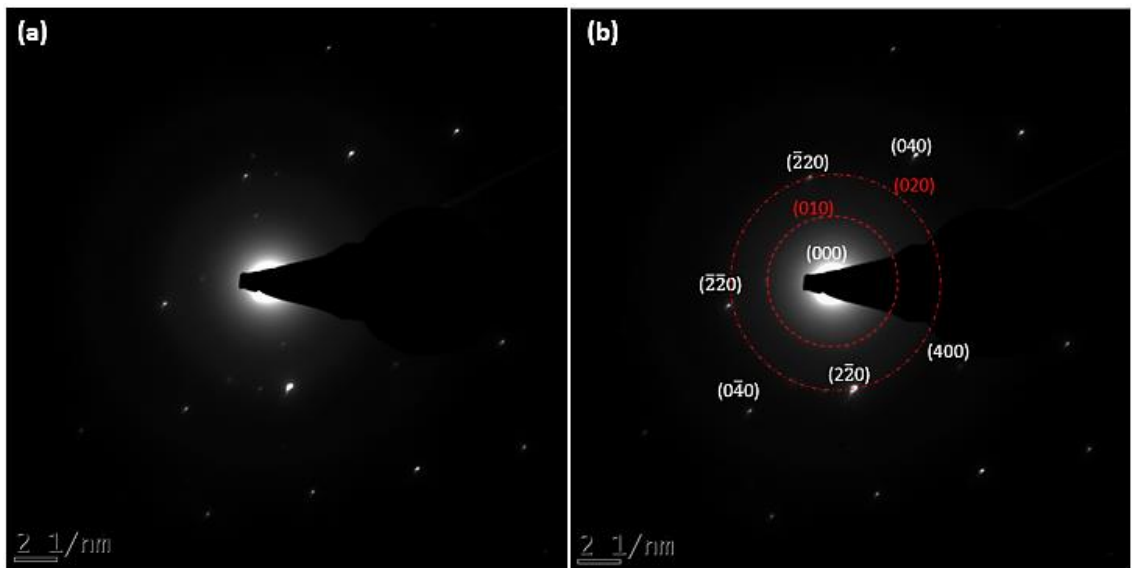


Figure 4. 12: The SAED pattern for the combination of rr-P3HT: 1.3 wt % SiNWs, (a) is the unindexed pattern which serve as a reference and (b) is the indexed pattern.

4.3.6 Electric properties and current density-voltage characteristics (J-V curves).

Electrical transport through disordered materials is a large and complex field. At this stage the information that has been gathered through different experiments about the as-synthesised SiNWs, rr-P3HT thin film and hybrid films will better equip us to understand the electrical properties associated with these materials. In this work the electrical conductivity study is discussed based on the expression:

$$\sigma = ne\mu, \quad (4.1)$$

where σ is the conductivity, n is the electron concentration, e is the electron charge and μ is the carrier mobility [4.39].

In the present work the electric properties of rr-P3HT: SiNWs thin films of different SiNWs weight ratios have been investigated to determine the relationship between the conductivity and SiNWs content. The thickness and conductivity of the hybrid films measured at room temperature using a Dektak Profilometer and four point probe Hall Effect measurement system are presented in table 4.1. As mentioned before, the thickness of the hybrid films increase with an increasing content of SiNWs which was attributed to the enhanced surface tension of the solutions with an increasing content of SiNWs. In addition, table 4.1 also reveals that adding SiNWs into the rr-P3HT matrix

increases the electrical conductivity, and the maximum conductivity is obtained from the rr-P3HT:1.3 wt% SiNWs thin film. The current that was passed through different samples (i.e. rr-P3HT, rr-P3HT: 0.3 wt% SiNWs, rr-P3HT: 0.6 wt% SiNWs and rr-P3HT: wt% SiNWs) films was 0.9 nA. This means that the electron concentration (n) passing in all the samples was fixed. Therefore an increase in conductivity upon the addition of SiNWs in the rr-P3HT matrix can be related to an increase of the mobility (μ) of charge carriers in the hybrid films. This means that SiNWs provide electric pathways for the charge carriers, which increases the conductivity as the concentration of wires increases. The low conductivity of the film deposited from pure rr-P3HT solution is no surprise since the film does not contain SiNWs which are deemed to be favourable for electron conduction. These results are in correspondence with those obtained by Kuila et.al, who reported a conductivity of the same order (i.e. $\sim 10^{-5} \Omega^{-1}\text{cm}^{-1}$) for the undoped rr-P3HT films [4.40].

Table 4. 1: Thickness and conductivity of spin coated films.

P3HT: SiNWs wt % ratio	Thickness (nm)	Conductivity ($\times 10^{-5} \Omega^{-1}\text{cm}^{-1}$)
P3HT	168	0.9
P3HT: 0.3 wt % SiNWs	202	1.2
P3HT: 0.7 wt % SiNWs	247	1.4
P3HT: 1.3 wt % SiNWs	351	3.4

Having considered the area of each SC which was 0.0256 cm^2 , the I-V characteristics of the rr-P3HT: SiNWs with different concentration of SiNWs measured in dark and under simulated AM 1.5 illumination with the intensity of 100 mW/cm^2 , are plotted using current density as depicted in figure 4.13. The PV parameters are summarised in table 4.2. Here, R_s and R_{sh} are series and shunt resistances, respectively, while other PV parameter symbols have their previous meanings. The amount of SiNWs within the rr-P3HT matrix is directly correlated with the observed variation in PV parameters.

The baseline efficiency of 0.0007 % was calculated for the least concentration of SiNWs (i.e. rr-P3HT: 0.3 % SiNWs). By increasing the concentration of SiNWs incorporated into rr-P3HT matrix (rr-P3HT: 0.7 % SiNWs), the V_{oc} and the J_{sc} increased while the R_s decreased which subsequently resulted in an increased efficiency of 0.0009 %. The enhancement of V_{oc} and the J_{sc} can be attributed to a good energetic relationship

between the rr-P3HT and SiNWs, and an increase in photon absorbance upon addition of SiNWs, respectively. Improved absorption of light will introduce more photo-generated carriers and lead to an improved J_{sc} . In SC fabrication, the R_s is required to be at its minimum to avoid efficiency loses due to increased charge carrier recombination. Therefore, the minimum R_s obtained for the P3HT: 0.7 wt% SiNWs signifies good energy level alignment between the materials used and reduced bulk resistance within the layer. This is in accordance with the maximum PL quenching observed in figure 4.8 for this nanocomposite weight ratio.

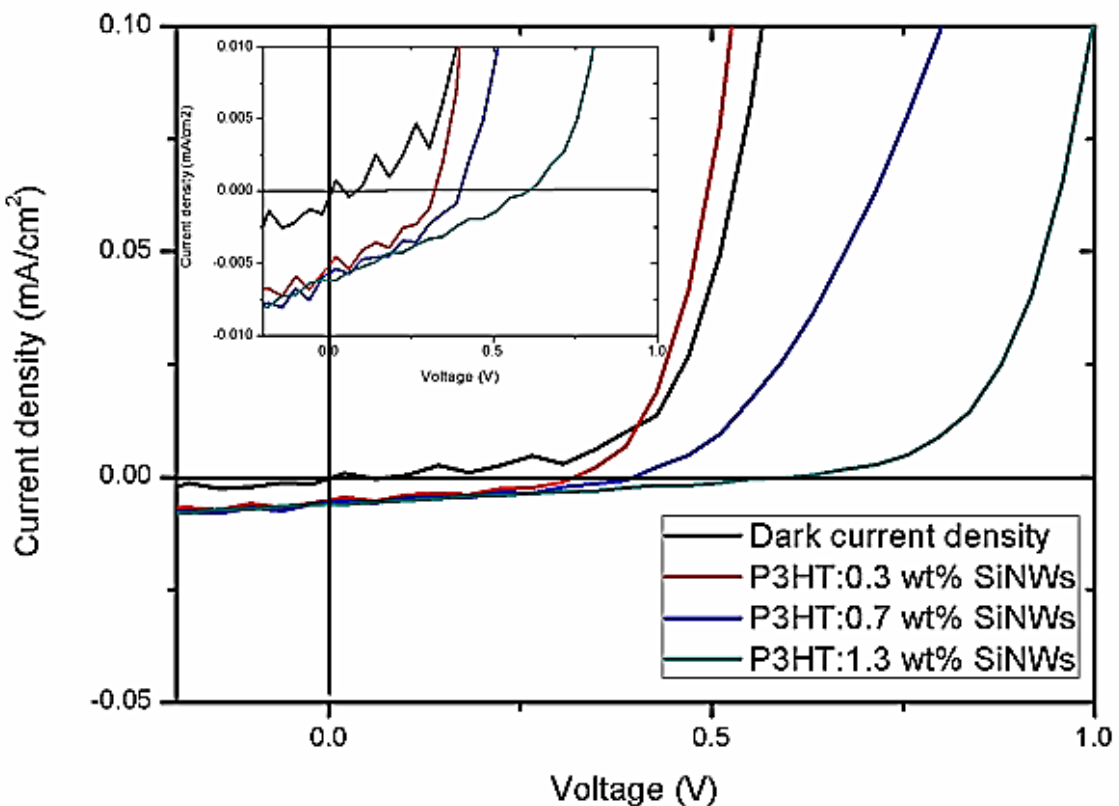


Figure 4. 13: J-V characteristics of ITO/PEDOT:PSS/rr-P3HT:SiNWs/Al devices with different weight ratios of SiNWs measure in dark and under light illumination, the inset is the zoomed-up J-V curve close to the origin.

Further addition of SiNWs into rr-P3HT matrix (i.e. rr-P3HT: 1.3 wt% SiNWs) leads to the maximum efficiency of 0.0011 %. This improved efficiency is as a result of the improvements in the V_{oc} , J_{sc} and the R_{sh} . The enhancement of the V_{oc} can be related to the fact that more SiNWs are now present in the active layer to extract electrons from rr-P3HT, which reduces charge carrier losses. The rapid increase in R_{sh} for this blend ratio validates the existence of different current paths within the active layer and confirms the reduced current leakage through the PV cell. This means that more electrons reach the

cathode electrode (Al). These J-V characteristic results are in agreement with the Hall effects results where it was observed that progressive incorporation of SiNWs into the rr-P3HT matrix constructively influence the electrical properties of the hybrid films. Moreover, these results are comparable with those obtained by Dkhil et.al and Chehata et.al in the sense that the PCE of the SCs increased upon addition of SiNWs [4.28, 4.6].

Table 4.2: Photovoltaic parameters of ITO/PEDOT:PSS/rr-P3HT:SiNWs/Al devices with different weight ratios of SiNWs.

P3HT: SiNWs	V _{oc} (V)	J _{sc} (mA/cm ²)	R _s (Ωcm ²)	R _{sh} (Ωcm ²)	PCE (%)
0.3 wt% SiNWs	0.31	0.0057	76623	73766	0.0007
0.7 wt% SiNWs	0.39	0.0060	35722	67502	0.0009
1.3 wt% SiNWs	0.59	0.0061	60292	165413	0.0011

Another parameter of the PV devices that reveals important information is the FF. For rr-P3HT: SiNWs SCs the FF reduced from 0.42 for rr-P3HT: 0.3 wt% SiNWs to 0.30 for rr-P3HT: 1.3 wt% SiNWs. We speculate that even though the highest weight ratio of SiNWs provide the highest efficiency compared to other rr-P3HT: SiNWs cells, it is not the best performing SC. In essence, only a fraction of the large number of initial photo-induced charge carriers reach the electrodes. This is in correspondence with the PL results where we observed that the rr-P3HT: 1.3 wt% SiNWs thin film resulted in the highest emission peak which suggested maximum charge recombination.

It is very noticeable from figure 4.13 and table 4.2 that the ITO/PEDOT:PSS/rr-P3HT:SiNWs/Al SCs exhibit very low PCEs. The absorption spectra in figure 4.6 confirmed that the rr-P3HT in the hybrid film absorbs photons and create excitons. However, the incomplete quenching of the rr-P3HT emission peak upon addition of SiNWs in the PL spectra, i.e. figure 4.8 suggested that the amount of SiNWs is not enough for effective electron dissociation and transportation. This necessitated the addition of the same amount of PCBM in our solutions to boost the electron accepting ability of the SiNWs in particular, and the SCs in general. The new solutions were composed of 12.5 mg of rr-P3HT, 7.5 mg of PCBM and different amounts of SiNWs (i.e. 0.156 mg, 0.313 mg and 0.625 mg) in a (1:1) binary solvent of DCB and CF. A ITO/PEDOT:PSS/rr-P3HT:PCBM/Al SC (without SiNWs) was fabricated as well for reference purpose. Figure 4.14 show the current density-voltage characteristic of the

ITO/PEDOT:PSS/rr-P3HT:PCBM:SiNWs/Al devices with different amount of SiNWs in the dark and under illumination. In addition, table 4.3 summarises the PV parameters that were obtained.

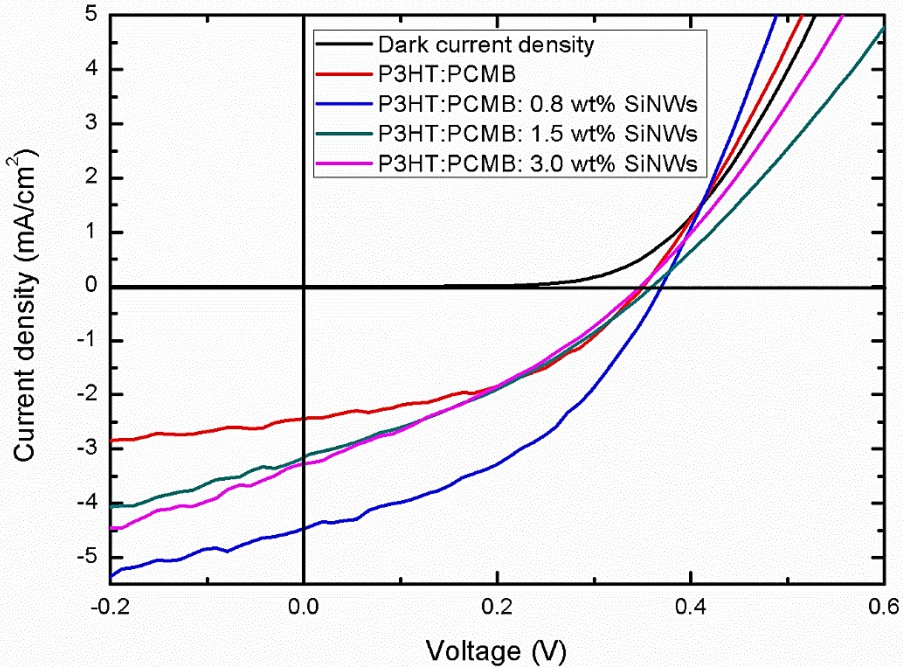


Figure 4. 14: J-V characteristics of ITO/PEDOT:PSS/rr-P3HT:PCBM:SiNWs/Al devices with different weight ratios of SiNWs measure in dark and under light illumination.

The baseline efficiency of 0.38 % was calculated for the rr-P3HT: PCBM SC. Upon addition of SiNWs (i.e. rr-P3HT:PCBM: 0.8 wt% SiNWs) the Voc and the Jsc increased from 0.35 V and 2.45 mA/cm² to 0.37 V and 4.51 mA/cm², respectively, while the R_s decreased from 606 Ω/cm² to 88 Ω/cm². These enhancements resulted in the largest efficiency of 0.68 %. The increase in the V_{oc} could be attributed to the favourable energy levels alignments between the rr-P3HT:PCBM and SiNWs for this specific composition. A sharp increase in the J_{sc} and a rapid decrease in the R_s could be attributed to the improved charge generation, transport and extraction within the SC. In the presence of PCBM, increasing the amount of SiNWs (i.e. rr-P3HT:PCBM: 1.5 wt% SiNWs and rr-P3HT:PCBM: 3.0 wt% SiNWs) deteriorated the performance of the SCs and resulted in reduced efficiencies of 0.38 % and 0.37 % respectively. This is as a result of low R_{sh} in both cases which suggest current leakage within the SCs.

Table 4.3: Photovoltaic parameters of ITO/PEDOT:PSS/rr-P3HT:PCBM:SiNWs/Al devices with different weight ratios of SiNWs.

Blend: SiNWs	V _{oc} (V)	J _{sc} (mA/cm ²)	R _s (Ωcm ²)	R _{sh} (Ωcm ²)	PCE (%)
P3HT: PCBM	0.35	2.45	606	428	0.38
0.8 wt% SiNWs	0.37	4.51	88	215	0.68
1.5 wt% SiNWs	0.36	3.20	347	193	0.38
3.0 wt% SiNWs	0.35	3.29	1343	156	0.37

For rr-P3HT:PCBM: SiNWs SCs, the FF reduced from 0.45 for rr-P3HT:PCBM to 0.32 for P3HT:PCBM: 3.0 wt% SiNWs. These results are consisted with those obtained by Huang et.al [4.41], they obtained a PCE of 1.9 % and their results clearly indicated that an incorporation of SiNWs into polymer SCs can be used to obtain high J_{sc} and efficiencies by improving the optical properties, dissociation of excitons and electron transport.

4.4 Conclusion

In conclusion, BHJ photoactive hybrid films composed of rr-P3HT, PCBM and SiNWs have been prepared by spin coating to establish optimal composition of these materials of interest. Within the photoactive hybrid layer, SiNWs are randomly distributed and the polymer covers SiNWs, thus forming various D-A interfaces essential for charge separation. The TEM results show that there is no chemical interaction between rr-P3HT and SiNWs which is why the rr-P3HT material only covers the surface of SiNWs. The conductivity and the PCE of the hybrid films increased upon addition of SiNWs. The maximum conductivity and PCE of $3.61 \times 10^{-5} \Omega^{-1} \cdot \text{cm}^{-1}$ and 0.0011 %, were respectively obtained for the blend ratio of rr-P3HT: 1.3 wt % SiNWs. However, upon addition of PCBM the maximum PCE of 0.68 % was realised for the blended ratio of rr-P3HT: PCBM: 0.8 wt% SiNWs. There is good correspondence between the optical and the electrical properties of the as-prepared hybrid films (i.e. rr-P3HT: SiNWs). Moreover, with the highest PCE obtained from the cell containing wires, we can confidently pronounce that an optimised amount of SiNWs can indeed improve the performance of low-PCE organic solar SCs by more than 56%.

Reference

- [4.1] Krebs F C 2009 *Solar Energy Materials and Solar Cells* **93** 394
- [4.2] Yue D, Khatau P , You F and Darling S B 2012 *Energy & Environmental Science* **5** 9163
- [4.3] McCullough R D 1998 *Advanced Materials* **10** 93
- [4.4] McCullough R D and Lowe R D 1992 *Journal of the Chemical Society, Chemical Communications* **1** 70
- [4.5] Kline R J, McGehee M D, Kadnikova E N, Liu J, Fréchet J M J and Toney M F 2005 *Macromolecules* **38** 3312
- [4.6] Muller T, Ramashia T A, Motaung D E, Cummings F, Malgas G, Oliphant C and Arendse C 2016 *Physica Status Solidi A* **213** 1915
- [4.7] Hoppe H and Sariciftci S N 2004 *Journal of Materials Research* **19** 1924
- [4.8] Azizi S, Braik M, Dridi C, Ouada H B, Ryback A and Davenas J 2012 *Applied Physics A* **108** 99
- [4.9] Chehata N, Ltaief A, Beyou E, Ilahi B, Salem B, Baron T, Gentile P, Maaref H and Bouazizi A 2015 *Journal of Luminescence* **168** 315
- [4.10] He L, Jiang C, Wang H, Lai D, Tan Y H, Tan C S and Rusli 2012 *Applied Physics Letters* **100** 103104
- [4.11] Charrier J, Najar A and Pirasteh P 2013 *Applied Surface Science* **283** 828
- [4.12] Bao Z, Dodabalapur A, Lovinger A J 1996 *Applied Physics Letters* **69** 4108
- [4.13] Yang H, Shin T J, Yang L, Cho K, Ryu C Y and Bao Z 2005 *Advanced Functional Materials* **15** 671
- [4.14] Emslie A G, Bonner F T and Peck L G 1958 *Journals of Applied Physics* **29** 858
- [4.15] Norrman K, Ghanbari-Siahkali A and Larsen N B 2005 *Annual Report on the Progress of Chemistry, Section C* **101** 174
- [4.16] Lawrence C J 1988 *Physics of Fluids* **31** 2786
- [4.17] Scriven L E 1988 *Material Science Society* **121** 717
- [4.18] Tyona M D 2013 *Advances in Material Research* **2** 181
- [4.19] Scriven L E 1988 *Material Research Society, Symposium Proceeding* **121** 717
- [4.20] Tyona M D 2013 *Advances in Material Research* **2** 195
- [4.21] Sahu N, Parija B and Panigrahi S 2009 *Indian Journals of Physics* **83** 493

- [4.22] Hanaor D A H, Triani G, Sorrell C C 2011 *Surface and Coating technology* **205** 3658
- [4.23] Lin D D, Wu H and Pan W 2007 *Advanced Materials* **19** 3968
- [4.24] Meyerhofer D 1978 *Journals of Applied Physics* **49** 3993
- [4.25] Taylor J F 2001 *Metal Finishing* **19** 16
- [4.26] Luo S C, Cranium V and Douglas E P 2005 *Langmuir* **21** 2881
- [4.27] Braik M, Dridi C, Rybuk A, Davenas J and Cornu D 2014 *Physica Status Solidi A* **211** 670
- [4.28] Dkhil S B, Elbdelli R, Dachraoui W, Faltakh H, Bourguiga R and Davenas J 2014 *Synthetic Metals* **192** 74
- [4.29] Flack W W, Soang D S, Bell A T and Hess D W 1984 *Journal of Applied Physics* **56** 1199
- [4.30] Clark J, Silva C, Friend R H and Spano F C 2007 *Physical Review Letters* **98** 206406
- [4.31] Savagatrup S, Printz A D, O'Connor T F, Zaretski A V, Rodriguez D, Sawyer E J, Rajan, K M, Acosta R I, Root S E and Lipomi D J 2015 *Energy & Environmental Science* **8** 55.
- [4.32] Sharma M, Kaushik D, Singh R R and Pandey R K 2006 *Journal of Materials Science: Materials in Electronics* **17** 537.
- [4.33] Sperling, L. (2006). Chain structure and configuration, *Introduction to physical polymer science*. Hoboken, New Jersey: Wiley, pp 29-65.
- [4.34] Drummy L F, Davis R J, Moore D L, Durstock M, Vaia R A and Hsu J W P 2011 *Chemistry of Materials* **23** 907
- [4.35] Salammal S T, Mikayelyan E, Grigorian S and Pietsch U 2012 *Macromolecules* **45** 5575
- [4.36] Motaung D E, Malgas G F and Arendse C J 2010 *Journals of Material Science* **45** 3276
- [4.37] Mardalen J and Emil J S 1992 *Synthetic Metals* **48** 363
- [4.38] Abdellah A, Virdi K S, Meier R, Doblinger M, Muller-Baschbaum P, Scheu C, Lugli P and Scarpa G 2012 *Advanced Functional Materials* **22** 4078
- [4.39] Kasap, S. and Capper, P. (2007). Electrical Conduction in Metals and Semiconductors, *Springer handbook of electronic and photonic materials*. Boston, MA: Springer Science+Business Media, Inc. pp19-46.
- [4.40] Kuila B K and Nandi A K 2004 *Macromolecules* **37** 8577

[4.41] Huang J S, Hsiao C Y, Syu S J, Chao J J and Lin C F 2009 *Solar Energy Materials & Solar Cells* **93** 621



5 SUMMARY AND RECOMMENDATIONS

The aim of the study was to optimise the weight ratio of rr-P3HT: SiNWs and fabricate BHJ hybrid SCs with rr-P3HT: SiNWs as a photoactive layer. Hybrid SCs combine advantages of both organic and inorganic materials. In this study the rr-P3HT absorbed light and acted as the electron D, whereas the SiNWs acted as an electron A and transporter in the structure. The polymer (rr-P3HT) was employed for its good optical absorption and hole transporting ability arising from the crystalline ordering, whereas SiNWs offered high surface area per volume ratio providing a large interface for exciton dissociation, therefore leading to high mobility of electrons. The rr-P3HT was purchased from Sigma Aldrich and it was used without any modification or purification whereas SiNWs were synthesised via MACE.

The first step of MACE is the deposition of AgNPs on a pre-cleaned Si wafer. This was obtained by immersion of pre-cleaned Si wafer into the HF/AgNO₃/H₂O solution. The as-deposited AgNPs are spherical shaped and are randomly deposited throughout the wafer. This is a very important step of MACE because it initialise the SiNWs formation and also controls the morphology, particularly the size of the resulting SiNWs. The average diameter of the AgNPs was found to be 288 ± 5 nm. The EDS results suggest that particles are mainly pure Ag, however some O imprints could be realised which suggested the oxidation of the sample surface since AgNPs deposition was done in ambient conditions.

The second step was the formation of SiNWs by immersion of AgNP-coated Si wafer into the aqueous solution of HF/H₂O₂/H₂O for 10 min and 20 min. The SiNWs

obtained from the immersion of AgNP-coated sample into the etching solution I for 20 minutes were longer ($\sim 4.5 \mu\text{m}$) than the ones obtained from 10 minutes ($\sim 1.1 \mu\text{m}$). This confirmed that the length of SiNWs depended on the etching duration. The average diameter of obtained SiNWs was $\sim 226 \pm 4 \text{ nm}$ and the EDS spectrum depicted some trace of O. In order to obtain SiNWs with smaller diameters, we suggest that the size of the AgNPs should be reduced by either reducing the immersion duration of Si wafer into HF/AgNO₃/H₂O solution or using another AgNPs deposition technique that could be highly controlled.

The third step was the etching of the bases of as-synthesised SiNWs in order to be able detached them from the wafer so we could assemble them with the polymer. This was realised by immersing the wafers consisting of vertically aligned SiNWs and AgNPs at the bottom in the etching solution II for different time (i.e. 2, 4, 6 and 8 minutes). The bases of vertically aligned SiNWs were etched horizontally for all four different durations which suggested that AgNPs start to oxidise and sink into the bases of SiNWs resulting into SiNWs with fragile bases. It was observed that the degree of the horizontal etching increases with time. After careful analysis of the wafers where SiNWs were synthesised and the SiNWs which were deposited on glass substrates, the 6 minutes etching in solution II was deemed the optimum condition. Therefore, the SiNWs that were assembled with rr-P3HT were detached as such.

TEM characterisation show that the core of SiNWs is cSi while the edges consist of an amorphous layer i.e. SiO₂ which confirms the suggestion made earlier about the oxidation of the SiNWs surfaces that could have occurred during or after the etching process since sample preparation were done in ambient conditions. In order to find the origin of the O imprints, we suggest that the exposure of sample in the atmosphere should be minimised by preparing the wires under the glove box. If the percentage of this O imprints do not decrease significantly, this would mean that most of the oxidation of the surface of wires occurs inside the solution during the SiNWs formation. The SAED pattern of the core of SiNWs show spot patterns which suggest that the single crystallinity of Si is not destroyed during the etching. According to the HR-TEM micrograph an interplanar spacing (d-spacing) of 0.129 nm corresponds to an axial orientation of [001].

The absorption and emission properties of SiNWs were investigated as well because these wires were going to be used for SC photoactive layer. The absorption and the emission properties of SiNWs were investigated so as to be able to recognise their contributions in the absorption and emission spectra of the hybrid films, respectively. The absorption spectrum of SiNWs exhibited more absorption intensity between 345 nm and 641 nm wavelengths which can reach the maximum of 57%, whereas the emission spectrum exhibited the broad and roughly symmetric PL peak observed between 710-730 nm.

Following the synthesis and detachment study of SiNWs, four solutions were prepared using a (1:1) binary solvent ratio of DCB and CF. The solutions were as follows; rr-P3HT, rr-P3HT: 0.3 wt% SiNWs, rr-P3HT: 0.7 wt% SiNWs and rr-P3HT: 1.3 wt% SiNWs. It is important to mention that in all four solutions, the amount of rr-P3HT and the volume of the solvent were kept constant so that the concentration was fixed to 25mg/ml. In essence, among the four solutions, only the amount of SiNWs was different. The rr-P3HT thin film was prepared for reference purposes. Among other things, the performance of a SC depends on the thickness of the absorbing layer and the interaction between the electron D and the A within the photoactive layer. The morphology of the active layer revealed that SiNWs are imbedded with the rr-P3HT film and the thickness measurements showed that the thickness of the film increases with an increase in the concentration of SiNWs.

It was remarkable to observe the absorption spectra of the rr-P3HT film depicting maximum absorption within the visible range of electromagnetic spectrum. Upon addition of SiNWs, the absorption of the thin film increased and the maximum absorption was obtain for rr-P3HT: 0.7 wt% SiNWs. This was ascribed to better structuring of rr-P3HT in the presence of SiNWs and optical absorption SiNWs. With regards to the emission properties, the rr-P3HT thin film depicted emission peaks between 600 and 750 nm which were quenched upon addition of SiNWs. The maximum quenching was obtained for rr-P3HT: 0.7 wt% SiNWs. The quenching signified successful exciton dissociation i.e. the transfer of electrons from the D to the A material. These emission peaks were not quenched completely and in order to increase the degree of quenching another electron accepting material like PCBM should be added in order

to subsidise the electron accepting properties of the hybrid film; alternatively the SiNWs have to be doped to make them to be more n-type so as to accept more electrons.

The TEM analysis of rr-P3HT film were done, which together with the TEM analysis of SiNWs provided a foundation to understand the interaction between rr-P3HT and SiNWs. The rr-P3HT thin film depicted crystalline domains that were ascribed to the periodic fringe patterns corresponding to regular π stacked chains with characteristic lamellar period and featureless zones that were related to amorphous zones of rr-P3HT. The SAED pattern depicted low crystallinity and the two crystalline domains possessing d spacing's of 0.38 and 0.18 nm could be indexed as (010) and (020) reflections, respectively. The interaction between rr-P3HT and SiNWs was examined at a later stage using the solution with the high content of SiNWs i.e. rr-P3HT: 1.3 wt% SiNWs. It was observed that the polymer covers the wall of SiNWs and that there is only physical interaction between the two materials.

The electrical properties of the different hybrid films was probed using Hall Effect measurements which revealed that the conductivity increases with the increase in the concentration of NWs. The increase in conductivity upon the addition of SiNWs in the rr-P3HT matrix was related to an increase of the mobility (μ) of charge carriers in the hybrid films. The maximum conductivity was obtained from rr-P3HT:1.3 wt% SiNWs thin film. Hybrid SCs were characterised by measuring the J-V in dark and under illumination. The baseline efficiency of 0.0007 % was calculated for the least concentration of SiNWs (i.e. rr-P3HT: 0.3 % SiNWs). By increasing concentration of SiNWs into rr-P3HT matrix an efficiency of up to 0.0011 % was realised for rr-P3HT: 1.3 wt% SiNWs. The enhancement in the PCE was related to the fact that more SiNWs were then present in the active layer to extract electrons from rr-P3HT which reduced charge carrier losses. Obtaining an efficiency of 0.0011 % was not sufficient, therefore SCs consisting of PCBM in addition to rr-P3HT and SiNWs were fabricated. For those cells, the maximum PCE of up to 0.68 % was achieved for rr-P3HT:PCBM: 0.8 wt% SiNWs. That solidified the conclusion that, employing inorganic-organic nanomaterial for hybrid SCs fabrication indeed improves the PCE of organic SCs

It is believed that better efficiencies could have been obtained if SCs were fabricated in the glovebox with inert atmosphere. With the lack of this facility in our department, this can be improved by an insertion of an electron transporting layer between the photoactive layer and the Al cathode electrode. The maximum PL emission intensity and the broadening of the peak observed for rr-P3HT: 1.3 wt% SiNWs thin film could not be properly correlated with the J-V curve of the same combination. This is because of the trade-off between the factors influencing the performance of a SC (i.e. V_{oc} , J_{sc} , FF, R_s , and R_{sh}) which makes it difficult to trace the origin of changes observed. Therefore for future work, we suggest the cross sectional characterisation of different hybrid SCs fabricated in this study to be undertaken.

